

GEOCHEMISTRY AND PETROGENESIS OF THE DIABASE DYKES FROM  
THE BOĞAZKALE REGION (ÇORUM, CENTRAL ANATOLIA)

A THESIS SUBMITTED TO  
THE GRADUATE SCHOOL OF NATURAL AND APPLIED SCIENCES  
OF  
MIDDLE EAST TECHNICAL UNIVERSITY

BY

UĞUR BALCI

IN PARTIAL FULFILLMENT OF THE REQUIREMENTS  
FOR  
THE DEGREE OF MASTER OF SCIENCE  
IN  
GEOLOGICAL ENGINEERING

JANUARY 2018



Approval of the thesis:

**GEOCHEMISTRY AND PETROGENESIS OF THE DIABASE DYKES  
FROM THE BOĞAZKALE REGION (ÇORUM, CENTRAL ANATOLIA)**

submitted by **UĞUR BALCI** in partial fulfillment of the requirements for the degree  
of **Master of Science in Geological Engineering Department, Middle East  
Technical University** by,

Prof. Dr. Gülbin DURAL  
Dean, Graduate School of **Natural and Applied Sciences**

Prof. Dr. Erdin BOZKURT  
Head of Department, **Geological Engineering**

Assoc. Prof. Dr. Kaan SAYIT  
Supervisor, **Geological Engineering Dept., METU**

**Examining Committee Members:**

Assoc. Prof. Dr. Biltan KÜRKÇÜOĞLU  
Geological Engineering Dept., Hacettepe Univ.

Assoc. Prof. Dr. Kaan SAYIT  
Geological Engineering Dept., METU

Assist. Prof. Dr. Fatma TOKSOY KÖKSAL  
Geological Engineering Dept., METU

Assist. Prof. Dr. Ali İMER  
Geological Engineering Dept., METU

Assoc. Prof. Dr. H. Evren ÇUBUKÇU  
Geological Engineering Dept., Hacettepe Univ.

**Date:** 15.01.2018

**I hereby declare that all information in this document has been obtained and presented in accordance with academic rules and ethical conduct. I also declare that, as required by these rules and conduct, I have fully cited and referenced all material and results that are not original to this work.**

Name, Last Name: Uğur BALCI

Signature:

## **ABSTRACT**

### **GEOCHEMISTRY AND PETROGENESIS OF THE DIABASE DYKES FROM THE BOĞAZKALE REGION (ÇORUM, CENTRAL ANATOLIA)**

BALCI, Uğur

M.Sc., Department of Geological Engineering

Supervisor: Assoc. Prof. Dr. Kaan SAYIT

January 2018, 119 pages

The Izmir-Ankara-Erzincan (IAE) Suture Belt contains oceanic and continental fragments derived from the northern branch of Neotethys and associated continental entities. In the Boğazkale region (Çorum, Central Anatolia), the pieces of Neotethyan oceanic lithosphere are present in a chaotic manner, and form an ophiolitic *mélange*. Diabase dykes are observed in the *mélange*, which cross-cut various rock types of oceanic lithosphere, such as pillow basalts, gabbros and ultramafics. This study aims to investigate the geochemical and petrogenetic features of the diabase dykes, and their importance in the Neotethyan framework.

The investigated diabbases are mainly made up of plagioclase and a mafic phase, which is clinopyroxene and/or hornblende. According to predominating mafic mineral phase, the diabbases can be subdivided into two types as clinopyroxene- and hornblende-diabase. Sub-ophitic textures are common in all clinopyroxene-diabase samples and poikilitic texture in almost all hornblende-diabase samples. Both types are variably modified by low-grade hydrothermal alteration as reflected by the presence of secondary minerals, such as chlorite, epidote, prehnite and actinolite.

The immobile trace element systematics reveals two chemical types, which seems consistent with the petrographical grouping. Both chemical types display sub-alkaline basalt characteristics. The relationship of MgO with some major and trace elements suggest that fractional crystallization was important in the magmatic evolution of the dykes. One of the major differences between two types is that while Type 2 diabases possess negative Nb anomalies, this feature is not observed in Type 1. In addition, Type 1 diabases are characterized by slight LREE enrichment, whereas Type 2 diabases display flat to slightly LREE-depleted patterns. Type 2 appears to have derived from a depleted asthenospheric mantle source metasomatized by slab-derived fluids/melts. Geochemical signatures of Type 1, on the other hand, require relatively enriched source region and/or small degrees of partial melting.

Trace element systematics of Type 2 is consistent with an origin in an oceanic back-arc basin, whereas Type 1 diabases appear to have been generated in a mid-ocean ridge or an oceanic back-arc basin.  $^{40}\text{Ar}$ - $^{39}\text{Ar}$  radiometric dating on the amphiboles from two Type 2 samples reveals ages of  $176.30 \pm 0.52$  Ma (Toarcian) and  $178.82 \pm 0.80$  Ma (Toarcian), which suggests the presence of an intra-oceanic subduction zone within IAE Ocean during the Early Jurassic.

Keywords: Izmir-Ankara-Erzincan Suture, Ophiolitic Mélange, Neothethys, Petrography, Geochemistry,  $^{40}\text{Ar}$ - $^{39}\text{Ar}$  Geochronology.

## ÖZ

### **BOĞAZKALE CİVARINDAKİ (ÇORUM, İÇ ANADOLU) DİYABAZ DAYKLARININ JEOKİMYASI VE PETROJENEZİ**

BALCI, Uğur

Yüksek Lisans, Jeoloji Mühendisliği Bölümü

Tez Yöneticisi: Doç. Dr. Kaan SAYIT

Ocak 2018, 119 sayfa

İzmir-Ankara-Erzincan (IAE) kenet kuşağı Neotetis'in kuzey kolundan ve bununla ilişkili kıtasal varlıklardan oluşan okyanusal ve kıtasal parçaları içinde barındırır. Bu okyanusal litosfer parçaları, Boğazkale (Çorum, İç Anadolu) bölgesinde ofiyolit karmaşığı adı verilen kaotik bir ortamda bulunur. Bu karmaşığın içinde yastık bazaltlarını, gabroları ve ultramafikleri kesen diyabaz daykları mevcuttur. Bu çalışma bu diyabaz dayklarının jeokimyasını ve petrojenezini ve bunların Neotetis çalışmalarındaki önemini incelemeyi amaçlamaktadır.

İncelenen diyabazlar ana olarak plajioklazdan ve klinopiroksen ve/veya hornblendden oluşan mafik bir fazdan meydana gelmektedir. Kayacı domine eden mafik mineral fazına göre, diyabazlar klinopiroksen- ve hornblend-diyabaz olmak üzere iki tipe ayrılmıştır. Klinopiroksen-diyabazların tamamı yarı-ofitik dokuya sahiptir ve neredeyse hornblend-diyabazlarının tamamı poikilitik dokuya sahiptirler. İkincil mineraller olan klorit, epidot, prehnit ve aktinolitlerin varlığı her iki tipinde değişik seviyelerde düşük dereceli hidrotermal alterasyondan etkilendiğini göstermektedir.

Farklı mobil olmayan iz elementleri sistematğine göre deęerlendirilen tm kaya jeokimyası petrografik olarak ayrılan iki grubu desteklemektedir. Her iki tipte yarı-alkali bazaltik kompozisyona sahiptir. MgO'nın dięer ana ve iz elementleri ile iliřkisi, daykların magmatik evriminde fraksiyonel kristalleřmenin nemli bir rol oynadıęını nermektedir. İki tip arasındaki ana farklardan birisi, Tip 2'nin negatif Nb anomalisi gsteriyorken Tip 1'in bu zellięi gstermemesidir. Bunun yanında, Tip 2 diyabazları dzden hafife kadar deęiřen bir LREE deseni izerken, Tip 1 diyabazları hafif bir řekilde LREE zenginleřmesi gstermektedir. Tip 2 dalma batma zonu sıvılarından/ergiyiklerinden etkilenen bir tkenmiř astenosferik manto kaynaęından tremektedir. Dięer taraftan, Tip 1'in jeokimyasal imzası ise onun greceli olarak daha zenginleřmiř bir kaynaęa ve/veya dřk dereceli kısmi ergimeye ihtiyaı olduęunu iřaret etmektedir.

Tip 2'nin iz element sistematęi onun okyanusal yay-ardı baseninde olduęunu gsteriyorken, Tip 1 diyabazlarının okyanus ortası sırtı veya okyanusal yay-ardı baseninde olduęu grlmektedir. Amfibollerin  $^{40}\text{Ar}$ - $^{39}\text{Ar}$  radyometrik yařları aracılıęı ile iki Tip 2 rneęinin yařlarının  $176.30 \pm 0.52$  Ma (Toarcian) ve  $178.82 \pm 0.80$  Ma (Toarcian) olduęu ortaya konulmaktadır ki bu Erken Jura'da IAE Okyanusu'nun iinde okyanus ii dalma-batma zonunun varlıęını nermektedir.

Anahtar Kelimeler: İzmir-Ankara-Erzincan Keneti, Ofiyolitik Karmařık, Neotetis, Petrografi, Jeokimya,  $^{40}\text{Ar}$ - $^{39}\text{Ar}$  Jeokronolojisi.

To those who believe in science...

## **ACKNOWLEDGEMENTS**

I would like to express my special thanks to my supervisor Assoc. Prof. Dr. Kaan Sayıt for his invaluable guidance, technical support, patience and encouragement during this M.Sc. study. I am extremely grateful for his advice, both on academic and on personal level. His attitude inspired and encouraged me for writing this thesis.

I would like to express my thanks to Prof. Dr. M. Cemal Göncüoğlu for his valuable recommendations, discussions and ideas regarding this study.

I would like to thank Orhan Karaman for the preparation of thin sections.

I would like to express my special thanks to Assist. Prof. Dr. Okay Çimen, Alican Aktağ and Faruk Berber for their mental and scientific supports and discussions. It would be difficult for me to finish fieldworks without them.

I would like to thank my office-mate Serdar Gökem Atasoy and Timur Ersöz for their discussions and supports during this thesis.

I would like to express my special thanks to my family for their endless encouragements throughout this study.

At last but not the least, I would like to express my very special thanks to my love, Ülkü Baturoğlu for his psychological support, trust and patience throughout this thesis.

I would not be able to succeed in this thesis without her endless understanding

## TABLE OF CONTENTS

ABSTRACT .....	v
ÖZ .....	vii
ACKNOWLEDGEMENTS .....	x
TABLE OF CONTENTS .....	xi
LIST OF TABLES .....	xiii
LIST OF FIGURES .....	xiv
CHAPTERS	
1. INTRODUCTION .....	1
1.1. Purpose and Scope.....	1
1.2. Previous Studies .....	3
1.2.1. Neo-Tethys Concept.....	3
1.2.2. Diabase Dykes around the World and Their Datings.....	7
1.2.3. Diabase Dykes from the Alpine Sutures and Their Datings .....	10
1.3. Geographic Location .....	13
1.4. Fieldwork.....	14
1.5. Laboratory Work .....	14
2. GEOLOGICAL FEATURES.....	15
2.1. Regional Geology .....	15
2.2. Geological Observations in the Study Area .....	19
3. PETROGRAPHY.....	29
3.1. Diabase Dykes .....	30

3.1.1.	Clinopyroxene-Diabases .....	30
3.1.2.	Amphibole-Diabases .....	34
3.2.	Host Rocks.....	40
4.	GEOCHEMISTRY .....	47
4.1.	Introduction .....	47
4.2.	Analytical Methods and Assessment of Alteration .....	47
4.3.	Classification .....	50
4.4.	Elemental Variations .....	51
4.4.1.	Major Oxides.....	51
4.4.2.	Trace Elements .....	53
4.5.	Petrogenesis.....	59
4.5.1.	Fractional Crystallization .....	59
4.5.2.	Source Features .....	60
4.5.3.	Partial Melting.....	65
4.6.	Tectonic Discrimination of the Studied Samples .....	67
4.7.	Geochronology of the Diabase Dykes .....	76
5.	DISCUSSION .....	81
6.	CONCLUSION .....	89
	REFERENCES.....	91
	APPENDICES.....	109
A.	GEOCHEMICAL ANALYSIS RESULTS .....	109
B.	<sup>40</sup> Ar/ <sup>39</sup> Ar GEOCHRONOLOGY ANALYSIS RESULTS .....	114
HT-20-A .....		114
HT-16 .....		117

## LIST OF TABLES

### TABLES

Table 1. Geochemical analysis results of Boğazkale diabases. ....	109
Table 2. Incremental heating results of HT-20-A sample.....	114
Table 3. Inverse isochron data of HT-20-A sample.....	115
Table 4. Age summary of HT-20-A sample.....	116
Table 5. Incremental heating results of HT-16 sample.....	117
Table 6. Inverse isochron data of HT-16. ....	118
Table 7. Age summary of HT-16 sample.....	119

## LIST OF FIGURES

### FIGURES

Figure 1. Simplified schematic section of a typical ophiolitic sequence (modified from Brown and Mussett, 1993 and Winter, 2001). .....	2
Figure 2. Distribution of the Alpine terranes showing Izmir-Ankara-Erzincan Suture between Sakarya composite terrane in the north and Tauride-Anatolide platform in the south (modified from Göncüoğlu, 2010).....	4
Figure 3. Tectonic map of Eurasia and North Africa illustrating Alpide Suture between Laurasia and Gondwanaland. Numbers are representing diabase dyke studies along Alpide suture. 1-Betic Zone (Weijermars, 1991), 2-Southern Apennine (Sansone et al., 2011), 3-Alpine (Bernoulli et al., 2003), 4-Pieniny Klippen Belt (Hoeck et al., 2009), 5-Vardar Zone (Bozovic et al., 2013), 6-North-West Dinarides (Pamir et al., 2002), 7-Central Dinarides (Lugovic et al., 1991), 8-Armutlu – Almacık Mountain (Gülmez et al., 2012), 9-Orhaneli ophiolite (Sarıfakıoğlu et al., 2010), 10-Ankara Mélange (Dilek and Thy, 2006), 11-Ankara Mélange (Tankut et al., 1998), 12-Divriği ophiolite (Parlak et al., 2006), 13-Mersin ophiolite (Parlak and Delaloye, 1996), 14-Tauride ophiolites (Dilek et al., 1999), 15-Mersin ophiolite (Çelik, 2008), 16-Pozanti-Karsanti ophiolite (Parlak, 2000), 17-Pozanti-Karsanti (Lytwyn and Casey, 1995), 18-Pozanti-Karsanti ophiolite (Çakır, 2009), 19-Pozanti-Karsanti ophiolite (Çelik, 2007), 20-Pınarbaşı ophiolite (Kayseri) (Vergili and Parlak, 2005), 21-Lycian ophiolites (Çelik and Chiaradia, 2008), 22-Antalya and Lycian ophiolites (Çelik and Delaloye, 2003), 23-Tekirova ophiolite (Antalya) (Bağcı and Parlak, 2009), 24-İspendere Ophiolite (Malatya) (Parlak et al., 2012), 25-East of Van (Çolakoğlu et al., 2012), 26-Sevan/Akera ophiolites (Galoyan et al., 2009), 27-Sevan/Akera ophiolites (Rolland et al., 2010), 28-Zagros ophiolites (Ao et al., 2016) (modified from Şengör et al., 1988). .....	12
Figure 4. Location map of the study area. ....	13

Figure 5. Geological map of Çorum region including the main faults and thrusts (modified from Bortolotti et al., 2013 after 1/500.000 Geological map of Turkey, MTA). .....	17
Figure 6. Geological map of the study area (modified from 1/100.000 Geological maps of Yozgat – İ33 (2007) and Çorum - H33 (2010) quadrangles of Turkey, MTA).....	19
Figure 7. Geological map of the study area with the diabase samples collected from the field (map is modified from 1/100.000 Geological map of Turkey Publication, MTA, 2010). .....	20
Figure 8. Field photographs of a) bracciated pillow basalt and b) bracciated pillow basalt cross-cut by a diabase dyke. ....	21
Figure 9. Field photographs of a) a diabase dyke intruding into basalt. b) closer view of the same dyke showing chilled margin and size difference from edge to core. ....	22
Figure 10. Field photograph of a diabase dyke cross-cutting through a gabbro host rock.....	23
Figure 11. Closer view of the diabase dyke cross-cutting gabbro in Figure 10.....	24
Figure 12. Field photograph of an ultramafic host rock cross-cut by a diabase dyke. ....	25
Figure 13. Field photograph of an ultramafic host rock cross-cut by a diabase dyke having chilled margin.....	25
Figure 14. Another field photograph showing another diabase dyke cross-cutting carbonatized ultramafic rock. ....	26
Figure 15. Field photograph of a diabase dyke intruding into ultramafic host rock..	27
Figure 16. Closer view of the diabase dyke cross-cutting into ultramafic host rock in Figure 15. ....	27
Figure 17. Field photograph showing faulting after intrusion of the diabase dyke. ..	28
Figure 18. Thin section photograph of a clinopyroxene-diabase showing interference color difference of clinopyroxene and plagioclase minerals (Sample HT-14; 4X, XPL, pl: plagioclase, cpx: clinopyroxene). ....	31

Figure 19. Plagioclase phenocrysts showing embayed texture (Sample 15-BOG-6; 4X, XPL, pl: plagioclase).....	31
Figure 20. Plagioclase grains are partly enclosed by larger clinopyroxene, illustrating sub-ophitic texture (Sample 15-BOG-7; 4X, XPL, pl: plagioclase, cpx: clinopyroxene).....	32
Figure 21. a) Clinopyroxene diabase characterized by low-grade alteration products including chlorite epidote and prehnite. Chlorite is seen variably replacing mafic phases, while epidote occurs as a vein-filling mineral b) Same sample showing the interference colors of chlorite, epidote and prehnite minerals (Sample 15-BOG-4B; 10X, a) PPL and b) XPL, ep: epidote, chl: chlorite, pr: prehnite).....	33
Figure 22. Thin section photograph illustrating calcite vein (Sample 15-BOG-4B; 10X, XPL, cc: calcite).....	34
Figure 23. a) Amphibole-diabase including primary hornblendes illustrating brownish colors. b) same view under XPL showing moderate interference color of hornblende (Sample HT-20-A; 10X, a) PPL and b) XPL, hb: hornblende).....	35
Figure 24. Remnant poikilitic texture characterized by clinopyroxene grain (now altered to actinolite) enclosed by a larger plagioclase (Sample HT-19; 10X, a) XPL and b) PPL, pl: plagioclase, cpx: clinopyroxene).....	36
Figure 25. Thin section photograph of a primary hornblende showing simple twinning (Sample HT-20-B; 20X, XPL, hb: hornblende).....	37
Figure 26. a) Thin section photograph illustrating color difference of chlorite, prehnite and actinolite. b) XPL appearance of the same view but displaying interference color difference of the same minerals (Sample 15-BOG-8; 4X, a) PPL and b) XPL, chl: chlorite, pr: prehnite, act: actinolite). ....	38
Figure 27. Thin section showing biotite mineral a) showing brownish color and b) showing mottled extinction (Sample 15-BOG-8; 10X, a) PPL and b) XPL, bio: biotite). ....	39
Figure 28. Thin section photographs of a basalt showing clinopyroxenes and plagioclases with sub-ophitic texture (Sample 15-BOG-5; 10X, XPL, cpx: oclinopyroxene, pl: plagioclase). ....	41

Figure 29. a) Thin section photograph of a basalt showing plagioclase and the color difference of secondary actinolite and chlorite and b) interference color difference of chlorite and actinolite (Sample 15-BOG-5; 10X, a) PPL and b) XPL, act: actinolite, chl: chlorite, pl: plagioclase). .....	41
Figure 30. Thin section photographs of a gabbro showing clinopyroxene and plagioclase minerals and secondary chlorite minerals under PPL and XPL (Sample 15-BOG-2; 4X, a) PPL and b) XPL, ol: olivine, pl: plagioclase, chl: chlorite). .....	43
Figure 31. Thin-section photograph of a gabbro showing vein-filling epidote with a) pistachio green color and high relief and b) upper third-order interference color (Sample 15-BOG-2; 4X, a) PPL and b) XPL, ep: epidote). .....	43
Figure 32. A thin section example of a serpentinite showing a) colorless to pale green colors and b) first-order interference colors (Sample 17-BOG-7; 10X, a) PPL and b) XPL). .....	44
Figure 33. Thin section photograph showing primary clinopyroxene and secondary calcite under a) PPL and b) XPL (Sample 17-BOG-1; 10X, cpx: clinopyroxene, cc: calcite). .....	45
Figure 34. Distribution of selected major and trace elements against Zr. ....	49
Figure 35. Multi-element diagram illustrating distributed appeared in mobile elements such as Sr, K, Ba and Rb. ....	50
Figure 36. Classification diagram of relatively immobile elements (Winchester and Floyd (1977) modified by Pearce (1996)). .....	51
Figure 37. Major oxides (wt.%) variation diagrams of the selected samples. ....	52
Figure 38. Variation diagram of MgO (wt.%) vs. trace elements of the selected samples. ....	54
Figure 39. N-MORB normalized multi-element variation patterns of Type 1 and Type 2 samples (normalization data from Sun and McDonough, 1989). ....	57
Figure 40. Chondrite normalized REE patterns of Type 1 and Type 2 samples (normalization data from Sun and McDonough, 1989). ....	58

Figure 41. Zr/Nb-La/Nb diagram. Greater Antilles data from Jolly et al. (1998); South Sandwich data from Pearce et al. (1995); Aolian Arc data from Calanchi et al. (2002); Andes data from compilation of Winter (2001) after Thorpe et al. (1984); Mariana back-arc data from Pearce et al. (2005); Mid-Atlantic Ridge data from Niu et al. (2001) and OIB, E-MORB and N-MORB data from Sun and McDonough (1989).....	61
Figure 42. Zr/Nb-Zr/Y diagram. All data sources can be seen in Figure 41.....	62
Figure 43. Zr/Y-Nb/Y diagram. All data sources can be seen in Figure 41.....	63
Figure 44. Nb/Yb-Th/Yb diagram. All data sources can be seen in Figure 41.....	64
Figure 45. Zr/Nb-Th/Nb diagram. All data source can be seen in Figure 41.....	65
Figure 46. Geochemical modelling of the diabase rocks having MgO (wt.%) content more than 5.00. E-DMM and DMM compositions of Workmann and Hart (2005) have been adopted for the garnet and spinel peridotite sources, respectively. Garnet peridotite source is assumed to have the mode of 0.600 Ol + 0.210 Opx + 0.120 Cpx + 0.070 Grt, which melts in the proportions 0.010 Ol + 0.040 Opx + 0.500 cpx + 0.450 Grt. Spinel peridotite source has the mode of 0.565 Ol + 0.220 Opx + 0.180 Cpx + 0.035 Spi and melts in the proportions of 0.200 Ol + 0.150 Opx + 0.550 Cpx + 0.100 Spi. Both melting curves have been modelled according to batch melting. Straight lines represent melt-mixing lines between various degrees of Grt-facies melts (2–9%) and 4.5% Spi-facies melt. Melt fractions contributed by these facies were indicated by dots drawn at each 10% interval (Sayit et al, 2016). .....	66
Figure 47. Ti/Y-Zr/Y tectonic discrimination diagram (Pearce and Gale, 1977). .....	67
Figure 48. Ti/1000-V tectonic discrimination diagram (Shervais, 1982). .....	68
Figure 49. Hf/3-Th-Nb/16 tectonic discrimination diagram. A = N-MORB, B = E-MORB, C = OIB (Rift) and D = Arc-basalts (Wood, 1980).....	68
Figure 50. N-MORB normalized multi-element pattern of Type 1 and Type 2 diabases with the comparison of OIB data from Sun and McDonough, (1989).....	69
Figure 51. N-MORB normalized multi-element pattern of Type 1 and Type 2 with the comparison of Greater Antilles data (Sample No: FJ-25; MgO (wt.%) = 6.75 from Jolly et al. (1998)) .....	70

Figure 52. N-MORB normalized multi-element pattern of Type 1 and Type 2 with the comparison of South Sandwich data (Sample No: SSS (10-1); MgO (wt.%) = 7.45 from Pearce et al. (1995)).....	71
Figure 53. N-MORB normalized multi-element pattern of Type 1 and Type 2 with the comparison of Aolian Arc data (MgO (wt.%) = 6.37) from Calanchi et al. (2002)).	72
Figure 54. N-MORB normalized multi-element pattern of Type 1 and Type 2 with the comparison of Andes data (Sample No: CVZ-Cal-LO34; MgO (wt.%) = 7.76) from compilation of Winter (2001) after Thorpe et al. (1984)).....	73
Figure 55. N-MORB normalized multi-element pattern of Type 1 and Type 2 diabases with the comparison of E-MORB data (Sun and McDonough, 1989).....	74
Figure 56. N-MORB normalized multi-element pattern of Type 1 and Type 2 with the comparison of Mariana back-arc data (Sample No: D1010; MgO (wt.%) = 7.57) from Pearce et al. (2005)). .....	75
Figure 57. a) Incremental heating $^{40}\text{Ar}/^{39}\text{Ar}$ age spectra for HT-16 diabase rock showing $176.30 \pm 0.52$ Ma age. The $^{40}\text{Ar}/^{39}\text{Ar}$ age has 95% confidence level limit ( $2\sigma$ ) including 0.29% standard deviation ( $1\sigma$ ) in the J-value. b) Inverse isochron plots for incremental heating $^{40}\text{Ar}/^{39}\text{Ar}$ age spectra for HT-16 diabase rock indicating Ar-loss for the edge of the crystal. Note that reference line (purple line) is shown in conjunction with the calculated isochron (pink line). Green squares indicates steps included in the age calculations. Blue circles indicates steps which are not included in the age calculations. The locations of the total fusion (TF) points are shown by red circle which is not included in the calculations. ....	77
Figure 58. a) Incremental heating $^{40}\text{Ar}/^{39}\text{Ar}$ age spectra for HT-20-A diabase rock showing $178.82 \pm 0.80$ Ma age. The $^{40}\text{Ar}/^{39}\text{Ar}$ age has 95% confidence level limit ( $2\sigma$ ) including 0.44% standard deviation ( $1\sigma$ ) in the J-value. b) Inverse isochron plots for incremental heating $^{40}\text{Ar}/^{39}\text{Ar}$ age spectra for HT-20-A diabase rock indicating again Ar-loss for the edge of the crystal. Note that reference line (purple line) is shown in conjunction with the calculated isochron (pink line). Green squares indicates steps included in the age calculations. Blue circles indicates steps which are not included in the age calculations. The locations of the total fusion (TF) points are shown by red circle which is not included in the calculations. ....	78



## **CHAPTER 1**

### **INTRODUCTION**

#### **1.1. Purpose and Scope**

Ophiolites are thought to be remnants of the oceanic crust and uppermost mantle, which have been tectonically emplaced onto the continental crust (e.g. Coleman, 1971, 1977; Peters et al., 1991). These ancient analogues of oceanic lithosphere may include deep-sea sediments, pillow basalts, sheeted dykes, isotropic and layered gabbros, and ultramafics. (Figure 1). In some places, ophiolitic successions are more or less preserved, as in the case of Oman and Cyprus (e.g. Boudier and Nicolas, 1986; Murton, 1990; Dilek and Eddy, 1992; Robertson, 2002; Dilek and Robinson, 2003). In other instances, however, the coherency of ophiolitic sequences is found to have been destroyed and they instead occur as blocks within a chaotic mixture of rocks, called a “*mélange*” (e.g. Raymond, 1984). The ophiolitic *mélanges* may contain fragments of oceanic lithosphere as well as structures built on it, such as seamounts and oceanic islands.

Oceanic domains do not exist forever; they are eventually consumed by subduction. The destruction of oceanic lithosphere will ultimately lead to collision of two continental plates, which will in turn create a “suture”. Suture zones are important in the sense that they include fragments of oceanic domains and continental masses surrounding them. Ophiolitic *mélanges* are common in suture zones and each piece in an ophiolitic *mélange* may provide a good perspective to understand the geodynamical evolution of the related ancient ocean.

Turkey has a complex tectonic history owing to amalgamation of a number of terranes which are separated by several suture zones (e.g. Göncüoglu et al. 1997). One of these suture zones, known as, Izmir-Ankara-Erzincan (IAE) Suture Zone, contains fragments of northern branch of Neotethys called IAE Ocean and associated continental entities. The pieces that derived from the IAE oceanic domain are mostly preserved in ophiolitic mélanges within this suture zone, and the Boğazkale (Çorum) region is one of such places where ophiolitic lithologies are found in a chaotic manner. In this region, some parts of the mélange contain dykes that are found to cross-cut various ophiolitic lithologies including basalt, gabbro and peridotites. This study focuses on the petrology of isolated mafic dykes (diabases) from an ophiolitic mélange in the Bogazkale region. With the understanding of the petrology of these diabase dykes in detail, this study aims to reveal the mantle source characteristics, magmatic processes responsible for melt generation and modification, and tectonic setting of the dykes. Also combining Ar-Ar radiometric age dating, this study further aims to bring some constraints to enlighten the geodynamic evolution of IAE Ocean.



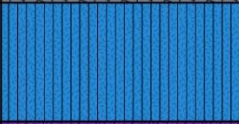
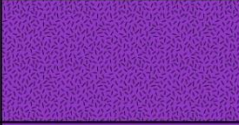



Lithology		Thickness (km)
Deep-Sea Sediment		~0.3
Basaltic Pillow Lavas		0.5
Sheeted Dyke Complex		1.0-1.5
Gabbro		2-5
Layered Gabbro		
Layered Peridotite		up to 7
Unlayered Tectonite Peridotite		

Figure 1. Simplified schematic section of a typical ophiolitic sequence (modified from Brown and Mussett, 1993 and Winter, 2001).

## **1.2. Previous Studies**

Although there are some studies associated with ophiolites in the Boğazkale (Çorum) region, the previous studies on the diabase dykes in this region appear to be very limited. The only study existing in this regard comes from an MTA report by Ateş et al. (2010). In their study, these authors called the ophiolites “Hattuş Ophiolitic Mélange”, which includes the Boğazkale district and Hattuş archaeological site on the H33-d3 quadrangle of 1/25.000 scale topographic map of Turkey. According to them, the Hattuş Ophiolitic Mélange includes serpentized tectonites (e.g. harzburgite), diabase dykes, gabbro, microgabbro, amphibolite, pillow basalt, splite, radiolarite, banded manganese chert and pelagic limestones. Because the ophiolitic lithologies in the region belong to the IAE Ocean, the previous studies on the IAE Ocean must also be reviewed, which will be summarized in the following paragraphs.

### **1.2.1. Neo-Tethys Concept**

The term “Neotethys” refers to one of the ancient ocean realms belonging to the Tethys family (Laubscher and Bernouli, 1977; Şengör, 1979; Stampfli, 2000). The Neotethys takes several names, such as Pyrenees, Bitlis/Zagros Ocean, and Indus/Tsangpo oceans, as geographical locations change. The initial studies regarded Neotethys to have been opened as a back-arc basin related to the south-dipping subduction of Paleotethys (Şengör, 1979; Şengör and Yılmaz, 1981; Görür et al., 1983; Şengör et al., 1984). Şengör (1979) stated that all Alpine-age sutures that lie to the south and west of Dobruja-Crimea-Greater Caucasus represent oceans which opened during the Triassic or later and the Pontide/Anatolide Ocean was regarded to be one of these Neotethyan oceans. The opening of Neotethys separated the Cimmerian Continent (Şengör, 1979) from the Gondwana-Land (Şengör and Yılmaz, 1981). For the details regarding the Cimmerian Continent and Cimmeride orogenic system caused by the closure of Paleotethys, the reader is referred to Şengör et al. (1984).

The Neotethys is subdivided into two main parts as northern branch and southern branch (Şengör and Yılmaz, 1981). The northern branch of Neo-Tethys can be further subdivided into three parts, namely the Izmir-Ankara (also called IAE Ocean), Intra-

Pontide, and the Inner Tauride Oceans, though the existence of the latter two remains enigmatic. According to terrane concept (Göncüoğlu et al., 1997), the Intra-Pontide Ocean was located between the Istanbul-Zonguldak in the north and Sakarya Composite Terrane in the south (Yılmaz, 1990; Göncüoğlu et al., 1997; Yigitbas et al., 1999; Göncüoğlu et al., 2008) (Figure 2). The IAE Ocean is located between Sakarya Composite Terrane in the north (Göncüoğlu et al., 1997) and Tauride-Anatolide Platform in the south (Göncüoğlu, 2010) (Figure 2). The Vardar Ocean between the Apulian platform and Rhodope-Pontide platform is believed to be linked with Izmir-Ankara and/or Intra-pontide Oceans (Şengör and Yılmaz, 1981; Stampfli, 2000; Marroni et al., 2014).

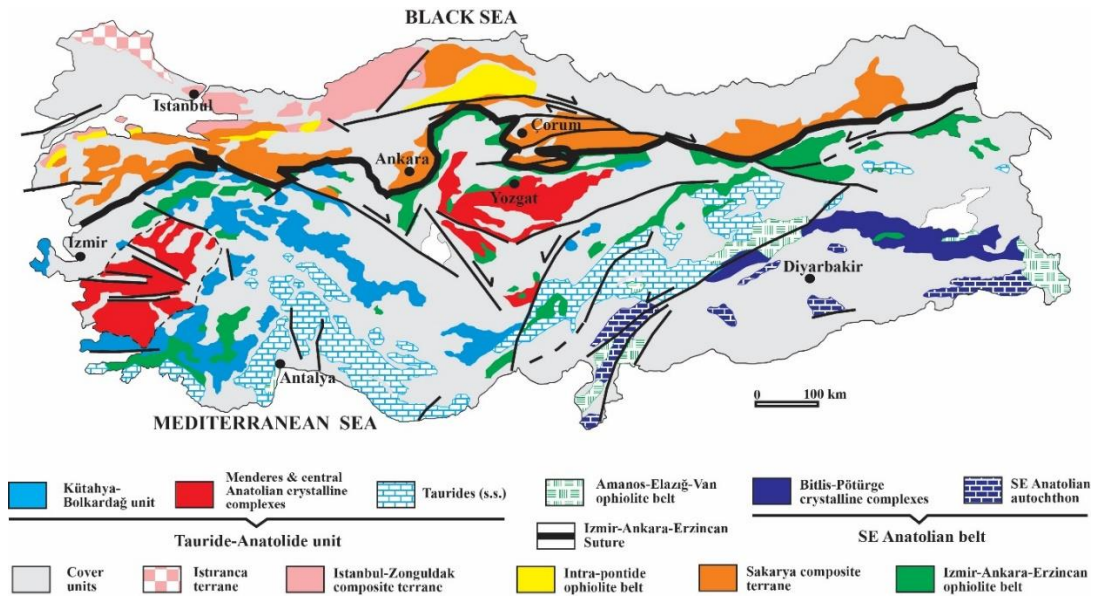


Figure 2. Distribution of the Alpine terranes showing Izmir-Ankara-Erzincan Suture between Sakarya composite terrane in the north and Tauride-Anatolide platform in the south (modified from Göncüoğlu, 2010).

Although there is consensus regarding the existence of IAE Ocean (compared to the Intra-Pontide and Inner-Tauride Oceans), its opening mechanism and time is highly controversial. While some researchers (e.g. Şengör, 1979; Şengör and Yılmaz, 1981;

Görür et al., 1983, 1984; Rojay et al., 2001, 2004) believe that it started to open during the Early Jurassic, the others (e.g. Tekin et al., 2002; Göncüoğlu et al., 2003, 2010; Tekin and Göncüoğlu, 2007, 2009; Tekin et al., 2016; Sayit et al., 2015, 2017) believe that its opening took place earlier than Liassic, and suggest a Triassic time interval instead. Şengör and Yılmaz (1981) claimed Early Jurassic opening by several facts. The Mashad suture in northern Iran indicated that Paleo-tethys ocean closed by the time of the deposition of the Shemshak Formation (Rhaeto-Liassic) (Stöcklin, 1974, 1977; Majidi, 1978) which is equal to the coal-bearing Kelkit Formation of Begougnan (1976) belonging a back-arc setting related to the opening northern branch of Neotethys. Şengör and Yılmaz (1981) also emphasized the works of Altinli (1973) including Early Jurassic basaltic volcanics with tholeiitic character which are overlain by typical shelf deposits of Middle to Late Jurassic age in the south of the Mudurnu area, which indicates Liassic rifting event. They also underlined the works of Fourquin (1975) claiming that opening of this ocean was again Lias (or earlier) as the time of faunal differentiation. Görür et al. (1983) claimed that block faulting and rifting causing the opening of this ocean started at Sinemurian age. Furthermore, Rojay et al. (2001) argued the Liassic opening of this ocean by means of the Liassic discordance throughout the northern Neotethyan belt. They also found Callovian-Hauterivian age interval from thin-shelled the biomicritic carbonates intercalated with pillow basalts from there. The latter researchers used a radiolarian-based age dating from pelagic sediments (e.g. chert) that are primarily related with pillow basalts in order to constrain the age of magmatic event. For example, Tekin et al. (2002) found an early Late Carnian age as the oldest age from a megablock including basaltic pillow basalts radiolarian associated with cherts in the Central Sakarya area. This age was interpreted to be an important implication for the rifting/opening age of the IAE Ocean (Tekin et al., 2002). Göncüoğlu et al. (2003) found within-plate, transitional MORB and MORB-type pillow basalts associated with radiolarian cherts and pelagic limestones from the ophiolites of IAE Ocean within Kütahya-Bolkardağ Belt (KBB). Those radiolarians and conodonts gave middle and early Late Carnian age (Tekin et al., 2002) as the oldest ages from the KBB in the Triassic successions of Tauride-Anatolide Platform and as olistoliths in the Izmir-Ankara mélangé complexes. Later, Tekin and Göncüoğlu (2007) reported a late Ladinian age from a chert block within the Bornova

Flysch Zone. This finding was of particular importance in two aspects. First, the chert block was a part of the Izmir-Ankara Suture Complex, which was later transported from the north to south. Second, this age became the oldest age obtained that far. This depositional age of radiolarian cherts was suggested to indicate the beginning of rifting during the late Middle-early Late Triassic time period (Tekin and Göncüoğlu, 2007, 2009). These Triassic ages were combined with detailed geochemical data in the mélanges of IAE Ocean (Göncüoğlu et al., 2006, 2010; Sayit et al., 2015, 2017). Göncüoğlu et al. (2010) discovered E-MORB-type basalts interlayered with Carnian radiolarian cherts from the Dagküplü Mélange Complex in Central Sakarya, which represents that the formation of true oceanic crust was present at the Carnian time. Sayit et al. (2015) found Middle Carnian arc-type basalts indicating from the Lycian Nappes, Southwestern Anatolia. The finding of Upper Anisian basalt blocks with back-arc basin signatures from the Mersin Mélange by Sayit et al. (2017) indicates not only a pre-Liassic opening age for the Northern Neotethys, but also that it may even have been opened before the Middle Triassic.

When the ages (paleontological or radiometric) and whole-rock geochemical data published thus far are considered, there is a good deal of evidence indicating the predominance of subduction-related magmatism. While some researchers (e.g. Şengör and Yılmaz, 1981) suggested that the contraction of northern branch of Neo-Tethys began at the Early Late Cretaceous time, other researchers with new findings (e.g. Sayit et al., 2016, 2017) recommend that subduction started before Early Cretaceous. According to latter, subduction was already operating in the Middle Triassic as evidenced by the presence of intra-oceanic back-arc basin lavas of Anisian age from the Mersin Mélange. Also, Topuz et al. (2013) found an Early Jurassic aged structurally intact, large ophiolite body from NE Turkey, the Refahiye ophiolite. Dilek and Thy (2006) found  $179 \pm 15$  Ma (Early Jurassic) U-Pb age from plagiogranites coeval with diabase dykes formed in a back-arc basin setting in Ankara Mélange. Görür et al. (1984) and Şengör and Yılmaz (1981) proposed that subduction started during early Late Cretaceous. Also, Harris et al. (1994) found an Ar-Ar isotopic age of  $101 \pm 4$  Ma from the garnet-amphibolite metamorphic rocks in the Tavşanlı Zone, which shows a Cenomanian subduction. Despite some researchers (e.g. Şengör & Yılmaz, 1981) believed that the closure of IAE Ocean was occurred during the latest

Paleocene to early Eocene period, others (e.g. Göncüoğlu et al., 2000) claim that closure was completed by the end of the Cretaceous. The closure of Neo-tethys resulted in the collision between Tauride-Anatolide Platform and the Pontides, which, in turn, led to the formation of Alpine orogenic belts (Şengör and Yılmaz, 1981). The polarity of subduction of IAE Ocean was suggested to be towards north by Şengör and Yılmaz (1981). Görür et al. (1984) also defended the north-dipping subduction of the northern branch of Neo-tethys which began under both the Rhodope-Pontide Fragment and the Sakarya Continent during Late Cretaceous. The collision of the Sakarya Continent with Rhodope-Pontide began at Maastrichtian time (Görür et al., 1984). Şengör et al. (1988) accepted that the dipping of the subduction was mostly in not just the north but also east direction. Yalınız et al. (2000) and Göncüoğlu et al. (2006a, b) also supported intra-oceanic subduction of IAE Ocean. They indicated that the middle Cretaceous SSZ type ophiolites (Yalınız et al., 2000, Göncüoğlu et al., 2006a, b) and radiometric ages of Albian-Campanian (Önen, 2003; Önen and Hall, 1993) proved that IAE Ocean closed along a N-directed intra-oceanic subduction zone.

Intra-plate volcanism was also present in IAE Ocean according to several findings. Rojay et al. (2001) found OIB type basalts formed during Callovian-Hauterivian interval in Dereköy (Haymana region). Göncüoğlu et al. (2006) found a geochemical data of basalts with a range containing OIB data in the Dağkumlu Mélange in the Central Sakarya Valley. The age of the radiolarians from a tectonic block consisting of chert-mudstone alternation which are related to OIB-type basalts is between early Berriasian and early Hauterivian. Moreover, Göncüoğlu et al. (2010) expanded the duration of the intra-plate seamounts producing OIB-type basalts from late Bathonian to early Aptian.

### **1.2.2. Diabase Dykes around the World and Their Datings**

Diabase (also called micro-gabbro or dolerite) is a mafic igneous rock. It is similar to gabbro and basalt in terms of chemical composition, but may show some textural difference, since diabase is a hypabyssal (subvolcanic) rock. Diabase may occur as dykes, and such occurrences have been studied in various regions by several researchers around the world for a long time. Studying diabase dykes can provide

important clues to the geodynamic environment when combined with geochemistry and geochronology. In some studies, diabase dykes appear as the indicators of pre-rifting stages or rifting stages of continents (e.g. Pandey et al., 1996; Wang et al., 2007; Peng et al., 2012). Some of these studies show that the rifting process is related to subduction-related activities, thus giving way to back-arc basins (e.g. Dupuy et al., 1988; Wang et al., 2007). On the other hand, some others (e.g. Bright et al., 2014) points out that diabase dykes derived from an ocean island basalts (OIB)- type plume source in a large igneous province, which is resulted in the rupturing of Laurentia into two parts. Moreover, diabase dykes can also be observed within the ophiolite sequences as isolated or sheeted dykes. (e.g. Boudier and Nicolas, 1986; Murton, 1990; Dilek and Eddy, 1992; Robertson, 2002; Dilek and Robinson, 2003; Çolakoğlu et al., 2012; Parlak et al., 2012).

The age dating of diabase dykes can be of significant importance, especially when combined with geochemistry. Geochronology of diabase dykes can be determined by several methods, including absolute or relative age dating methods. Relative age dating includes one of the principles of geology called the cross-cutting relationship (Steno, 1669; Hutton, 1795). If the age of the host rock that is cross-cut by the dyke is known, then the dyke must be younger than that age or if absolute age of the dyke is known, then age of cross-cut host rock must be older than that of the dyke. In order to determine the absolute age of diabase dykes, radiometric age dating methods such as U-Pb,  $^{40}\text{Ar}$ - $^{39}\text{Ar}$ ,  $^{87}\text{Rb}$ - $^{87}\text{Sr}$ , or  $^{147}\text{Sm}$ - $^{143}\text{Nd}$  isotopic systems can be used. However, these methods must be used and interpreted very carefully, because some of these systems can be easily affected by secondary processes, such as hydrothermal alteration (Kelley, 2002; Söderlund et al., 2005). When a system is disturbed by secondary processes by means of adding or removing some elements by fluids and increasing temperature (if the temperature rises above closure temperature of the system) and/or pressure, the system is no longer a closed system. Hence, the isotopes used in age determination will not give crystallization ages in these cases. However, closure temperature of some radiometric age systems (e.g. U-Pb) is so high (Titanite = 600-650 °C, Rutile = 400-450 °C, Apatite = 450-500 °C, Zircon, monazite and baddeleyite > 1000 °C; Flowers et al., 2005) that they are not affected from low-grade metamorphism. U-Pb system is regarded to be the most reliable dating method

amongst others (Schoene et al., 2014).  $^{40}\text{Ar}$ - $^{39}\text{Ar}$  step-heating method is also reliable, if the sample includes primary minerals such as hornblende, plagioclase, biotite, muscovite. For example, closure temperature of hornblende which can be used in  $^{40}\text{Ar}$ - $^{39}\text{Ar}$  age dating system is between 450 °C and 550 °C (Harrison, 1982), so it is also reliable in rocks that have been metamorphosed under low-grade conditions. Both  $^{147}\text{Sm}$ - $^{143}\text{Nd}$  whole-rock and single mineral isochron age dating methods can also be used for these dykes to get formation age (e.g. Fletcher et al., 1987; Söderlund et al., 2005).  $^{87}\text{Rb}$ - $^{87}\text{Sr}$  method is not suitable for altered rocks to obtain crystallization age due to lower closure temperature of the system (e.g. Söderlund et al., 2005). Thus, these systems must be used for the samples which are relatively fresh (i.e. without or minor alteration) in order to get formation age of the dykes.

Zircon and baddeleyite in mafic rocks have been recently used in U-Pb age dating systems (e.g. Söderlund et al., 2005; Olsson et al., 2010; Bright et al., 2014). Recently, because of the high stability of baddeleyite having crystallization temperature of 626.85 °C-1226.85 °C, it has been very attractive for U-Pb age dating (Lumpkin, 1999). Mineral separation of baddeleyite by LA-ICP-MS (Laser Ablation - Inductively Coupled – Mass Spectrometry) and SIMS (Secondary Ion Mass Spectrometry) in-situ methods for larger baddeleyite crystals have been used by several researchers (e.g. Söderlund and Johansson, 2002; Söderlund et al., 2005; Peng et al., 2012; Wu et al., 2013). If the mineral grains are so small that minerals cannot be separated by mineral separation techniques, SIMS in-situ method can be used for absolute age dating of diabase dykes (e.g. Schmitt et al., 2010; Catlos et al., 2013; Wu et al., 2015).

$^{40}\text{Ar}$ - $^{39}\text{Ar}$  age dating method has also recently been used by several researchers in order to date mafic rocks (e.g. Koppers et al., 2011; Duncan and Al-Amri, 2013; Tchouankoue et al., 2014).  $^{40}\text{Ar}$ - $^{39}\text{Ar}$  age dating system is more productive in whole-rock or single-crystal incremental heating (McDougall and Harrison, 1999). If the sample was affected by alteration, then Ar gas into the system was probably escaped from the system for the minerals having lower closure temperatures. Hence, whole-rock analyses would give a mixture age of crystallization age and alteration age of the rock. On the other hand, single-crystal incremental heating of primary hornblende and plagioclase (regarding with mafic rocks) will give just crystallization age spectrum or

both crystallization and alteration age spectrum. Also, age spectrum for a rock having rapid cooling will be undisturbed which means giving minimum number of ages while age spectrum for a rock having complex cooling histories will be very disturbed which means giving several ages for it (Kelley, 2002).

### **1.2.3. Diabase Dykes from the Alpine Sutures and Their Datings**

The greek suffix “-ide” means ancestor so Alpine Suture is the ophiolitic belt made up of ancestor ophiolitic rocks formed by the closure of Neotethys Ocean (Şengör, 1979; Şengör and Yılmaz, 1981). Alpine sutures can be traced from Pyrenean (France) to Timor (North of Australia) (Şengör et al., 1988). Ophiolites which are the remnants of Neotethys Ocean have been found and studied along this suture for a very long time. Isolated diabase dykes have also been studied in this suture by several workers (Figure 3). In most studies, petrography, geochemistry and geochronology of these dykes have not been covered together in detail. Instead, petrography of those rocks just have been worked in those studies. Figure 3 illustrates these studies on the tectonic map of Eurasia, North Africa and Tethysides including Neo-tethys and several continental portions separating it or containing within it (modified from Şengör et al. 1988). Some studies (e.g. Weijermars, 1991 (Betic Zone); Bernoulli et al., 2003 (Alpine)) point out that the diabase dykes formed in the geological environment of thinning of continental crust and rifting causing opening of Neo-tethys Ocean. On the other hand, others (e.g. Bozovic et al., 2013 (Vardar Zone), Tankut et al., 1998; Dilek and Thy, 2006 (Ankara Mélange), Parlak and Delaloye, 1996 (Mersin ophiolite), Parlak, 2000; Çelik, 2007; Çakır, 2009 (Pozanti-Karsanti ophiolite), Vergili and Parlak, 2005 (Pınarbaşı ophiolite), Çelik and Delaloye, 2003; Çelik and Chiaradia, 2008 (Lycian ophiolite), Bağcı and Parlak, 2009 (Tekirova ophiolite), Parlak et al., 2012 (İspendere ophiolite), Çolakoğlu et al., 2012 (East of Van), Galoyan et al., 2009; Rolland et al., 2010 (Zagros ophiolite)) indicate that these diabase dykes were formed in an intra-oceanic arc-back arc or fore-arc environment of Neo-Tethys. Specifically, the studies (e.g. Bozovic et al., 2013) in the Vardar Zone, the western extension of northern branch of Neo-tethys including Intra-Pontide Ocean and Izmir-Ankara-Erzincan Ocean in Turkey (e.g. Parlak et al., 2006) and the studies (e.g. Lugovic et al., 1991) in the Dinaric Ophiolite

Belt, the western extension of southern branch of Neo-tethys in Turkey (e.g. Çolakoğlu et al., 2012) indicate back-arc basin originated diabase dykes (Figure 3). The studies of Sevan/Akera ophiolites (e.g. Galoyan et al., 2009; Rolland et al., 2010) which is the eastern extension of Izmir-Ankara-Erzincan ophiolites also have shown intra-oceanic back-arc origin of isolated diabase dykes. Moreover, the studies in northern branch of Neo-tethys (e.g. Lytwyn and Casey, 1995; Dilek et al., 1999; Sarifakioğlu et al., 2010) show a fore-arc origin of isolated diabase dykes.

Geochronology of diabase dykes within the Alpine suture have been studied and several methods (e.g.  $^{40}\text{Ar}$ - $^{39}\text{Ar}$ , K-Ar) have been tested by many researchers. Dilek and Thy (2006) found a zircon U-Pb age of  $179 \pm 15$  Ma from plagiogranites which has mutual cross-cutting relationship with the diabase dykes in Ankara Mélange. Parlak and Delaloye (1996) found  $^{40}\text{Ar}$ - $^{39}\text{Ar}$  whole-rock ages between  $89.6 \pm 0.7$  Ma and  $63.8 \pm 0.9$  Ma from diabase dykes which has island arc geochemistry from Mersin ophiolites. Also, Çelik (2008) had two K-Ar ages,  $88.8 \pm 2$  Ma and  $84.4 \pm 3$  Ma, from diabase dykes having island arc geochemistry in Mersin ophiolites. Dilek et al. (1999) have  $^{40}\text{Ar}$ - $^{39}\text{Ar}$  (amphibole) ages as 90-91 Ma from diabases having fore-arc geochemistry in Tauride Belt. Çakır (2009) have a good age reviews of diabase dykes including K-Ar (Plagioclase) age as  $73 \pm 2$  Ma (Lycian ophiolite) (Thuizat et al., 1979), K-Ar and Ar-Ar (Amphibole) ages as  $69.7 \pm 9.8$  and  $79 \pm 9$  Ma (Kütahya) (Önen, 2003), K-Ar (Amphibole) ages as  $65.2 \pm 10.3$  and  $81.8 \pm 5.2$  Ma (Kütahya) (Önen, 2003) and K-Ar (Plagioclase) age as  $71 \pm 1$  Ma (Pozanti-Karsanti) (Çakır, 1978; Thuizat et al., 1981). Çelik and Chiaradia (2008) displays K-Ar diabase dyke with island arc geochemistry ages ranging from 63.6 Ma to 81.4 Ma from Lycian ophiolites. Finally, Çolakoğlu et al. (2012) gave two Ar-Ar ages,  $92 \pm 0.9$  Ma from Mehmetalan Ophiolite and  $105.4 \pm 1.1$  Ma from Mollatopuz Ophiolite, from diabase dykes having intra-oceanic arc-basin geochemistry in East of Van. Except from Turkey, only Pamic et al. (2002) reviewed age dating from diabase dykes along Vardar Zone (VZ). K-Ar (whole rock) age as  $160 \pm 10$  Ma by Majer and Lugovic (1985) in Banovia from VZ, another K-Ar (Hornblende) ages ranging from  $189 \pm 6.7$  Ma to  $185 \pm 6$  Ma by Pamic (1997) in Mt. Kalnik from VZ, another K-Ar (Hornblende) age as  $109.6 \pm 6.6$  Ma by Pamic (1997) in South Pannonian Basin from VZ and K-Ar (whole rock) age as  $62.2$

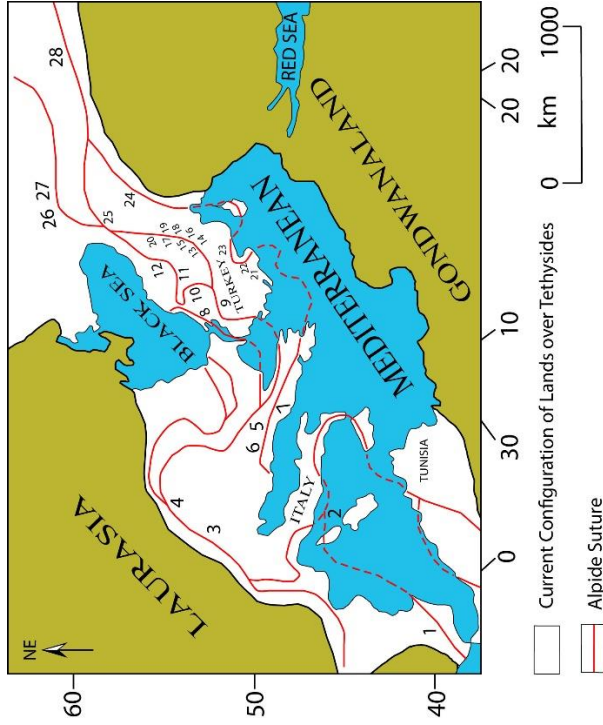


Figure 3. Tectonic map of Eurasia and North Africa illustrating Alpine Suture between Laurasia and Gondwanaland. Numbers are representing diabase dyke studies along Alpide suture. 1-Betic Zone (Weijermars, 1991), 2-Southern Apennine (Sansone et al., 2011), 3-Alpine (Bernoulli et al., 2003), 4-Pieniny Klippen Belt (Hoeck et al., 2009), 5-Vardar Zone (Bozovic et al., 2013), 6-North-West Dinarides (Pamic et al., 2002), 7-Central Dinarides (Lugovic et al., 1991), 8-Armutlu – Almacık Mountain (Gülmez et al., 2012), 9-Orhaneli ophiolite (Sarifakioğlu et al., 2010), 10-Ankara Mélange (Dilek and Thy, 2006), 11-Ankara Mélange (Tankut et al., 1998), 12-Divriği ophiolite (Parlak et al., 2006), 13-Mersin ophiolite (Parlak and Delaloye, 1996), 14-Tauride ophiolites (Dilek et al., 1999), 15-Mersin ophiolite (Çelik, 2008), 16-Pozanti-Karsanti ophiolite (Parlak, 2000), 17-Pozanti-Karsanti (Lytwyn and Casey, 1995), 18-Pozanti-Karsanti ophiolite (Çakır, 2009), 19-Pozanti-Karsanti ophiolite (Çelik, 2007), 20-Pınarbaşı ophiolite (Kayseri) (Vergili and Parlak, 2005), 21-Lycian ophiolites (Çelik and Chiaradia, 2008), 22-Antalya and Lycian ophiolites (Çelik and Delaloye, 2003), 23-Tekirova ophiolite (Antalya) (Bağcı and Parlak, 2009), 24-İspendere Ophiolite (Malatya) (Parlak et al., 2012), 25-East of Van (Çolakoglu et al., 2012), 26-Sevan/Akera ophiolites (Galoyan et al., 2009), 27-Sevan/Akera ophiolites (Rolland et al., 2010), 28-Zagros ophiolites (Ao et al., 2016) (modified from Şengör et al., 1988).

$\pm 2.5$  Ma by Pamic (1997) in South Pannonian Basin from VZ are reviewed along VZ (Pamic et al., 2002).

### 1.3. Geographic Location

The study area is located near Boğazkale district which is almost 65 km south-east of Çorum City Center and almost 30 km north-west of Yozgat City Center (Figure 4). It covers an area of approximately 100 km<sup>2</sup> in the H33-d3 and h33-d4 quadrangles of 1/25.000 scale topographic maps of Turkey.

The study area covers several main villages, including Yazır, Karakeçili, Derbent, Yüksekayla and Küçükhrka.

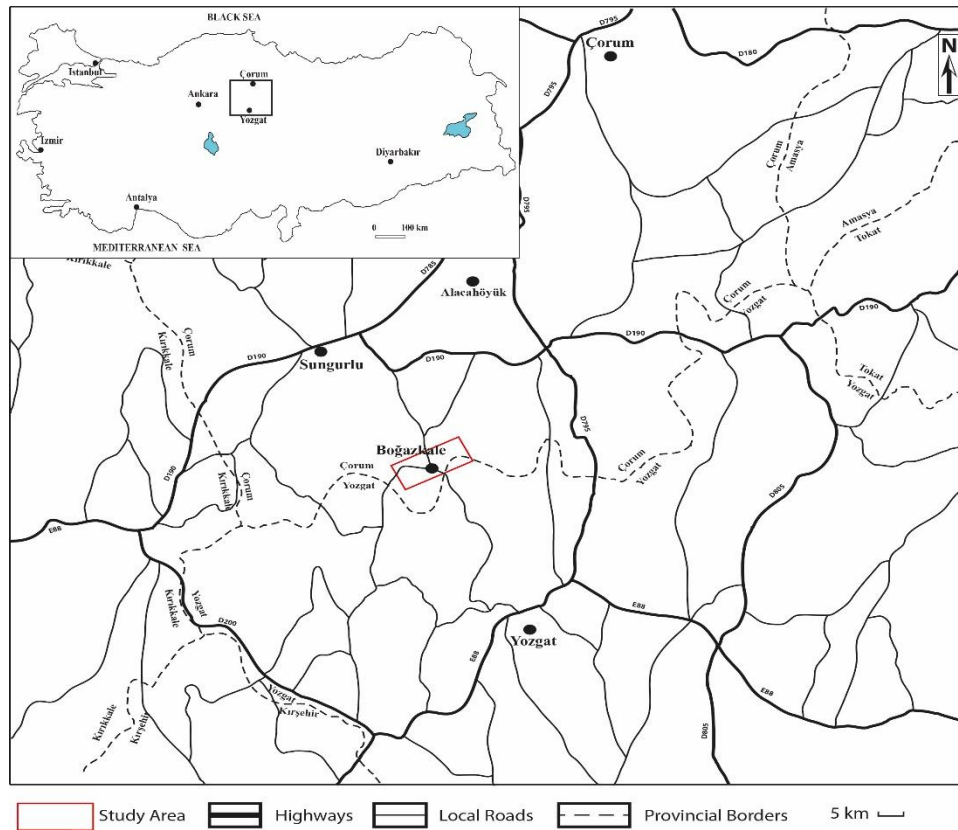


Figure 4. Location map of the study area.

#### **1.4. Fieldwork**

The fieldwork was performed in the summer of 2015, 2016 and 2017 in order to investigate the diabase dykes and their cutting relationship with the host rocks. During the fieldworks, 26 samples from diabase dykes and 14 samples from the host rocks including pillow basalts, gabbros and serpentinized ultramafics were collected.

#### **1.5. Laboratory Work**

The 40 samples collected from the fieldwork was processed in the thin-section preparation laboratory at the Department of Geological Engineering, METU in order to make petrographical investigations. Prepared thin sections were investigated and photographed under the Olympus polarizing microscope with the attachment of Olympus camera. After the petrographical works were finished, 14 samples were selected and prepared for geochemical analysis. All samples were cut into slabs and polished by the carborundum powder in order to weaken the effect of the diamond saw. Then, the samples were sent to Activation Laboratories Ltd. (Ancaster, Ontario, Canada) for whole-rock geochemistry. Major oxides were analysed by means of fusion inductively-coupled plasma (FUS-ICP) while trace elements were analysed by using either FUS-ICP or fusion mass spectrometry (FUS-MS). Samples were diluted and analyzed by Perkin Elmer Sciex ELAN, 9000 ICP/MS. Three blanks and five controls were analyzed per group of samples. Instrument was recalibrated every 40 samples. Finally, two samples (HT-16 and HT-20-A) were selected and sent to Oregon State University Geochronology Laboratories for  $^{40}\text{Ar}/^{39}\text{Ar}$  age dating processes. Primary single hornblende crystals into these samples were separated and analyzed by the laboratory with incremental heating method and by means of Thermo Scientific Model ARGUS-VI-D instrument.

## **CHAPTER 2**

### **GEOLOGICAL FEATURES**

#### **2.1. Regional Geology**

The Anatolia is a tectonically complex region, which can be attributed to a number of orogenic events related to the closure of ancient oceanic domains, such as the Pan-African/Cadomian orogeny, Variscan orogeny, Cimmeride orogeny, and Alpide orogeny with the closure of Neotethys Ocean (Şengör, 1979). These orogenic events controlled the distribution and amalgamation of the terranes, which was last shaped by the Alpide orogeny (Göncüoğlu et al. 1997). In this context, the Anatolia consists of several terranes, including the Istranca Terrane Istanbul-Zonguldak Composite Terrane (IZCT), Sakarya Composite Terrane (SCT), Tauride-Anatolide Terrane and SE Anatolian Autochthon (Göncüoğlu, 2010) (Figure 2). These terranes are separated by three Neotethyan suture belts, namely Intra-Pontide suture, Izmir-Ankara Erzincan (IAE) suture and Southeast Anatolian Suture (Göncüoğlu, 2010) (Figure 2 and 3).

The orogenic events mentioned above are large-scale processes, whose traces can be found beyond the Anatolian region. For example, The Cimmeride orogeny can be traced from the Eastern Carpathians to the Pacific shores of Asia (Şengör et al., 1984). The Mediterranean Cimmerides form the westernmost segment that can be traced from the Eastern Carpathians and North Dobrudja to the eastern end of the Greater Caucasus (Şengör et al., 1984). Moreover, its longitudinal sections can be subdivided into three parts; the Balkan/Carpathian Cimmerides, Anatolian Cimmerides containing the North Dobrudja and the Causian Cimmerides (Şengör et al, 1984). The Alpide

sutures can also be traced from Pyrenees to Indus with different opening ages of the Neotethys ocean. These sutures are Pyrenees (Boillot and Capdevila, 1977), Alps/Apennines (Trümpy, 1975), Carpanthians/Vardar Ocean (Dewey et al., 1973), Pontide/Anatolide Ocean (Delaune-Mayere et al., 1977; Marcoux, 1978), Bitlis/Zagros Ocean (Şengör et al., 1978), North Makran/Afghanistan and Indus/Tsangpo Oceans (Boulin and Bouyx, 1977) (Şengör, 1979).

The IAE Suture Zone is located between the Sakarya Composite Terrane in the north and Tauride-Anatolide Terrane in the south (Göncüoğlu et al., 1997) (Figure 2). The Sakarya Composite terrane was considered by Göncüoğlu et al. (1997) as a composite terrane, since this continental entity includes several pre-Alpine terranes and associated oceanic assemblages in its basement that was amalgamated at different geological times (Göncüoğlu, 2010). This pre-Jurassic basement was covered by Mesozoic flysch-type deposits (Göncüoğlu, 2010). The Tauride-Anatolide Terrane consists of three structural units which are from north to south, the Kütahya-Bolkardağ Belt, the Anatolides including metamorphic units and the Taurides which is made up of non-metamorphic nappes (Göncüoğlu, 2010) (Figure 2).

Four main geological units outcrop in the Çorum region (Figure 5) (based on 1/500.000 Geological map of Turkey, MTA modified by Bortolotti et al., 2013). They are Sakarya Composite Terrane (SCT), Central Anatolian Crystalline Complex (CACC), IAE ophiolitic mélange and cover units (Figure 5). SCT contains several pre-alpine terranes where each of them presents a tectonic assemblage showing different geological histories in its basement (Göncüoğlu et al., 1997; Göncüoğlu, 2010). These tectonostratigraphic units are made up of pieces of Variscan and Cimmerian continental and oceanic assemblages (Göncüoğlu, 2010).

CACC is considered as a part of Anatolides and the eastern extension of the Menderes Massif (Göncüoğlu, 2010). The lowermost unit of CACC contains metamorphic rocks including gneisses, micaschists, amphibolites, marbles and migmatites (Göncüoğlu, 2010). It has a Precambrian basement of Gondwanaland origin, which has been dated by U-Pb on zircon and sphene (Göncüoğlu, 1982; Köksal et al., 2004, 2007, 2008). There is an unconformity after this Precambrian basement followed by a thick quartzitic band indicative of a post-Pan-African transgression in Mesozoic. This thick

quartzite band is followed by metamorphic rocks, recrystallized limestone, Central Anatolian granitoids, pelagic sedimentary rocks and ophiolitic rocks with ages between Triassic to Cretaceous. All of these units are intruded by post metamorphic collision-type granitoides (Göncüoğlu and Türel, 1994; Akıman et al., 1993; Boztuğ, 1998, 2000). Lastly, these units are covered by tertiary olistostromal clastics after an unconformity (Göncüoğlu et al., 1992; Göncüoğlu, 2010).

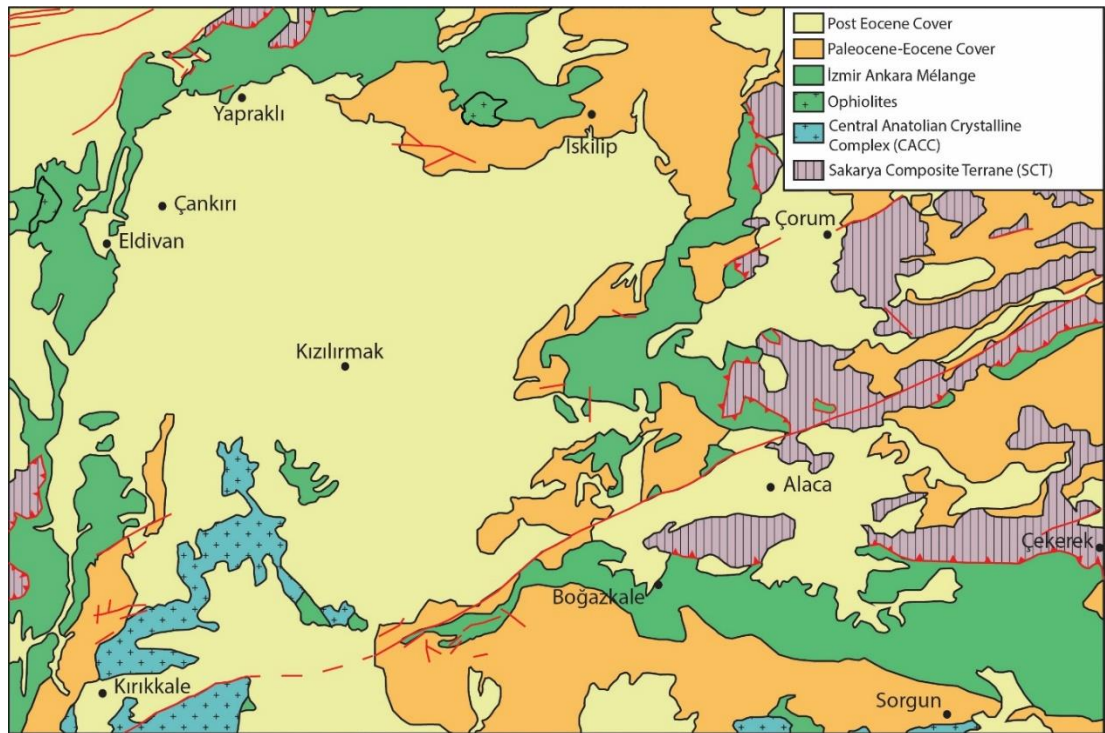


Figure 5. Geological map of Çorum region including the main faults and thrusts (modified from Bortolotti et al., 2013 after 1/500.000 Geological map of Turkey, MTA).

The IAE ophiolitic mélangé contains blocks of almost complete ophiolitic sequences and tectonic mélanges of this accretionary complex (Göncüoğlu et al., 1997; Okay and Tüysüz, 1999; Robertson, 2002). These ophiolitic blocks includes mainly peridotites, gabbros, sheeted dykes, basalts and pelagic sediments (Önen, 2003; Bortolotti et al., 2013). Geochemical studies of these ophiolitic blocks point out SSZ signatures made

up of MORB and OIB affinities (Robertson, 2000; Floyd et al., 2000; Göncüoğlu et al., 2010; Parlak et al., 2012; Bortolotti et al., 2013). They are associated with the late Norian radiolarian cherts as the oldest age from Ankara mélange (Bortolotti et al., 2013).

All of SCT, CACC and IAE ophiolitic mélange units are covered by Paleocene-Eocene and post-Eocene cover units (Bortolotti et al., 2013). In detail, larger scaled geological map of the study area shows that the oldest rocks are Silurian-Triassic limestones and Middle Triassic-Upper Triassic volcanic and sedimentary rocks which are owned by SCT (Figure 6). Age of the ophiolitic rocks including diabase dykes, pillow basalts, gabbros, serpentinized ultramafics and deep sea sedimentary rocks (limestone, chert) are Triassic-Cretaceous. Tectonically, SCT rocks had been thrust onto IAE ophiolitic rocks and there are some klippe of SCT blocks into ophiolite itself. Ophiolitic rocks had been thrust onto Upper Cretaceous flysch deposits which have also been thrust onto Eocene sedimentary and volcanic rocks, basaltic volcanics and also Eocene basaltic pyroclastics. Upper miocene-pliocene terrestrial sandstone-mudstone-limestones are the youngest units in the region so they cover all of the oldest rocks in the region (Figure 6).

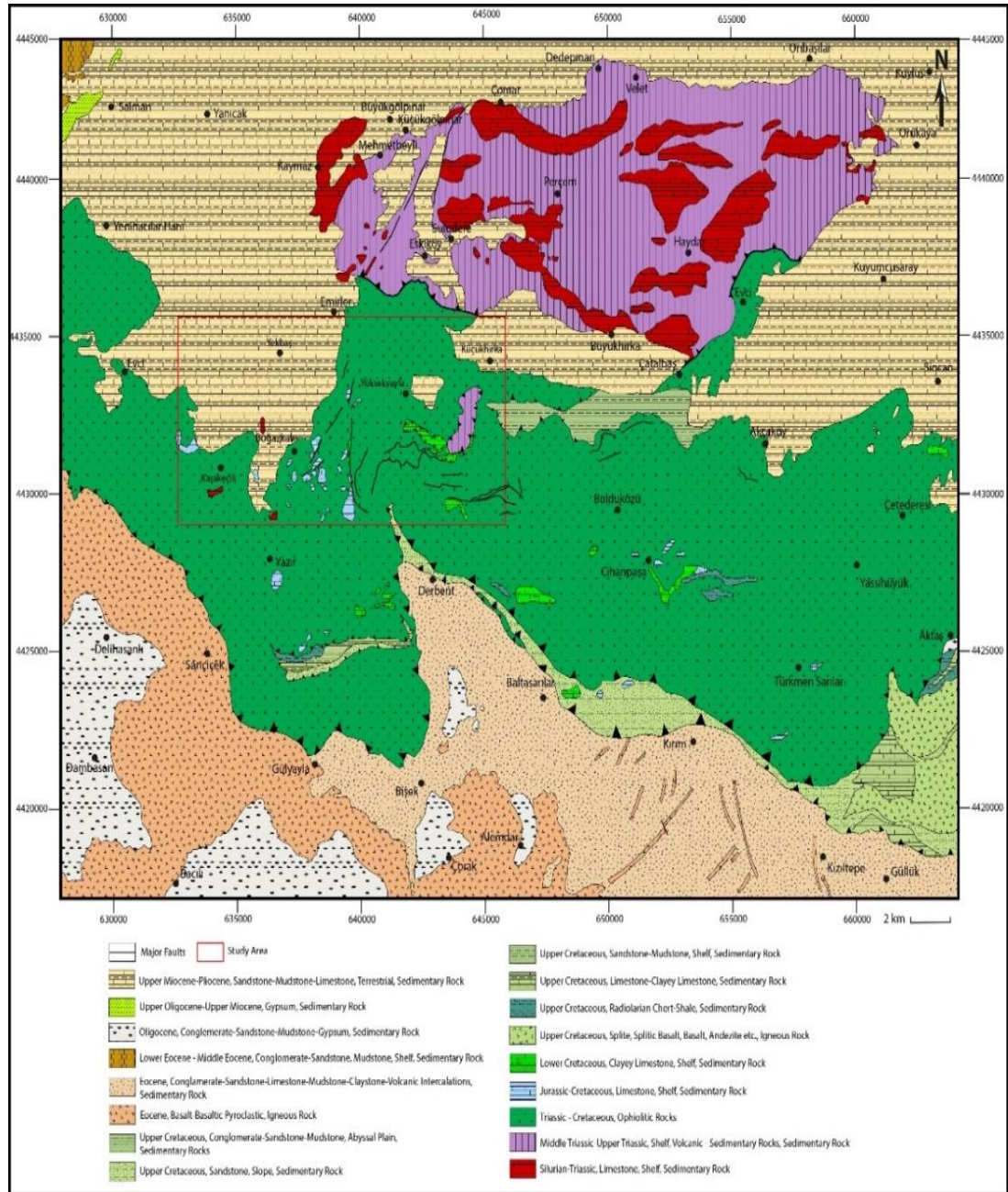


Figure 6. Geological map of the study area (modified from 1/100.000 Geological maps of Yozgat – İ33 (2007) and Çorum - H33 (2010) quadrangles of Turkey, MTA).

## 2.2. Geological Observations in the Study Area

Study area contains the ophiolitic mélangé units which are the remnants of IAE Ocean. The mélangé consists of serpentinized ultramafics, gabbros, pillow basalts, diabase dykes, and deep-sea sediments which are limestones and radiolarian cherts for

this area. Specially, ophiolitic mélange contains Triassic-Cretaceous ophiolitic rocks, Jurassic-Cretaceous shelf limestone, Lower Cretaceous clayey shelf limestone, Upper Cretaceous shelf sandstone-mudstone, and Cenomanian-Campanian slope sandstone. This ophiolitic mélange had been called as “Artova Ophiolitic Mélange” by Özcan et al. (1980) and as “Hattuşaş Ophiolitic Mélange” by Ateş et al. (2010) (Figure 7). It must be noted that the diabase dykes, which are the main focus of this study, only cover a limited portion of the study area (Figure 7). Geological observations in the study area points out that all diabase dykes are observed to intrude into ophiolitic lithologies, including pillow basalts, gabbros and serpentinized ultramafics.

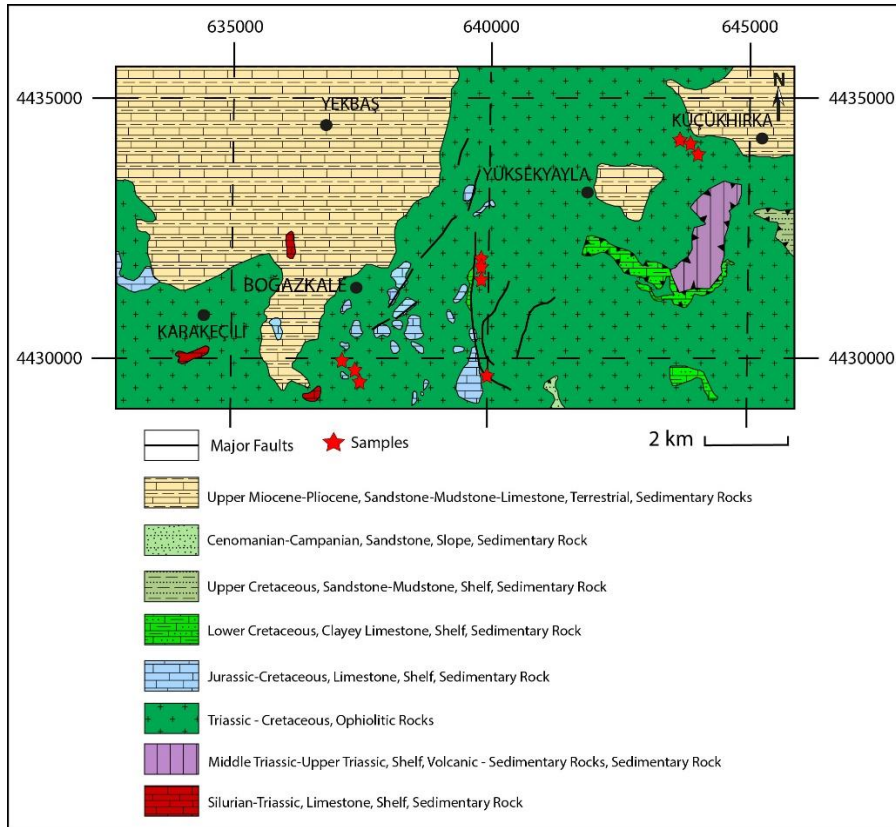


Figure 7. Geological map of the study area with the diabase samples collected from the field (map is modified from 1/100.000 Geological map of Turkey Publication, MTA, 2010).

The east of Boğazkale and southwest of the Yüksekayla Village are characterized by diabase dykes that cross-cut pillow basalts (Figure 7). Pillow basalts have very brecciated appearances and have brownish colors related with weathering (Figure 8a). However, some pillow basalts were not affected by weathering that much, which results in greenish colors (Figure 8b). Pillow lobes can be seen easily in the field (Figure 8). Diabase dyke has also very brecciated appearances (Figure 9). The width of the dyke is approximately 4.5m and it has greenish color (Figure 9a). Chilled margin and primary intrusion surface has been saved from alteration and it can be seen easily in the field (Figure 9b).



Figure 8. Field photographs of a) bracciated pillow basalt and b) bracciated pillow basalt cross-cut by a diabase dyke.



Figure 9. Field photographs of a) a diabase dyke intruding into basalt. b) closer view of the same dyke showing chilled margin and size difference from edge to core.

West of Küçükırka Village hosts diabase dykes which cross-cut gabbros (Figure 10). Field observations show that gabbros have been affected by surface alteration and they have a white color (Figure 10). Diabase dyke has a 5m width and it has a darker green color (Figure 10). It is very fractured and the fractures are mostly filled with calcite (Figure 11). Primary intrusion surface and chilled margins can still be observed despite the hydrothermal alteration (Figure 11). Furthermore, in spite of this alteration effect, several intrusions but having smaller widths of the diabase dyke into gabbro host rock can be easily seen (Figure 10 and 11).



Figure 10. Field photograph of a diabase dyke cross-cutting through a gabbro host rock.



Figure 11. Closer view of the diabase dyke cross-cutting gabbro in Figure 10.

South and southeast of Boğazkale host diabase dykes cross-cutting ultramafics (Figure 12). Ultramafic rocks are the parts of peridotite and these rocks have serpentinization and carbonatization as alteration processes. Ultramafic rocks which were not influenced by weathering so much have darker colors (Figure 12) but in some areas, weathering and intensive carbonatization mask the real color of those host rocks (Figure 14). The width of these dykes is approximately 10m. They have grayish colors in the field and they also have very fractured appearances (Figure 12). Moreover, they have chilled margins that can be observed easily in the field (Figure 13).



Figure 12. Field photograph of an ultramafic host rock cross-cut by a diabase dyke.



Figure 13. Field photograph of an ultramafic host rock cross-cut by a diabase dyke having chilled margin.



Figure 14. Another field photograph showing another diabase dyke cross-cutting carbonatized ultramafic rock.

These peridotite rocks are also cross-cut by diabase dykes which also cross-cut gabbros in west of Küçükhirka Village (Figure 15 and 16). In these ultramafic rocks, mesh texture can be seen easily and they have a darker green color which is masked by white colors due to carbonatization (Figure 15 and 16). The width of this dyke is approximately 1m which is smaller than the other ones and the color of diabase rocks is darker green (Figure 16). The host rock and diabase dyke have very fractured appearances (Figure 15 and 16). Furthermore, in field studies it is also observed that after intrusion of these dykes, the region has been affected by tectonic activities (Figure 17). This tectonic activity can be seen in the faulting of the diabases (Figure 17).



Figure 15. Field photograph of a diabase dyke intruding into ultramafic host rock.



Figure 16. Closer view of the diabase dyke cross-cutting into ultramafic host rock in Figure 15.



Figure 17. Field photograph showing faulting after intrusion of the diabase dyke.

## **CHAPTER 3**

### **PETROGRAPHY**

In order to deduce the petrographical features of the diabase dykes, 48 thin-sections were examined under the polarizing microscope. In addition, 6 thin-sections were prepared from the host rocks cross-cut by the dykes to infer their petrographic characteristics as well. The petrographical examination reveals two types of diabbases based on the presence of predominant mafic mineral phase. One of these types consists mainly of clinopyroxene as the major mafic phase and will be called hereafter “clinopyroxene-diabase”, whereas the ones that are dominated by amphibole will be called “amphibole-diabase”. This grouping is efficient for the samples which saved their primary minerals. However, some of the samples could not save their primary minerals because of the effect of hydrothermal alteration so that grouping according to petrographical features of those samples is not efficient. Therefore, actual grouping of these dykes were done according to geochemical results, which will be discussed in chapter 4. These diabase dykes cross-cut various ophiolitic lithologies, including pillow basalts, gabbros and ultramafics, whose petrographic features will also be given following the diabbases.

### **3.1. Diabase Dykes**

#### **3.1.1. Clinopyroxene-Diabases**

The clinopyroxene-diabases are phaneritic and holocrystalline. Their primary mineralogy is composed of mainly clinopyroxene and plagioclase. Plagioclase is mostly found as euhedral and subhedral lath-shaped crystals (Figure 18), while some of them display anhedral outlines. Under plane-polarized light (PPL), plagioclase appears colorless and has low relief. It shows first-order interference colors. Polysynthetic twinning is common. In some samples, there also are some large plagioclase phenocrysts with embayed textures, which may indicate resorption due to reaction with the melt (Figure 19). These diabases are characterized by equigranular fabric. However, in some cases, porphyritic appearances can be seen, including relatively large plagioclase or clinopyroxene crystals surrounded by finer-grained minerals. (Figure 18 and 19). The presence of porphyritic texture may imply two stage-cooling of magma. The first stage is characterized by relatively slow rates of cooling and responsible for the formation of the phenocrysts in deeper levels, while the second stage involves faster cooling rates and formed smaller crystals in probably shallower depths.

Clinopyroxene is colorless to green under PPL and has high relief. It shows maximum second-order interference colors with blues and pinks under XPL (Figure 20). Most of the clinopyroxene grains have elongated shapes which show one-directional cleavage (Figure 18). However, some basal sections of clinopyroxene grains display characteristic two-directional cleavage intersecting at  $\sim 90^\circ$ . Moreover, clinopyroxene displays large extinction angles exceeding  $40^\circ$ . In some places, plagioclase crystals are enclosed by larger clinopyroxene crystals, and exhibit sub-ophitic textures (Figure 20).

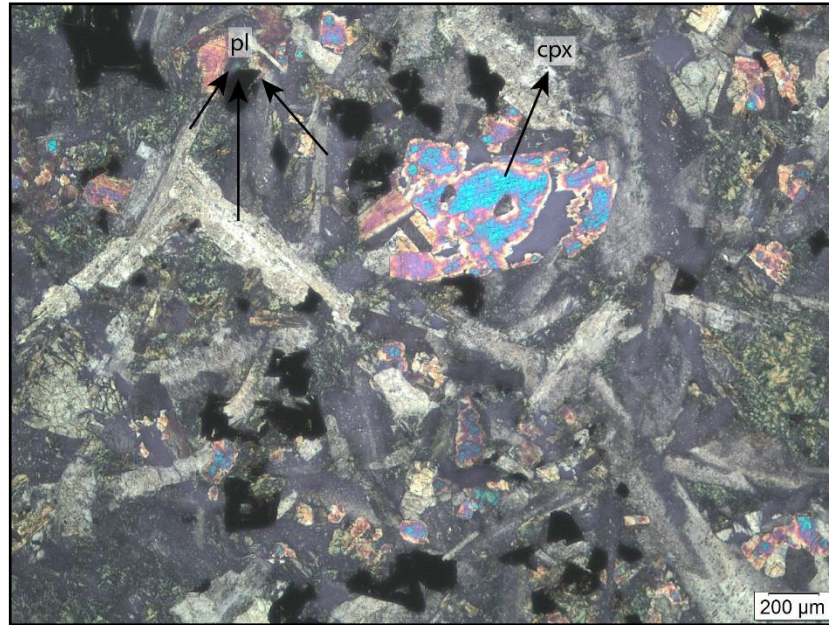


Figure 18. Thin section photograph of a clinopyroxene-diorite showing interference color difference of clinopyroxene and plagioclase minerals (Sample HT-14; 4X, XPL, pl: plagioclase, cpx: clinopyroxene).

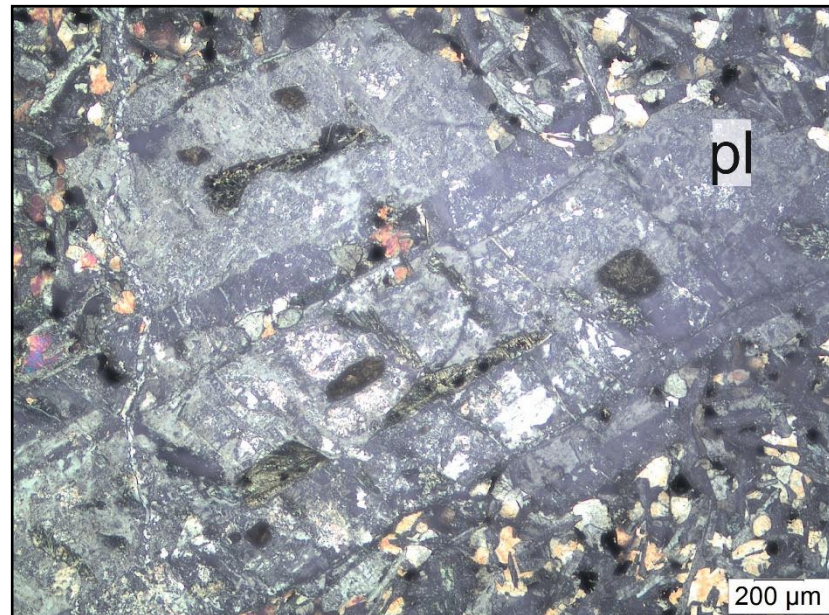


Figure 19. Plagioclase phenocrysts showing embayed texture (Sample 15-BOG-6; 4X, XPL, pl: plagioclase).

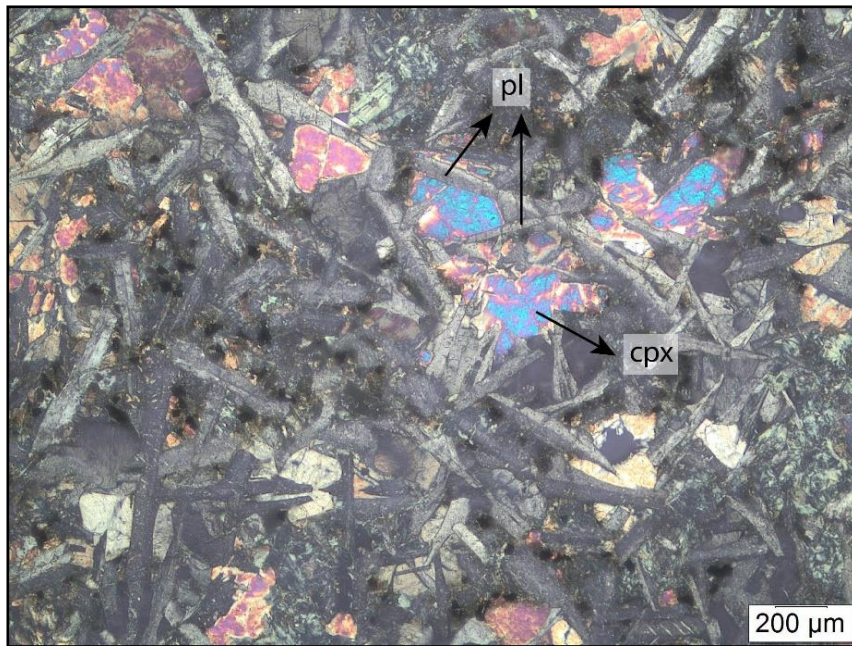


Figure 20. Plagioclase grains are partly enclosed by larger clinopyroxene, illustrating sub-ophitic texture (Sample 15-BOG-7; 4X, XPL, pl: plagioclase, cpx: clinopyroxene).

Chlorite, epidote and prehnite can be seen as alteration products in these diabbases. Chlorites are the alteration product of mafic minerals like pyroxene group minerals. This mineral have characteristic pale green color and showing very weak pleochroism under PPL and display low to moderate relief (Figure 21a). They show anomalous interference colors with browns, greens, which are characteristic for them under XPL (Figure 21b). They have perfect (001) cleavage which can be spotted in thin sections. Epidote shows a characteristic pistachio green color and high relief under PPL (Figure 21). It appears very fractured but its perfect one directional cleavage can also be seen with higher magnifications. It has moderate to high birefringence, showing low second to upper third-order interference colors (Figure 21b). Epidote is seen in the veins as an infilling product (Figure 21). The last secondary mineral in the first group is prehnite. Prehnite is a Ca-bearing mineral, and it is a typical alteration product after plagioclase. It also may also occur as a vein-filling mineral like epidote. In the clinopyroxene diabbases investigated, both occurrences of prehnite are encountered (Figure 21b). Prehnite is colorless under PPL, has low relief. It displays second-order

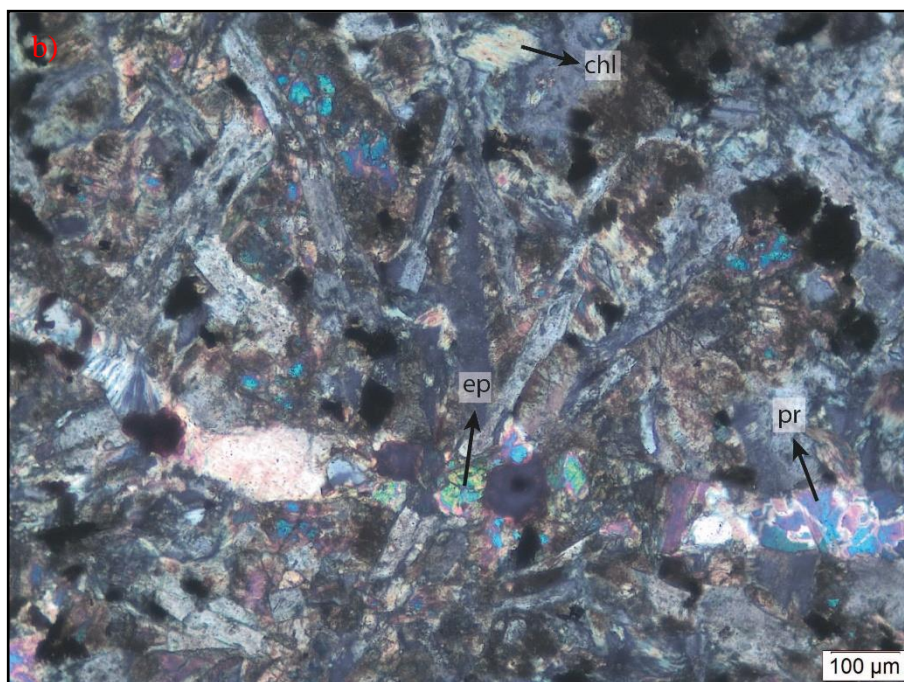


Figure 21. a) Clinopyroxene diabase characterized by low-grade alteration products including chlorite epidote and prehnite. Chlorite is seen variably replacing mafic phases, while epidote occurs as a vein-filling mineral b) Same sample showing the interference colors of chlorite, epidote and prehnite minerals (Sample 15-BOG-4B; 10X, a) PPL and b) XPL, ep: epidote, chl: chlorite, pr: prehnite).

interference colors under XPL (Figure 21b). Moreover, some of the veins were filled with secondary calcite minerals (Figure 22). Calcite is also colorless under PPL and has moderate relief. It has fourth-order interference colors.

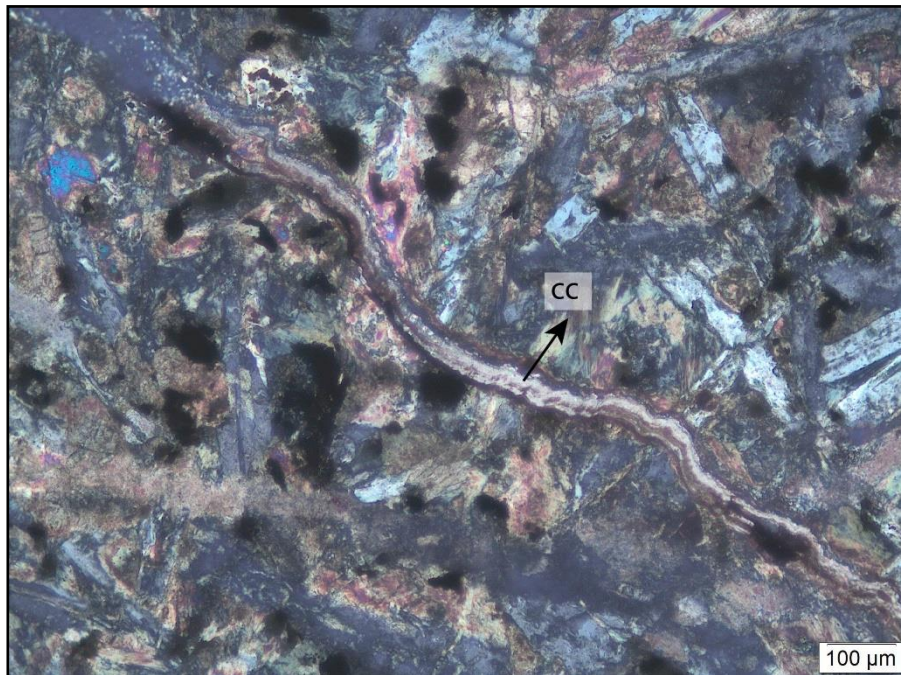


Figure 22. Thin section photograph illustrating calcite vein (Sample 15-BOG-4B; 10X, XPL, cc: calcite).

### 3.1.2. Amphibole-Diabases

Amphibole-diorite forms the second petrographic group in which amphibole occurs as the predominant mafic phase. These diorites are also phaneritic and holocrystalline. The primary minerals in this group are mostly hornblende and plagioclase, however some samples also contain subordinate amounts of clinopyroxene. Amphibole diorites largely display equigranular fabric.

Primary hornblendes have saved their euhedral shapes in some rocks which had been slightly altered (Figure 23) despite most of the rocks had been extremely affected by hydrothermal alteration (Figure 26). There can be seen chlorite and also actinolite in the

rims of these hornblendes but the cores are generally not affected by hydrothermal alteration (Figure 23). Hornblendes display variety of colors changing from green to light brown that shows their pleochroic character and moderate to high relief (Figure 23). While some hornblendes show one directional cleavages at some samples, others have two-directional cleavages and euhedral to subhedral shapes (Figure 23). They also have moderate interference colors and show simple twinning in some samples (Figure 25). As explained in clinopyroxene diabases, plagioclases are colorless and have first-order interference colors and clinopyroxenes are also colorless and have maximum second-order interference color.

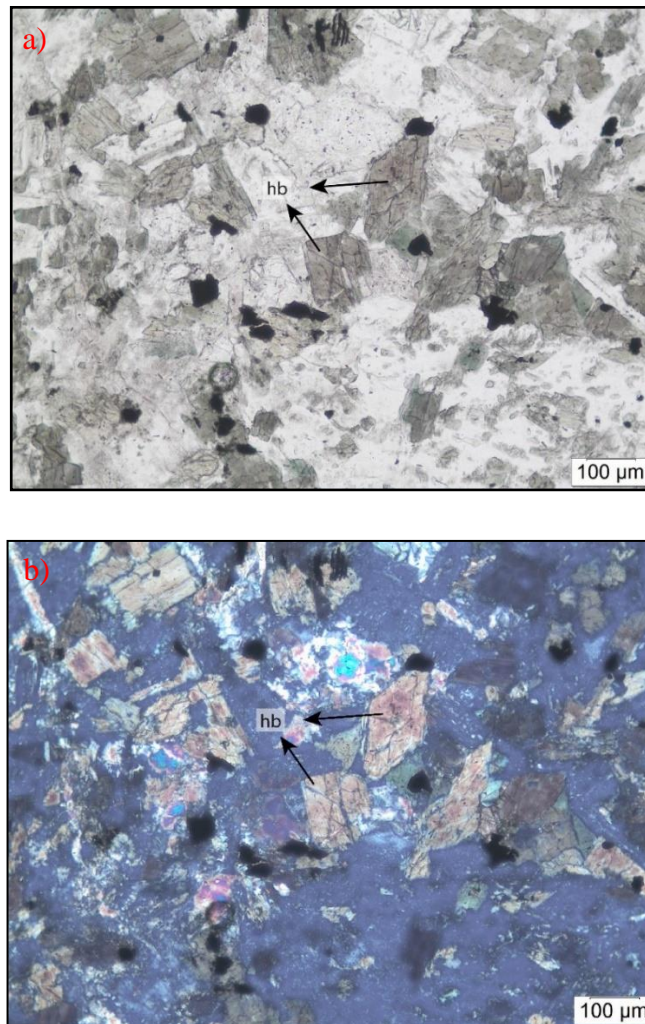


Figure 23. a) Amphibole-diabase including primary hornblendes illustrating brownish colors. b) same view under XPL showing moderate interference color of hornblende (Sample HT-20-A; 10X, a) PPL and b) XPL, hb: hornblende).

Poikilitic texture rarely occurs and it is characterized by plagioclase enclosing smaller clinopyroxene grain (now altered) (Figure 24). Poikilitic texture refers to different nucleation rates of different minerals (Winter, 2001). The example in the Figure 24 shows a poikilitic texture where clinopyroxene probably crystallized firstly, then plagioclase enclosed clinopyroxene. Finally, clinopyroxene was replaced by actinolite owing to low-grade alteration. As alteration products, primary amphiboles were replaced by chlorite and actinolite (Figure 26) and plagioclases were replaced by prehnite minerals (Figure 26b). Actinolite is an amphibole group mineral having pleochroism in shades of green and moderate relief under PPL (Figure 26b) and moderate interference colors under XPL (Figure 26). It has (110) perfect cleavage and oblique extinction at around  $10^{\circ}$ - $15^{\circ}$  degrees. The habit of actinolites may be as fibrous crystals (Figure 26).

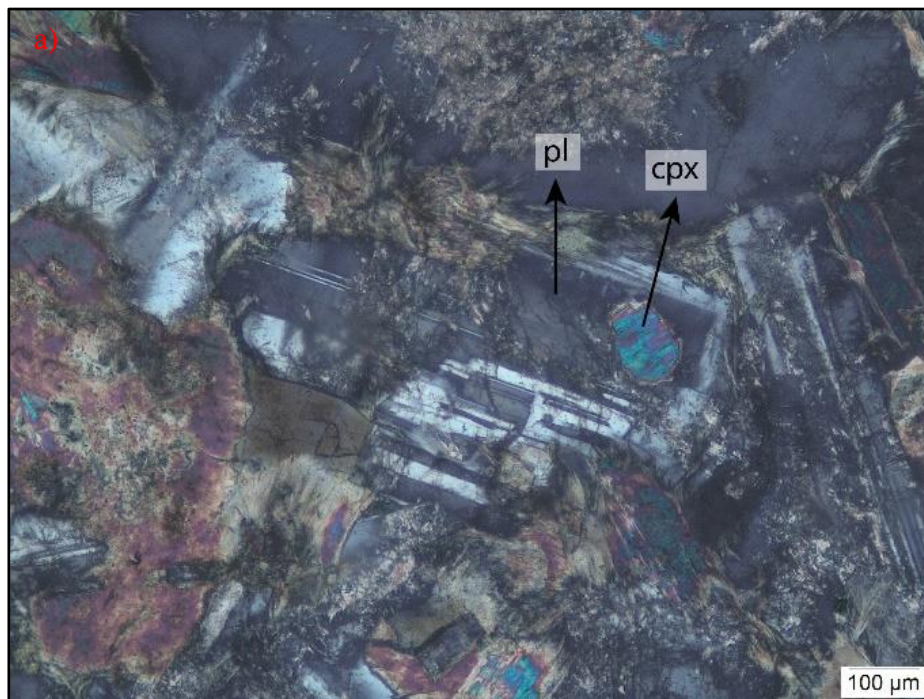


Figure 24. Remnant poikilitic texture characterized by clinopyroxene grain (now altered to actinolite) enclosed by a larger plagioclase (Sample HT-19; 10X, a) XPL and b) PPL, pl: plagioclase, cpx: clinopyroxene).



Figure 24. Cont'd.

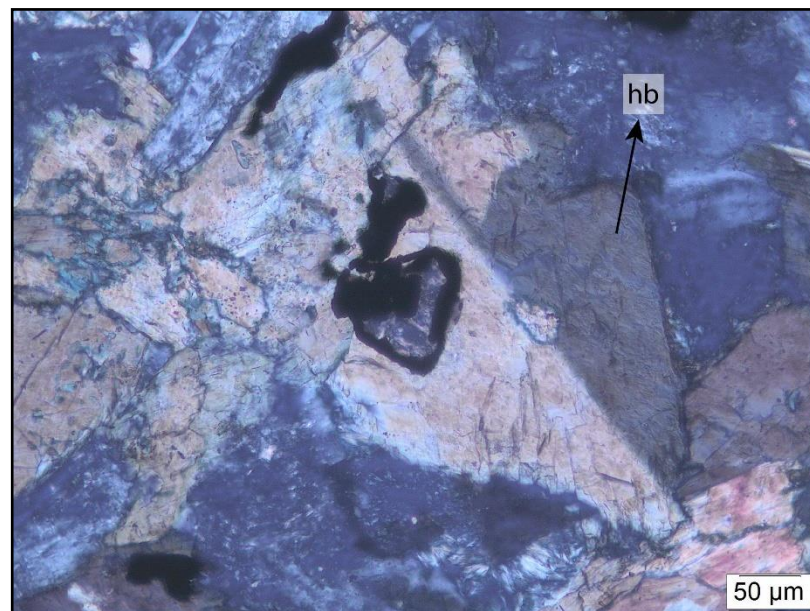


Figure 25. Thin section photograph of a primary hornblende showing simple twinning (Sample HT-20-B; 20X, XPL, hb: hornblende).

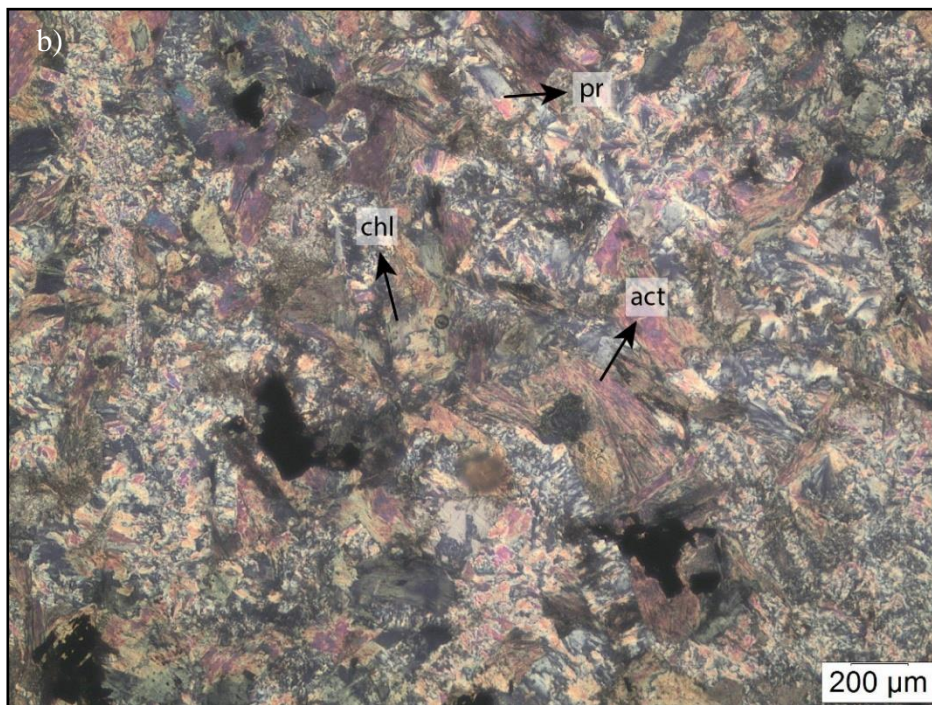
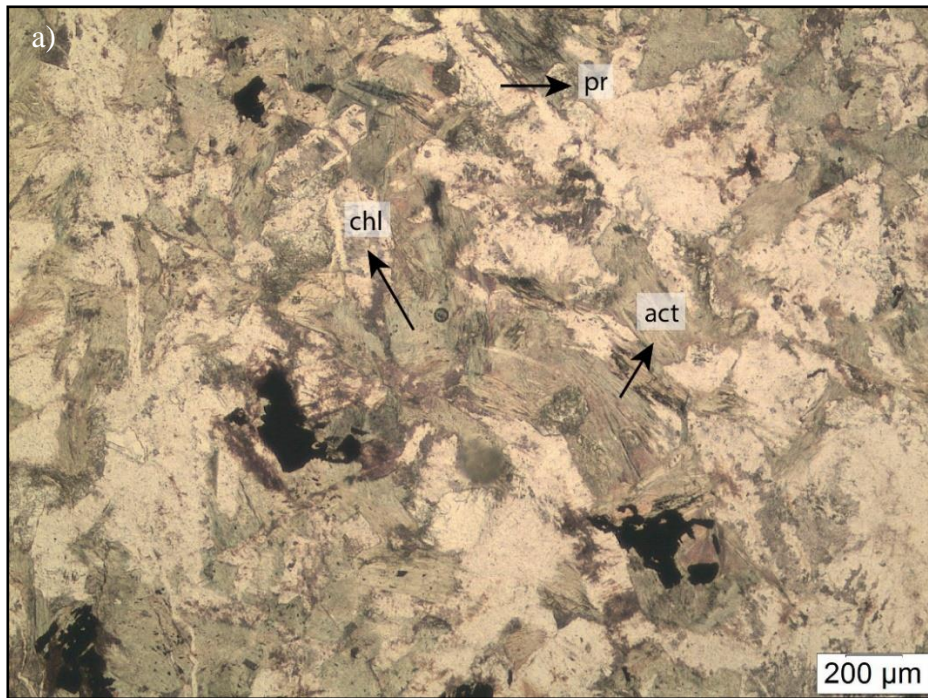


Figure 26. a) Thin section photograph illustrating color difference of chlorite, prehnite and actinolite. b) XPL appearance of the same view but displaying interference color difference of the same minerals (Sample 15-BOG-8; 4X, a) PPL and b) XPL, chl: chlorite, pr: prehnite, act: actinolite).

Primary biotites which are the replacement products after hornblendes are also spotted in the second group (Figure 27). For these biotites, brownish colors and pleochroism of colorless to brownish colors, are displayed very clear under PPL (Figure 27a). Moreover, (001) perfect cleavage and moderate relief can be seen under PPL (Figure 27a). High birefringence and mottled extinction which is the characteristic feature of micas can be seen under XPL (Figure 27b). These biotites are also replaced by chlorites owing to alteration processes.

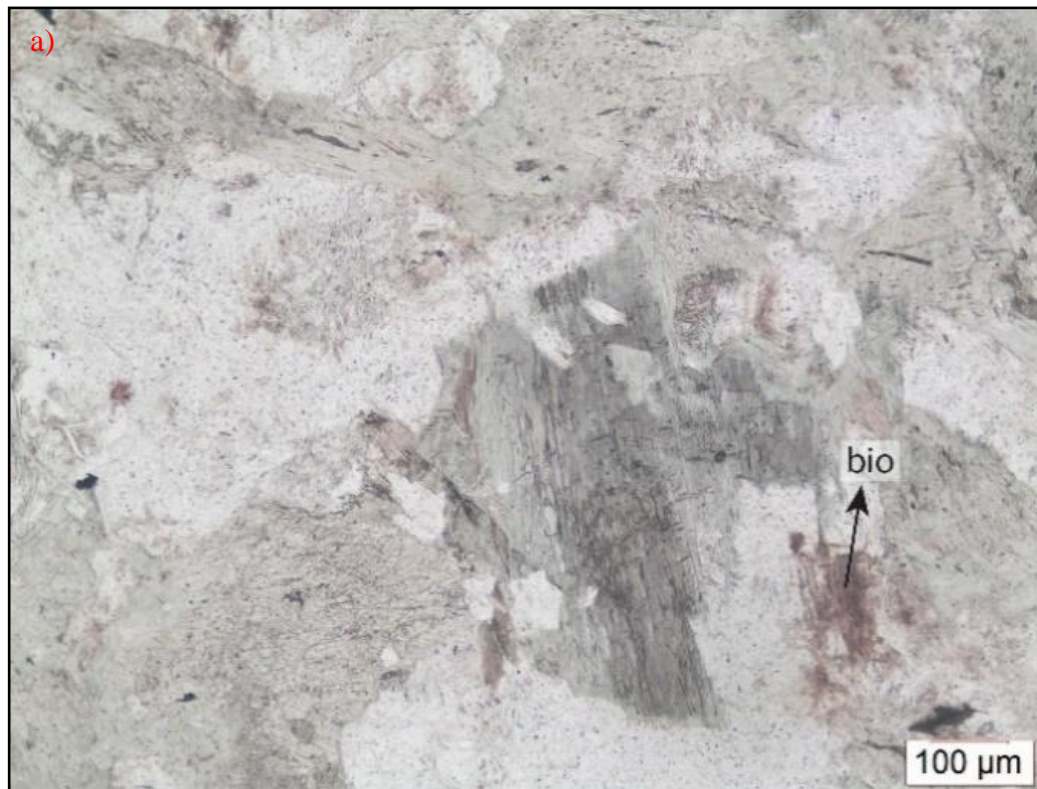


Figure 27. Thin section showing biotite mineral a) showing brownish color and b) showing mottled extinction (Sample 15-BOG-8; 10X, a) PPL and b) XPL, bio: biotite).

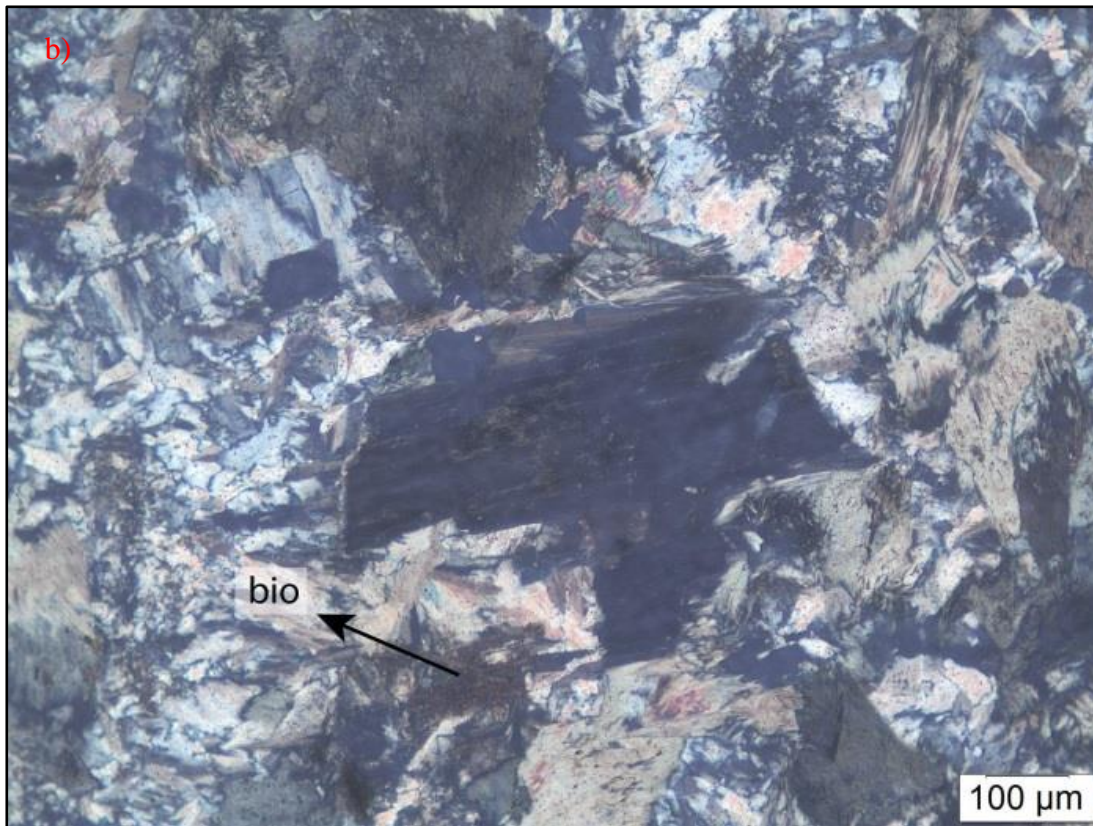


Figure 27. Cont'd.

### 3.2. Host Rocks

Pillow basalts, gabbros and ultramafics are intruded by the diabbases in the study area. In this parts, same minerals which were covered in diabase dyke parts will not be explained again. Pillow basalts are are phaneritic and holocrystalline. They display porphyritic texture with larger clinopyroxene crystals embedded in a finer-grained groudmass. Clinopyroxenes and plagioclases are the primary minerals in basalts (Figure 28). Sub-ophitic texture can also be seen in relation with clinopyroxene and plagioclase crystals (Figure 28). Moreover, the effects of hydrothermal alteration can also be seen in basalts as secondary minerals such as chlorites and actinolites (Figure 29).

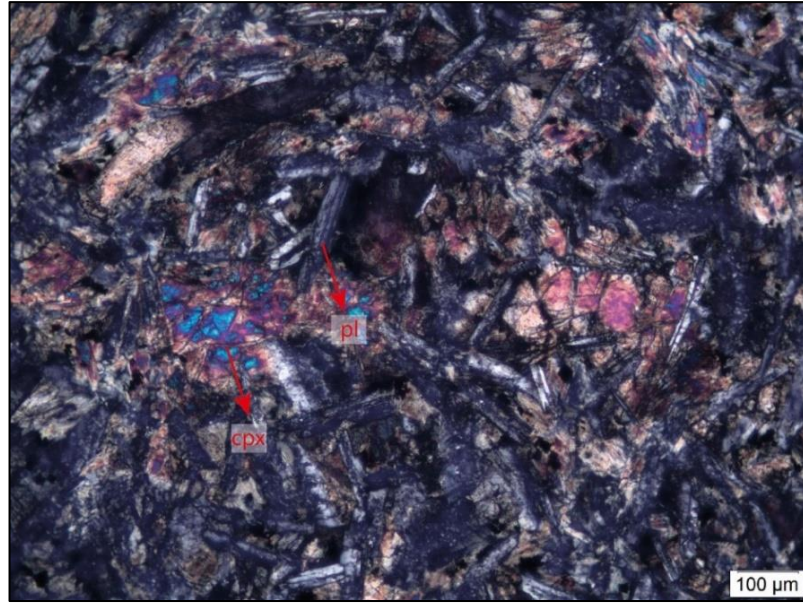


Figure 28. Thin section photographs of a basalt showing clinopyroxenes and plagioclases with sub-ophitic texture (Sample 15-BOG-5; 10X, XPL, cpx: clinopyroxene, pl: plagioclase).

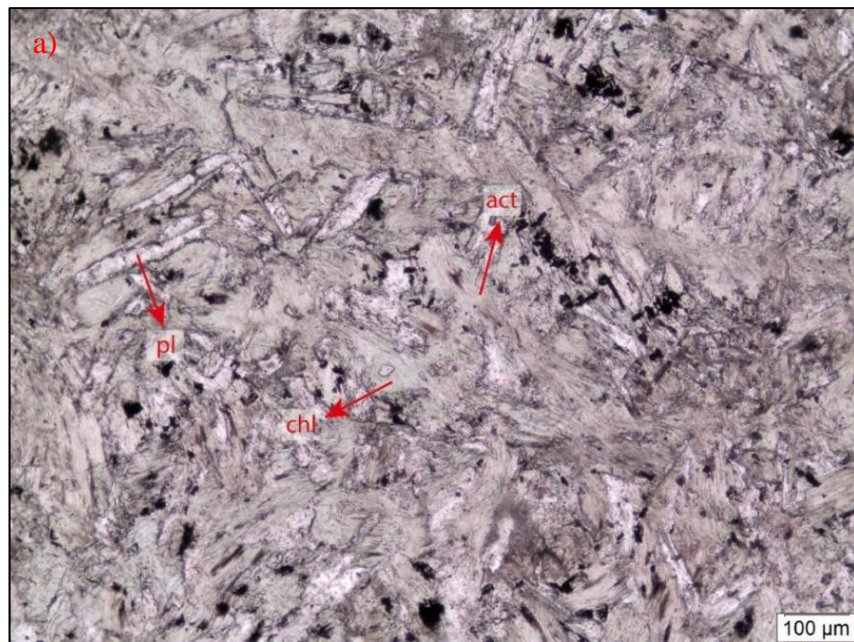


Figure 29. a) Thin section photograph of a basalt showing plagioclase and the color difference of secondary actinolite and chlorite and b) interference color difference of chlorite and actinolite (Sample 15-BOG-5; 10X, a) PPL and b) XPL, act: actinolite, chl: chlorite, pl: plagioclase).

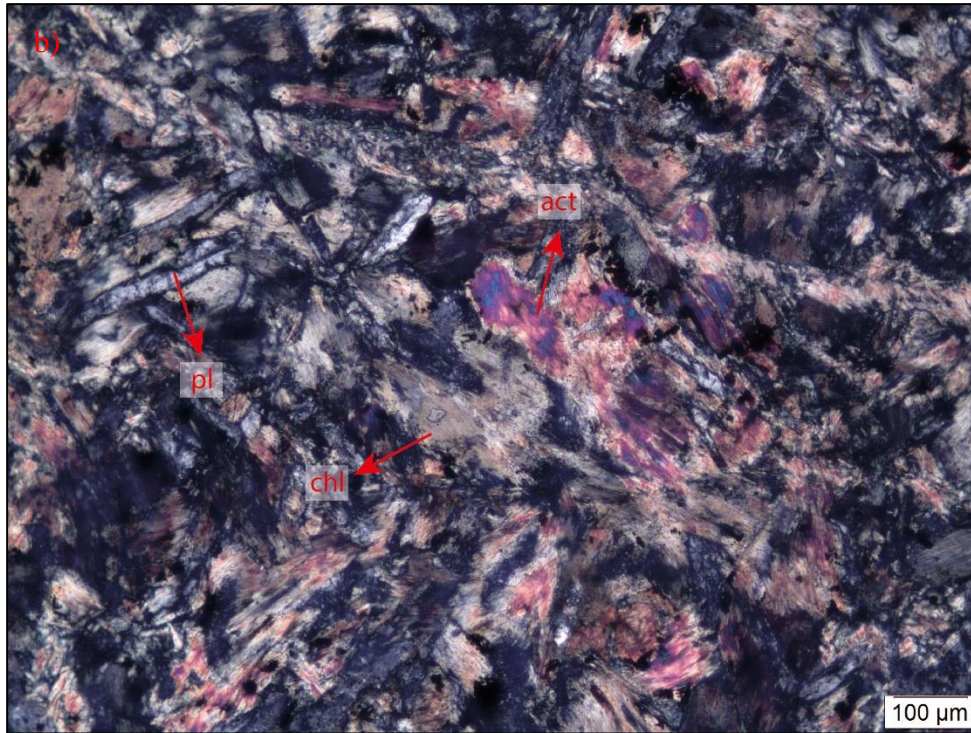


Figure 29. Cont'd.

Gabbros are phaneritic and holocrystalline. Porphyritic texture is also the common fabric in thin sections of them with larger clinopyroxene crystals and smaller plagioclase laths (Figure 30). Clinopyroxenes and plagioclases are also the primary minerals for gabbros (Figure 30). The effect of hydrothermal alteration can also be seen from secondary minerals such as chlorite and epidote (Figure 30 and 31). Epidotes can also found as veins (Figure 31).

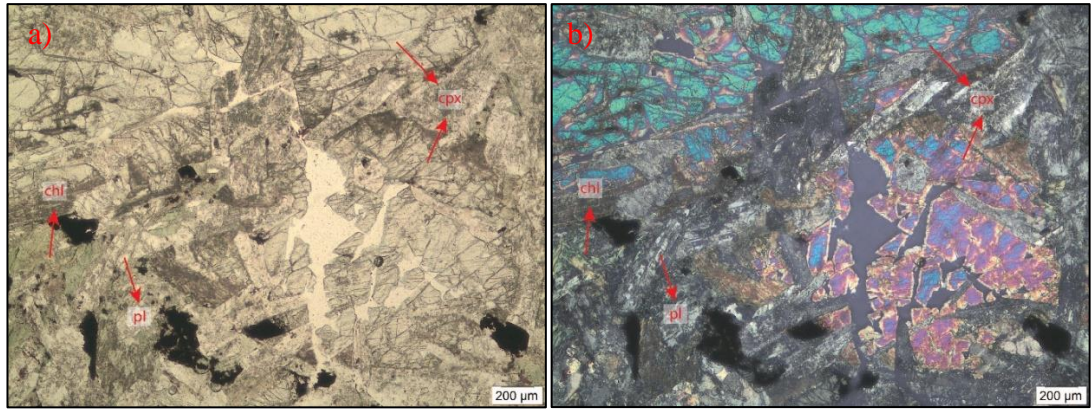


Figure 30. Thin section photographs of a gabbro showing clinopyroxene and plagioclase minerals and secondary chlorite minerals under PPL and XPL (Sample 15-BOG-2; 4X, a) PPL and b) XPL, ol: olivine, pl: plagioclase, chl: chlorite).

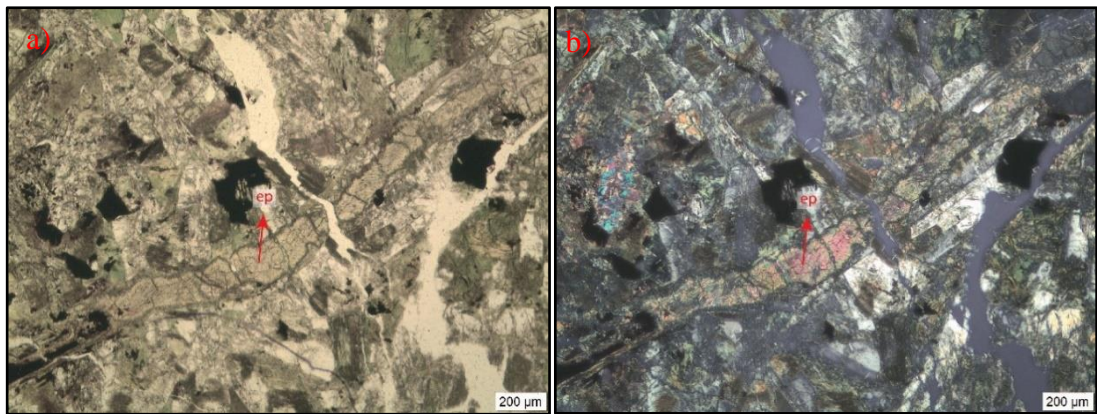


Figure 31. Thin-section photograph of a gabbro showing vein-filling epidote with a) pistachio green color and high relief and b) upper third-order interference color (Sample 15-BOG-2; 4X, a) PPL and b) XPL, ep: epidote).

Ultramafic rocks are represented by serpentinites and carbonatized peridotites. Serpentinized ultramafics are composed mainly of serpentine minerals (Figure 32). Serpentine minerals are colorless to pale green minerals and low relief (Figure 32a). They have first-order interference colors (Figure 32b). On the other hand, carbonatized ultramafics contain primary clinopyroxenes and secondary calcites (Figure 33).

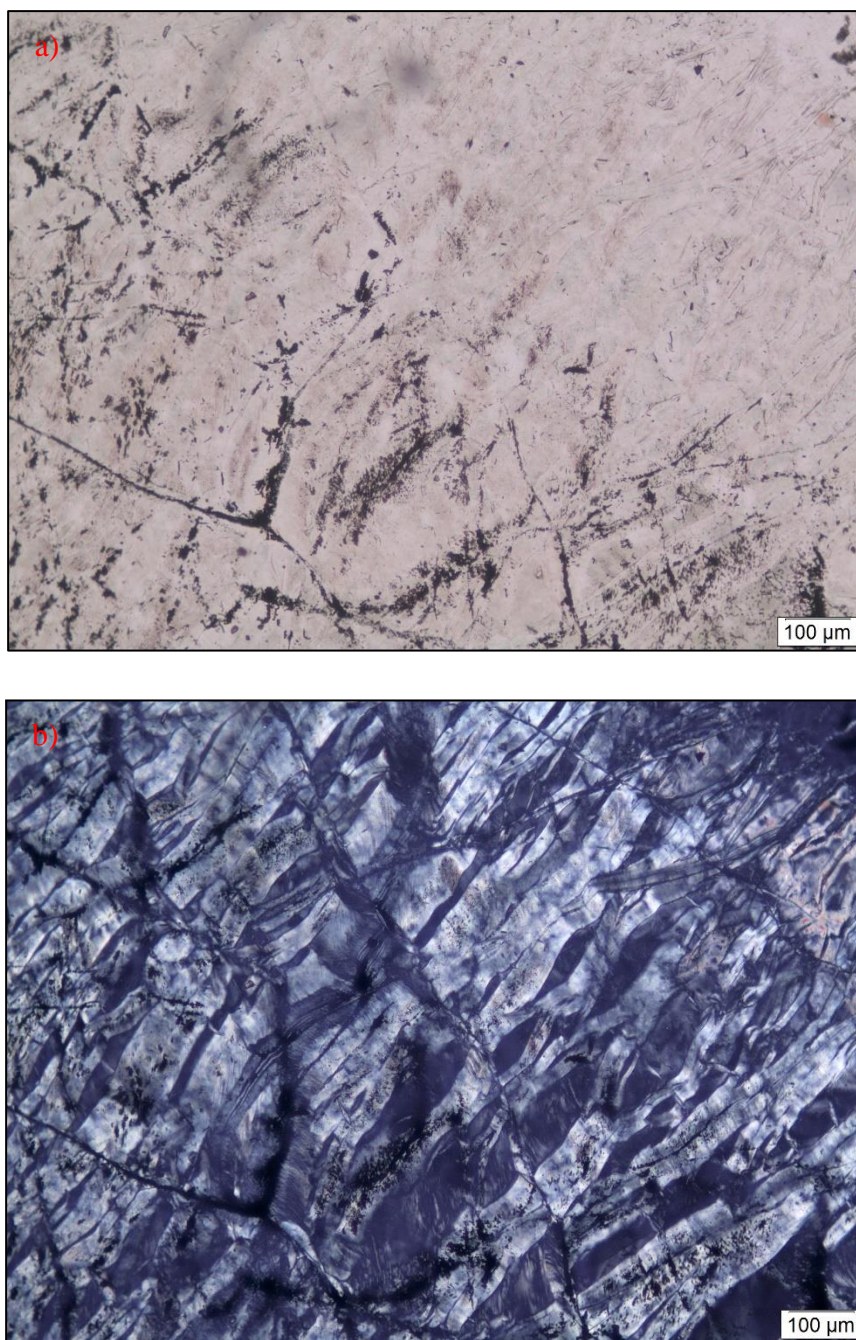


Figure 32. A thin section example of a serpentinite showing a) colorless to pale green colors and b) first-order interference colors (Sample 17-BOG-7; 10X, a) PPL and b) XPL).

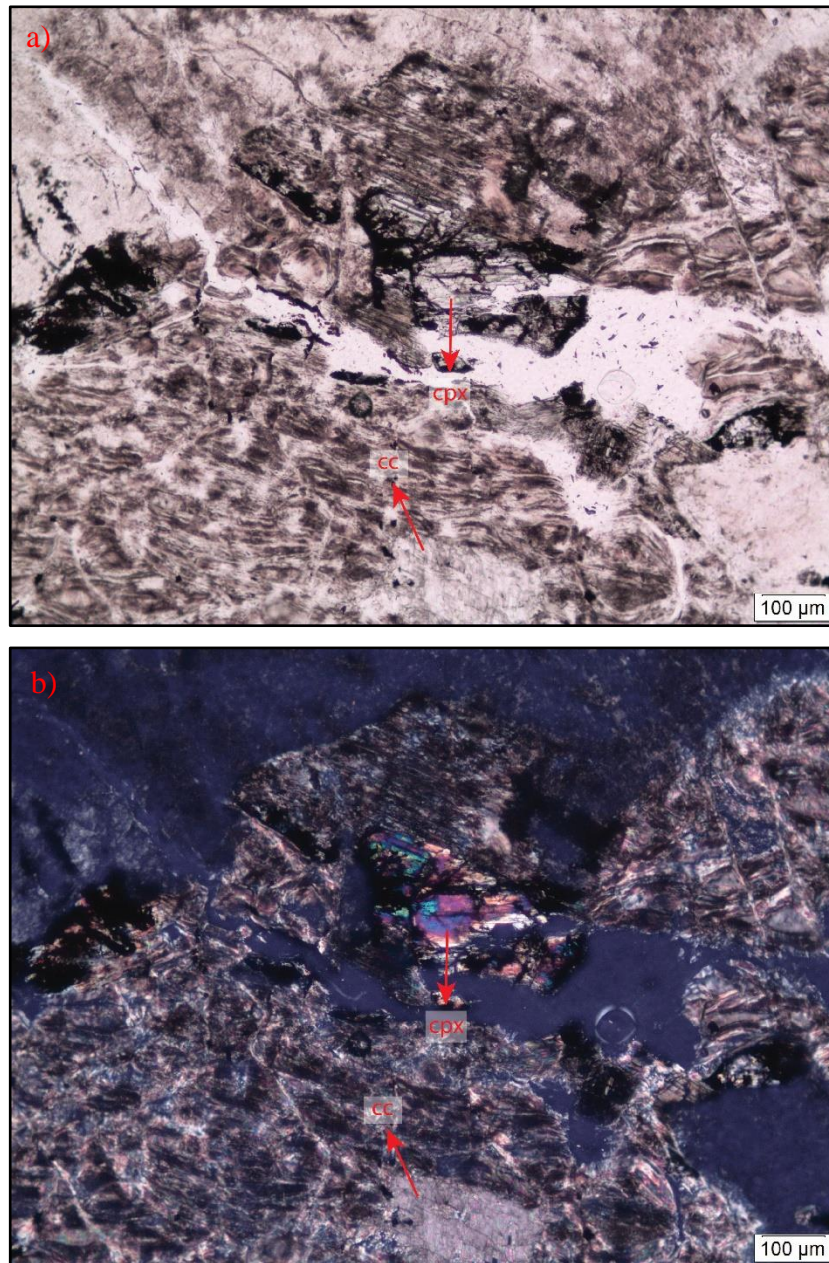


Figure 33. Thin section photograph showing primary clinopyroxene and secondary calcite (Sample 17-BOG-1; 10X, a) PPL and b) XPL, cpx: clinopyroxene, cc: calcite).



## **CHAPTER 4**

### **GEOCHEMISTRY**

#### **4.1. Introduction**

In this chapter, a total of 15 diabase samples from the Hattuşaş ophiolitic mélange, Çorum region were analyzed in order to understand the rock composition, effect of fractional crystallization, mantle source features, and tectonic environment by using a variety of diagrams, including such as harker, multi-element and tectonic discrimination diagrams.

#### **4.2. Analytical Methods and Assessment of Alteration**

The whole-rock geochemical analyses were performed by the Activation Laboratories Ltd. (Ancaster, Ontario, Canada). The analyses of 15 diabase samples were measured by inductively-coupled plasma optical emission spectrometry (ICP-OES) and inductively-coupled plasma mass spectrometry (ICP-MS) methods after lithium metaborate/tetraborate fusion. Major oxides were analysed by ICP-OES, while trace elements were analysed by using either ICP-OES or ICP-MS. The results are given in the appendix. All oxide values were recalculated on volatile-free basis in order to remove the effect of loss on ignition (LOI).

$^{40}\text{Ar}/^{39}\text{Ar}$  incremental heating analyses of two diabase rock (HT-16 and HT-20-A) were performed by Oregon State University Geochronology Laboratories. Primary single hornblende crystals were separated and analyzed according to incremental

heating method by means of Thermo Scientific Model ARGUS-VI-D instrument. The system is equipped with an air-cooled 25W Synrad CO<sub>2</sub> laser with industrial scan head for performing gas extractions. This system has a maximum laser power which is sufficient for the fusion of single crystals and flux monitors. Extraction method of the experiments is bulk laser heating. Durations of heating and isolation are 64 sec. and 3 min., respectively. All age equations were taken from Min et al. (2000).

LOI values are generally high ranging from 1.89 to 5.21, which is consistent with the fact that the samples are hydrothermally altered as revealed by the petrography (see Chapter 3 for details). Therefore, mobile major elements must be considered very carefully in order not to misunderstand the processes (e.g. Wood et al., 1976; Thompson, 1991). Most of the samples were influenced by low-grade hydrothermal alteration which may affect the content of mobile elements, the Large Ion Lithophile elements (LILE) (e.g. K, Rb, Cs, Ba) (e.g. Hart et al., 1974; Thompson, 1991) (Figure 34). Therefore, LILE cannot be used to classify the samples. Instead, High Field Strength Elements (HFSE) (e.g. Th, U, Ce, Zr, Hf, Ti, Nb, Ta) and REE (Rare Earth Elements) are used for the classification of the investigated samples due to their immobility character (e.g. Floyd and Winchester, 1978). Bivariate diagrams based on Zr versus trace elements and major oxides are used to show the effect of the hydrothermal alteration (Figure 34). The diagrams of Zr vs. K<sub>2</sub>O (Figure 34b) and Zr vs. Ba (Figure 34c) indicates this alteration effect by means of a wide range distribution of the samples. On the other hand, the diagrams of Zr vs. TiO<sub>2</sub> (Figure 34a), Zr vs. Hf (Figure 34d), Zr vs. Sm (Figure 34d) and Zr vs. Th (Figure 34f) show nice linear trends, which proves the immobility of these HFSE. Furthermore, the multi-element diagram shows incoherent distribution in mobile elements (Sr, K, Ba, Rb) in all Type 1 samples and almost all Type 2 samples except from the samples which were not affected from alteration so much (Figure 35).

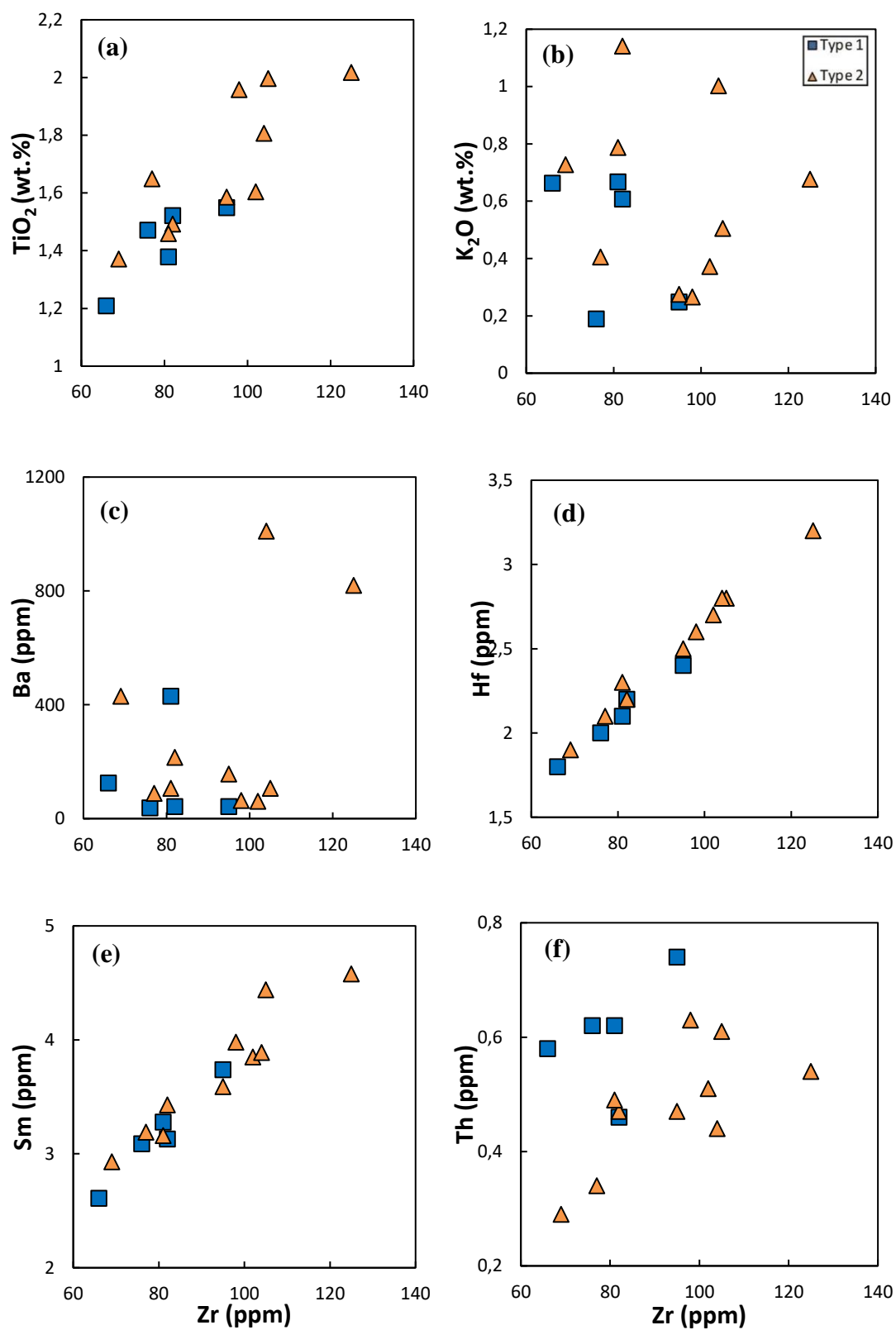


Figure 34. Distribution of selected major and trace elements against Zr.

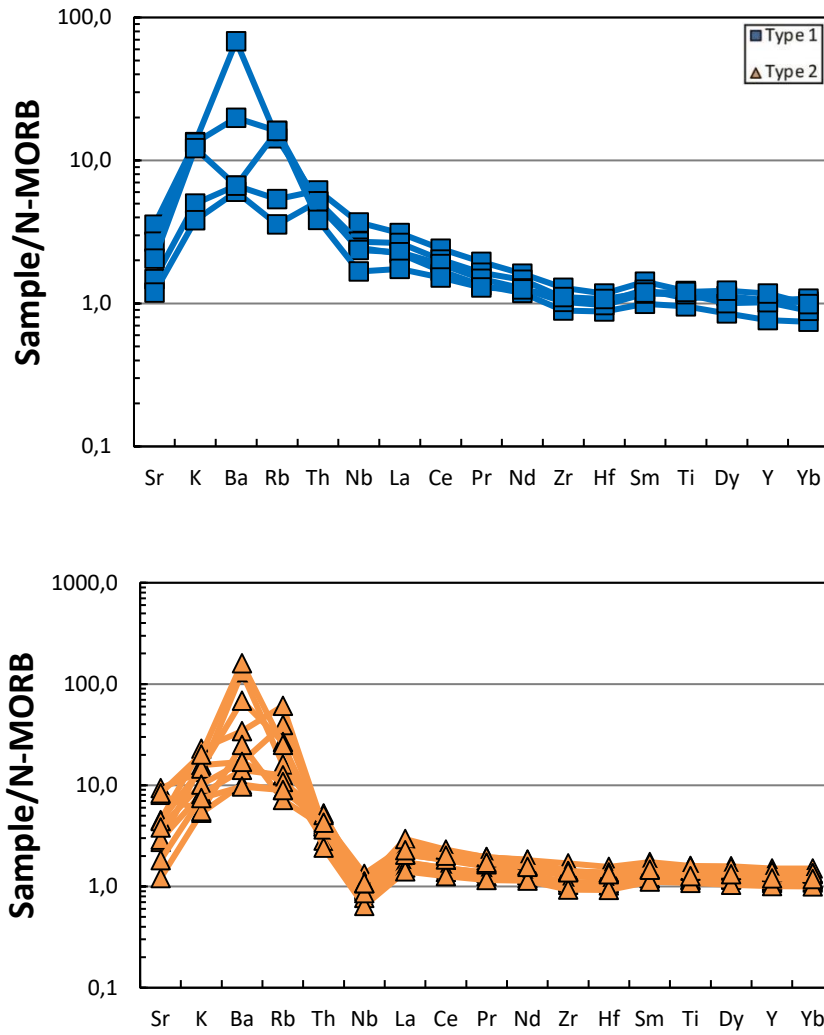


Figure 35. Multi-element diagram illustrating distributed appearances in mobile elements such as Sr, K, Ba and Rb.

#### 4.3. Classification

The Nb/Y vs. Zr/TiO<sub>2</sub> diagram (Winchester and Floyd 1977 modified by Pearce 1996), instead of TAS diagram, is used in order to classify the rocks (Figure 36) because mobile elements (Alkalis (Na<sub>2</sub>O and K<sub>2</sub>O) and SiO<sub>2</sub>) of TAS diagram would give wrong results under the effect of hydrothermal alteration. For this reason, trace element systematics are used to classify those diabbases since immobile trace elements like in the Nb/Y vs. Zr/TiO<sub>2</sub> diagram are not affected from hydrothermal alteration easily, which helps to get correct classification results. According to this diagram, all samples

are classified as subalkaline basalts ( $Nb/Y=0.2-0.3$  for Type 1;  $Nb/Y=0.05-0.08$  for Type 2) (Figure 36). For the subdivision of subalkaline basalts, the AFM diagram again may give wrong information because of the mobility of elements (Alkalis, FeO and MgO) so AFM diagram cannot be used in this purpose. Further subdivision of subalkaline basalts as calc-alkaline or tholeiitic basalts will be discussed in later petrogenesis parts.

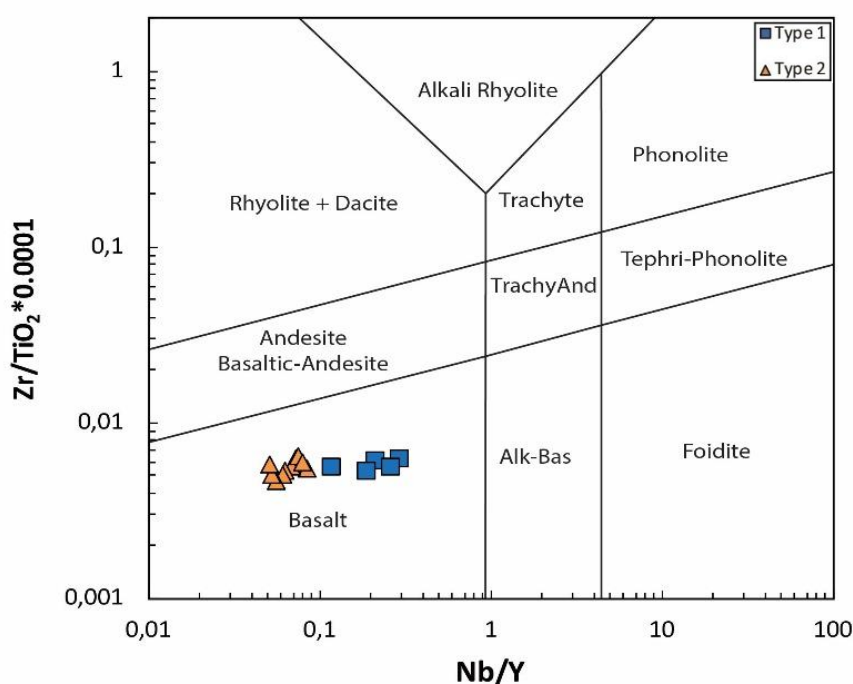


Figure 36. Classification diagram of relatively immobile elements (Winchester and Floyd (1977) modified by Pearce (1996)).

#### 4.4. Elemental Variations

##### 4.4.1. Major Oxides

All the diabase samples investigated have a wide range of  $SiO_2$  (wt.%) contents from 49.6 to 56.5 (from 50.2 to 51.8 for Type 1 and from 49.6 to 56.5 for Type 2),  $MgO$  (wt.%) content ranging from 4.16 to 8.81 (from 6.82 to 8.63 for Type 1 and from 4.16 to 8.81 for Type 2) and  $CaO$  (wt.%) content ranging from 5.10 to 11.4 (from 8.15 to

10.0 for Type 1 and 5.10 to 11.4 for Type 2). On the other hand,  $P_2O_5$  (wt.%),  $TiO_2$  (wt.%) and  $Na_2O$  (wt.%) values of all the samples have narrower ranges.  $P_2O_5$  (wt.%) content of all samples is ranging from 0.11 to 0.21 (from 0.13 to 0.17 for Type 1 and 0.11 to 0.21 for Type 2).  $TiO_2$  (wt.%) content of all samples is ranging from 1.21 to 2.02 (from 1.21 to 1.55 for Type 1 and from 1.37 to 2.02 for Type 2) and  $Na_2O$  (wt.%) content is ranging from 2.59 to 5.73 (from 3.23 to 3.61 for Type 1 and from 2.59 to 5.73 for Type 2) (Figure 37).

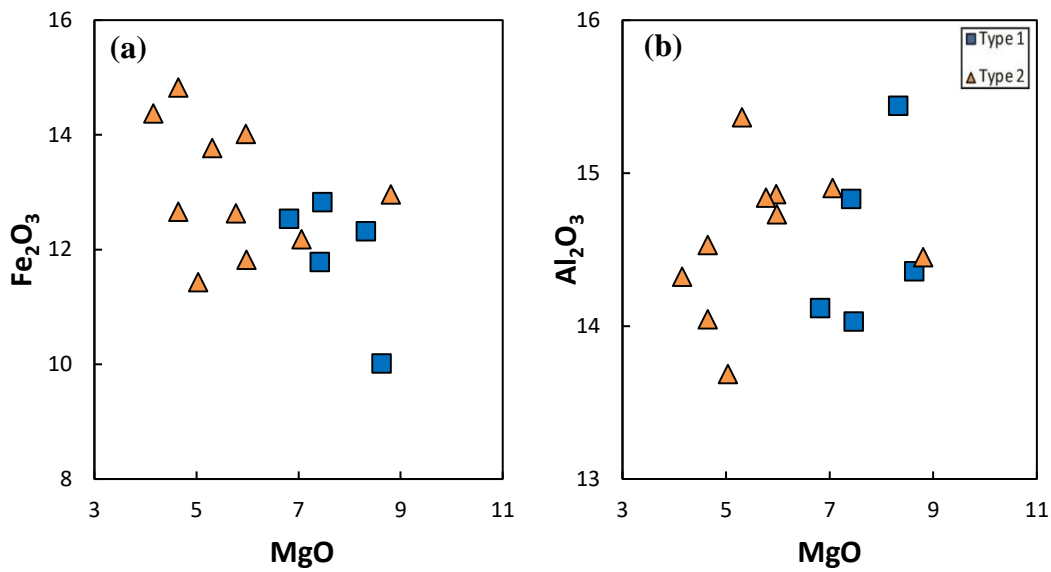


Figure 37. Major oxides (wt.%) variation diagrams of the selected samples.

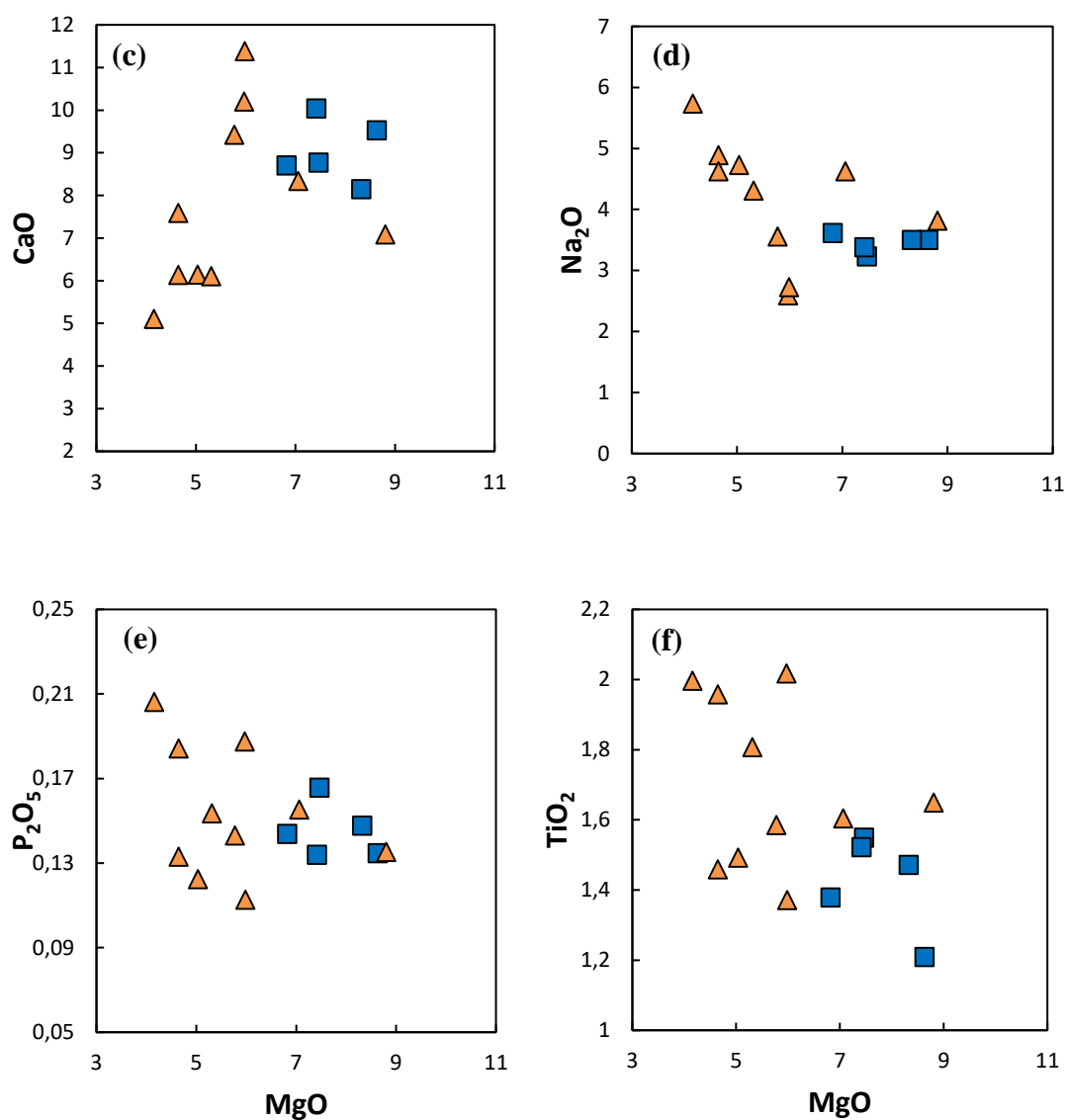


Figure 37. Cont'd.

#### 4.4.2. Trace Elements

Ni (ppm) values range from 60-110 for Type 1 and 20-170 for Type 2. Co (ppm) content having narrower ranges than Ni (ppm) from 37-46 for Type 1 and 29-43 for Type 2. Furthermore, Sc (ppm) and V (ppm) values are 38-43 and 246-342 for Type 1 and 34-40 and 322-482 for Type 2, respectively. Lastly, Y (ppm) and Zr (ppm) show ranges from 21.4-32.9 and 66-95 for Type 1 and 28.3-42.1 and 69-125 for Type 2.

These values are also variant in other trace elements (eg. Th (ppm) = 0.46-0.74, Sm (ppm) = 2.61-3.74, Eu (ppm) = 0.99-1.30, Hf (ppm) = 1.80-2.40 for Type 1; Th (ppm) = 0.29-0.63, Sm (ppm) = 2.93-4.58, Eu (ppm) = 0.86-1.61, Hf (ppm) = 1.9-3.2 for Type 2) (Figure 38).

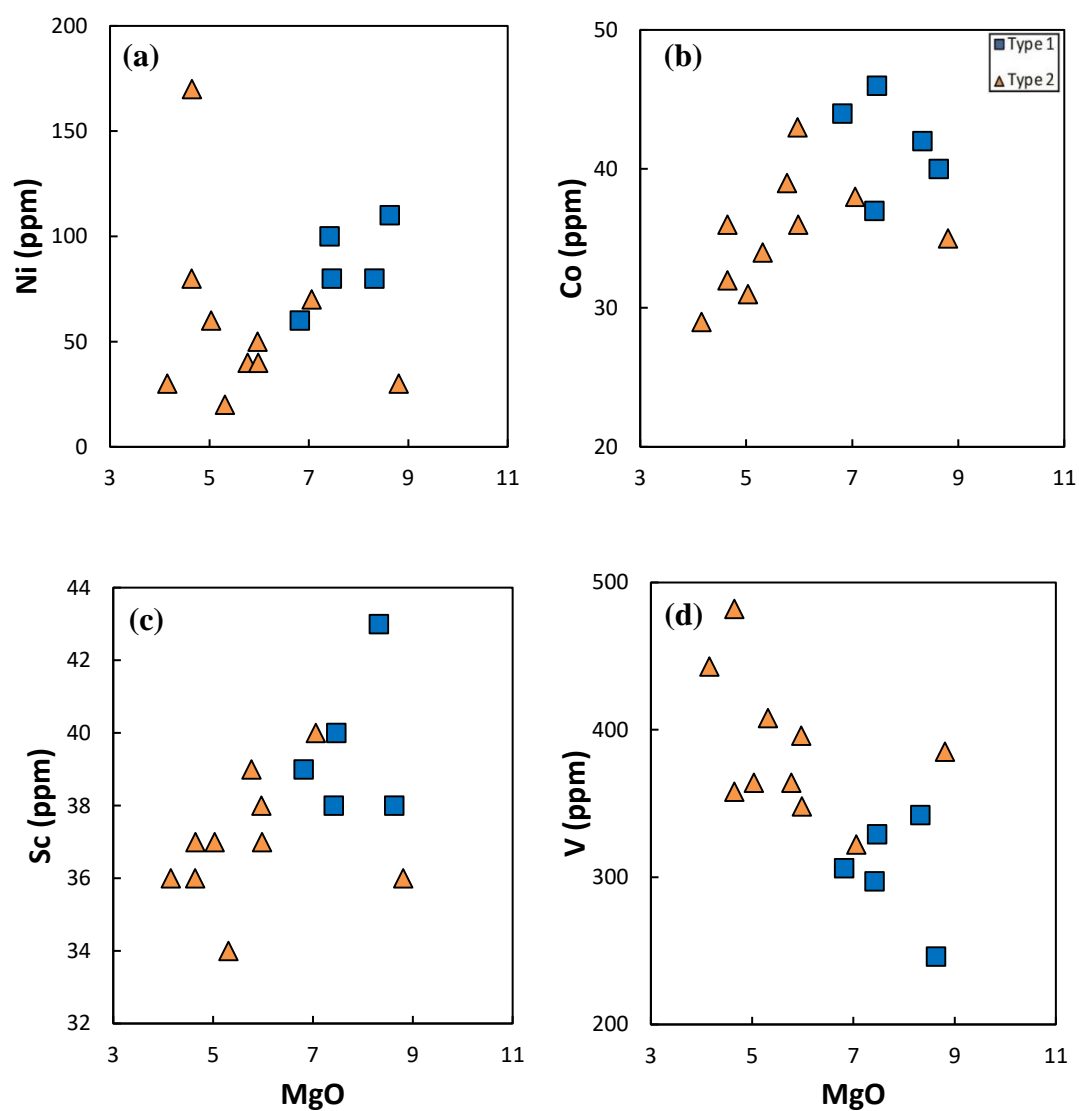


Figure 38. Variation diagram of MgO (wt.%) vs. trace elements of the selected samples.

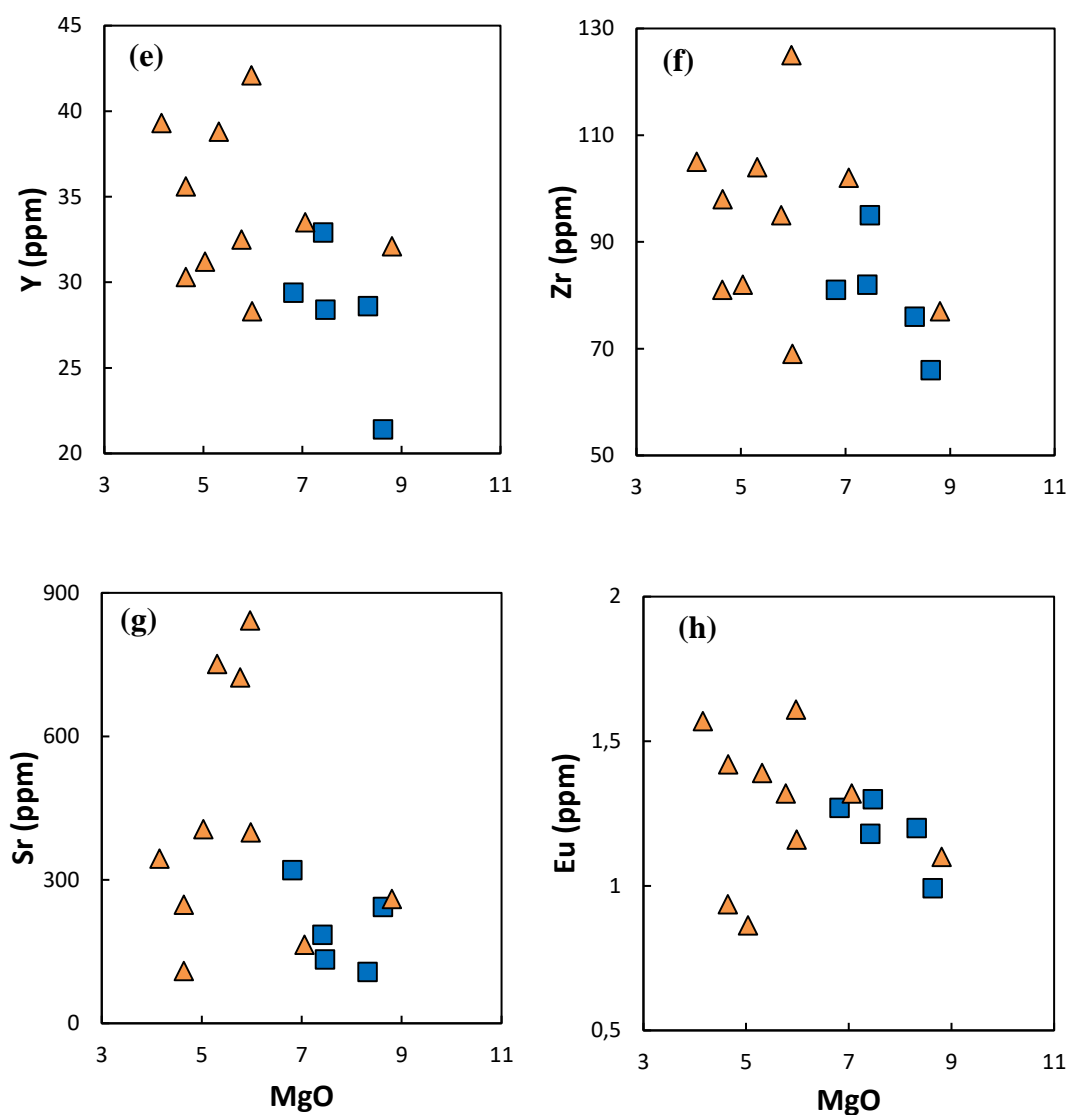


Figure 38. Cont'd.

Variations in the trace elements were also examined by plotting them on the N-MORB (Normal Mid-Ocean Ridge Basalt)-normalized multi-element and Chondrite-normalized REE diagrams. N-MORB-normalized multi-element patterns were plotted containing only HFSE in order to reduce the effect of alteration. Both Type 1 and Type 2 diabases have enrichment in Th and LREE relative to N-MORB (Figure 39). On the other hand, almost all the samples show a similar trend with N-MORB in Zr, Hf, Sm, Ti, Y and HREE) (Figure 39). Some Type 1 samples show slight depletion relative to

N-MORB in Zr, Hf, Ti, Dy, Y, Yb (Figure 39), while some Type 2 samples are depleted relative to N-MORB in Nb (Figure 39). An important difference observed between two types appears to be the presence of negative Nb anomaly in Type 2 samples. Therefore, Type 2 samples are characterized higher Th/Nb ratios compared to Type 1 and both are higher than that of N-MORB, E-MORB (Enriched Mid-Ocean Ridge Basalts) and OIB (Ocean Island Basalts) ( $\text{Th/Nb} = 0.09\text{-}0.12$  for Type 1;  $\text{Th/Nb} = 0.17\text{-}0.29$  for Type 2; 0.052 for N-MORB (Sun and McDonough, 1989); 0.072 for E-MORB (Sun and McDonough, 1989); 0.08 for OIB (Sun and McDonough, 1989)). Another difference is that Type 1 is more enriched in Nb relative to Type 2, resulting in lower Zr/Nb ratios in Type 1 ( $\text{Zr/Nb} = 11.1\text{-}21.0$  for Type 1;  $\text{Zr/Nb} = 31.5\text{-}52.0$  for Type 2). Type 1 has lower Zr/Nb values than that of N-MORB but higher than that of E-MORB and OIB while Type 2 has higher Zr/Nb values than that of N-MORB, E-MORB and OIB (31.8 for N-MORB; 8.80 for E-MORB; 5.83 for OIB). In the Chondrite-normalized REE diagrams (Figure 40), Type 1 is characterized by relative enrichment in light REE (LREE) relative to heavy REE (HREE), while Type 2 has generally LREE-depleted to flat REE patterns ( $[\text{La/Yb}]_N = 1.04\text{-}1.77$  for Type 1 and  $[\text{La/Yb}]_N = 0.77\text{-}1.28$  for Type 2; N refers to all samples normalized with respect to Chondrite) (Figure 40). Most Type 2 samples have slight negative Eu anomalies while none of Type 1 samples shows this negative Eu anomaly. In two samples of Type 2, this signature appears to be quite strong (Figure 40).

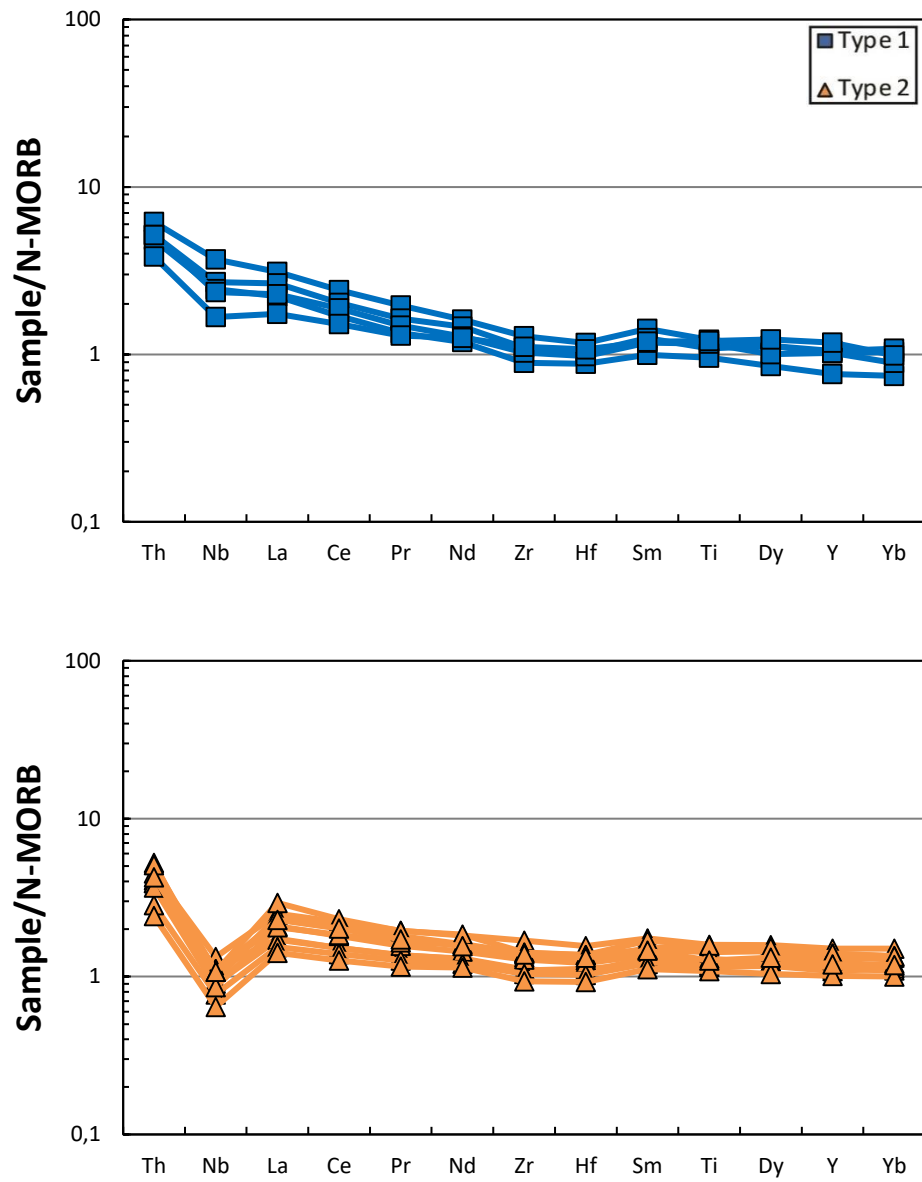


Figure 39. N-MORB normalized multi-element variation patterns of Type 1 and Type 2 samples (normalization data from Sun and McDonough, 1989).

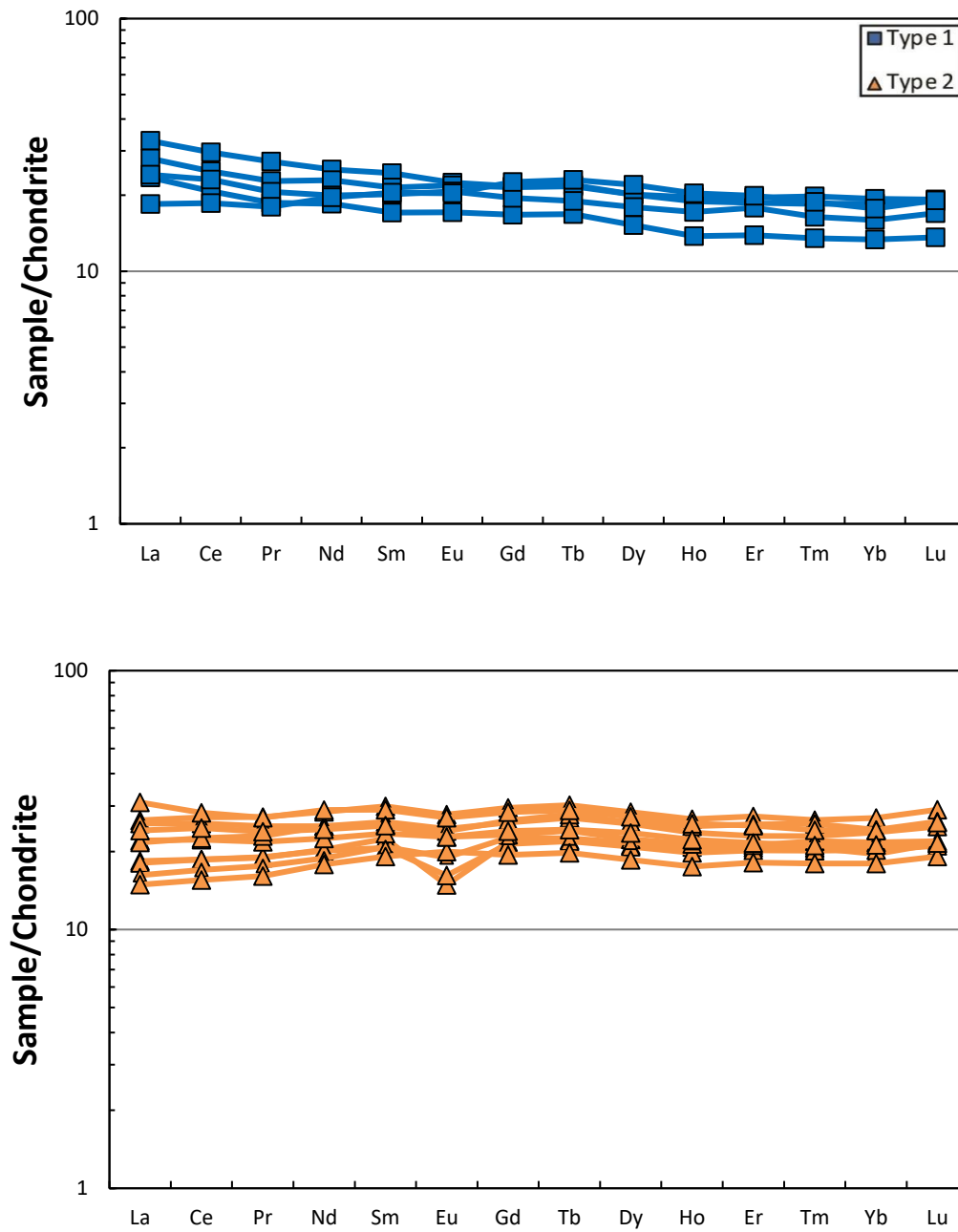


Figure 40. Chondrite normalized REE patterns of Type 1 and Type 2 samples (normalization data from Sun and McDonough, 1989).

## 4.5. Petrogenesis

### 4.5.1. Fractional Crystallization

Increasing content of  $\text{Fe}_2\text{O}_3$  with decreasing  $\text{MgO}$  is related with the ferro-magnesian mafic minerals such as olivine. This may suggest that Mg-rich olivines were thrown away from the system as the evolution of magma continues. That situation is not observed clearly in harker diagrams but when all samples considered, an increasing trend can be seen in  $\text{MgO}$  vs.  $\text{Fe}_2\text{O}_3$  diagram (Figure 37a). Other major oxide elements ( $\text{Al}_2\text{O}_3$ ,  $\text{CaO}$ ,  $\text{Na}_2\text{O}$ ,  $\text{P}_2\text{O}_5$  and  $\text{TiO}_2$ ) do not present enough trends to interpret the fractionation.

Variation diagrams of trace elements and  $\text{MgO}$  show similar trends as in major oxide diagrams (Figure 38). Ni and Co are highly compatible with olivine ( $K_d$  of Ni is 14 for olivine and 7 for clino-pyroxene; Rollison, 1993) so variation diagrams of both may show olivine and clinopyroxene fractionation. Theoretically, there must be a decreasing trend of Ni (ppm) or Co (ppm) content with decreasing  $\text{MgO}$  (wt.%) in those diagrams. In Figure 38a, this trend is seen nicely for Type 1 diabase rocks but it is not presented very well for Type 2 diabases. On the other hand, variation diagram of Co (ppm) represents better trend than that of Ni (ppm) for Type 2 while it has more scattered trend than that of Ni (ppm) for Type 1 (Figure 38b). Similarly, increasing content of V (ppm) with decreasing  $\text{MgO}$  (wt.%) content indicates that it is not observable of the fractionation of Fe-Ti oxides (Figure 38d). Decreasing content of Y (ppm) with decreasing content of  $\text{MgO}$  (wt.%) is related with garnet and amphibole minerals which Y (ppm) is mostly compatible with (Winter, 2001 after Green (1980)). In Y vs.  $\text{MgO}$  diagram (Figure 38e), an increasing trend of Y is seen, which again shows that fractionation of those minerals cannot be observable. Increasing content of Zr (ppm) by decreasing of  $\text{MgO}$  (wt.%) is not very clear for Type 2 while Type 1 rocks have much clearer trend, which again displays no fractionation of zircon or baddeleyite (Figure 38f). Sr (ppm) variation diagram does not present any significant data due to its highly mobility under hydrothermal alteration (Figure 38g). The relationship between Eu (ppm) and  $\text{MgO}$  (wt.%) shows that decreasing of  $\text{MgO}$  (wt.%) content causes an increasing of Eu (ppm), which indicates no plagioclase fractionation with a  $K_d$  of 1.5 (Winter, 2001 after Green (1980)) (Figure 38h). However, two samples (15-

BOG-12A and 15-BOG-12B) of Type 2 show decreasing trends which are also seen in chondrite-normalized REE diagram by means of negative Eu anomaly (Figure 38h). Eu anomaly can be either negative or positive whether plagioclase was removed that is the case for Type 2 diabase rocks (Figure 40) or accumulated, respectively (Gao and Wedepohl, 1995). As a result, some of the variation diagrams of major oxides and trace elements versus MgO (wt.%) gives fractional trends of ferro-magnesian and plagioclase phases during the magmatic evolution while others do not give any significant trend because of the possible effect of the hydrothermal alteration or unobservable of fractionation processes.

#### **4.5.2. Source Features**

In this section, several trace element ratios were used to understand the nature of the mantle source from which the studied diabases derived. These elemental ratios include Nb/Yb, Th/Yb, Zr/Nb, La/Nb, Th/Nb, Zr/Y and Nb/Y. In addition, published data from a number of geological environments were used for comparison. These geological settings are Greater Antilles island arc (Jolly et al., 1998), South Sandwich island arc (Pearce et al., 1995), Aolian continental arc (Calanchi et al., 2002), Andes continental arc (compilation of Winter (2001) after Thorpe et al. (1984)), Mariana back-arc (Pearce et al., 2005) and Mid-Atlantic Ridge (Niu et al., 2001).

Low Zr/Nb ratios may indicate derivation from an enriched mantle source like source of OIBs ( $Zr/Nb = 5.83$ ; Sun and McDonough, 1989) or E-MORBs ( $Zr/Nb = 8.80$ ; Sun and McDonough, 1989), whereas high Zr/Nb ratios may point out a depleted mantle source, such as N-MORB source ( $Zr/Nb = 31.8$ ; Sun and McDonough, 1989) (Figure 41). Type 1 rocks have a close Zr/Nb content with respect to E-MORB source ( $Zr/Nb = 11.1-21.0$ ) and they are scattered in the Mid-Atlantic Ridge field having an enriched mantle source like E-MORB except 16-BOG-1 which is also scattered in Mariana and Greater Antilles field (Figure 41). On the other hand, all of the Type 2 rocks have a much more close Zr/Nb content with respect to N-MORB ( $Zr/Nb = 31.5-52.0$ ) and they are confined in the Mariana back-arc field and additionally Greater Antilles and South Sandwich Island arcs (Figure 41). Hence, Type 1 diabases have more enriched mantle source than Type 2 diabases.

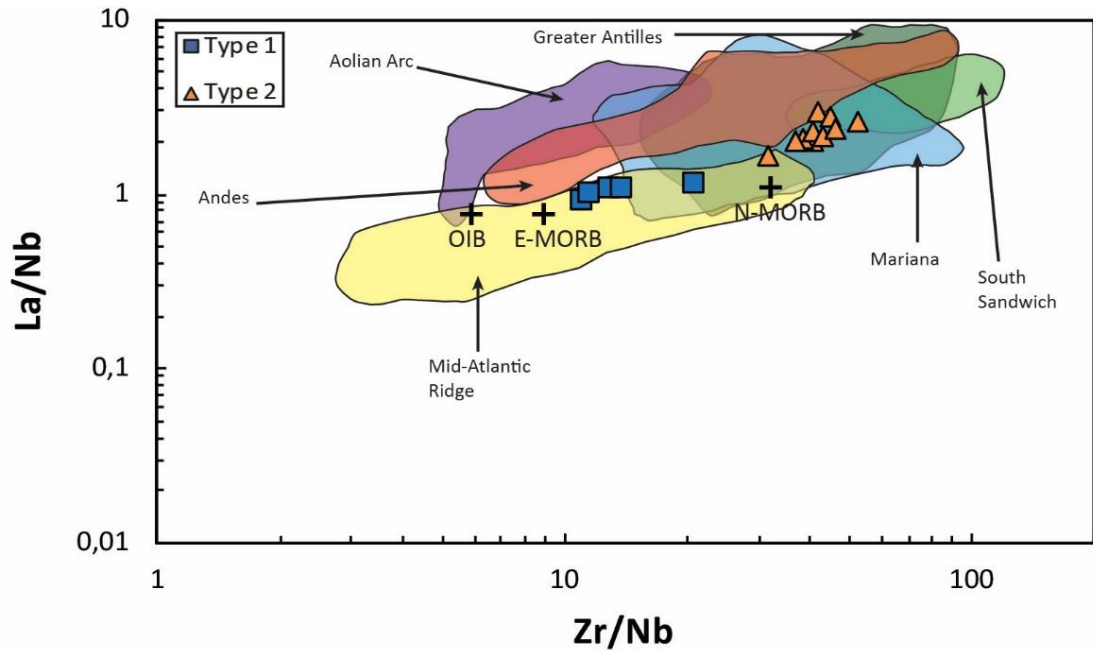


Figure 41. Zr/Nb-La/Nb diagram. Greater Antilles data from Jolly et al. (1998); South Sandwich data from Pearce et al. (1995); Aolian Arc data from Calanchi et al. (2002); Andes data from compilation of Winter (2001) after Thorpe et al. (1984); Mariana back-arc data from Pearce et al. (2005); Mid-Atlantic Ridge data from Niu et al. (2001) and OIB, E-MORB and N-MORB data from Sun and McDonough (1989).

Higher Zr/Y interpret more enriched mantle source like OIB-type source ( $Zr/Y = 9.66$  (Sun and McDonough, 1989)) or E-MORB-type source ( $Zr/Y = 3.32$  (Sun and McDonough, 1989)) and lower Zr/Y means more depleted mantle source like N-MORB source ( $Zr/Y = 2.64$  (Sun and McDonough, 1989)). Type 1 diabases ( $Zr/Y = 2.49-3.35$ ) have again a more enriched source according to this diagram since Zr/Y content of them is much closer to E-MORB-type source (Figure 42). Type 1 diabases are shown here into Mid-Atlantic Ridge field having again an enriched mantle source like E-MORB but they also are scattered in the Aolian continental arc field in this diagram. On the other hand, Type 2 diabases have much more closer meaning lower Zr/Y content ( $Zr/Y = 2.40-3.05$ ) to a N-MORB-type depleted mantle source than Type 1. They are confined in the Mid-Atlantic Ridge and additionally Greater Antilles and South Sandwich Island arcs fields like in Figure 41 (Figure 42). Higher Zr/Nb content

of Type 2 indicates more depleted source than that of Type 1, which can also be seen in Figure 42 similar to Figure 41.

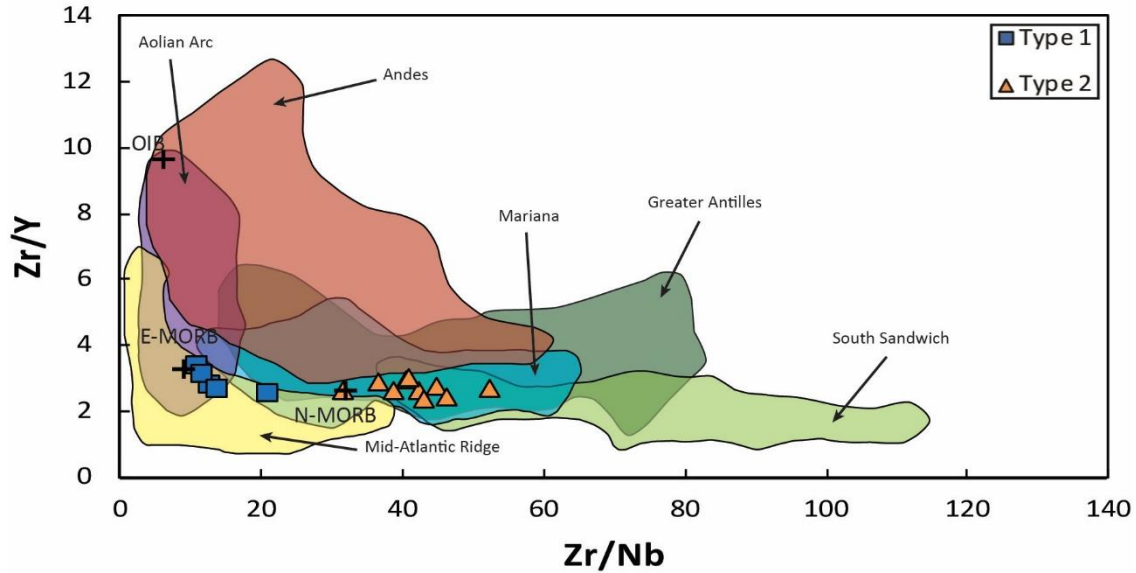


Figure 42. Zr/Nb-Zr/Y diagram. All data sources can be seen in Figure 41.

Higher Nb/Y points out more enriched mantle source like OIB-type source ( $Nb/Y = 1.66$  (Sun and McDonough, 1989)) or E-MORB-type source ( $Nb/Y = 0.38$  (Sun and McDonough, 1989)) while lower Nb/Y indicates more depleted mantle source like N-MORB Type source ( $Zr/Y = 0.08$  (Sun and McDonough, 1989)) (Figure 43). This diagram is also proves having more enriched mantle source of Type 1 diabases resulted from higher Nb/Y ratio ( $Nb/Y = 0.12-0.30$ ) and they are again scattered in the Mid-Atlantic Ridge field having again an enriched mantle source like E-MORB (Figure 43). Similarly, Type 2 diabases have lower Nb/Y contents ( $Nb/Y = 0.05-0.08$ ) indicating more depleted mantle source. They are confined in the Mariana back arc, Greater Antilles island arc and South Sandwich island arc fields similar to previous diagrams (Figure 43). Similarly, higher Nb/Y content (Figure 42) can be correlated with higher Zr/Y (Figure 43) content in order to point out more enriched sources like

that Type 1 have higher Nb/Y and Zr/Y content than Type 2, which shows more enriched source of Type 1.

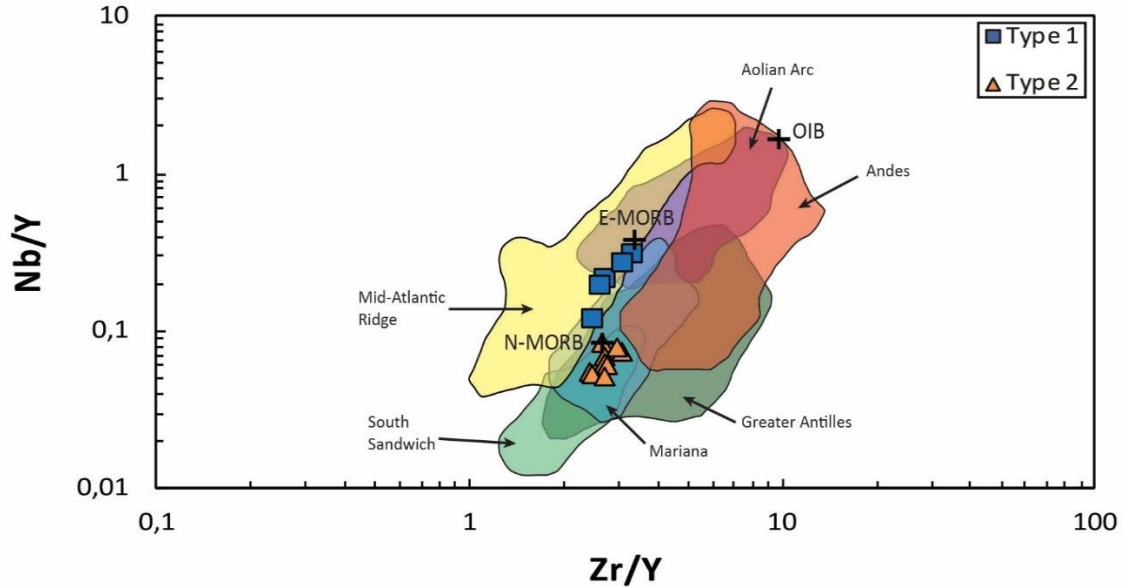


Figure 43. Zr/Y-Nb/Y diagram. All data sources can be seen in Figure 41.

Nb/Yb-Th/Yb diagram again displays a crucial story about diabbases because of the relationship of Th and Nb elements and subduction mechanism. According to diagram, if Th/Yb ratios are higher and higher, subduction components in the source will be higher. Th/Yb ratio of Type 1 is 0.15-0.26 and that of Type 2 is 0.09-0.15. The diagram indicates that continental arcs have the highest ratios in Th/Yb ( $\text{Th/Yb} > 0.70$  (accepting  $\text{Nb/Yb} = 1$ )) (Figure 44). Island arcs ( $0.07 < \text{Th/Yb} < 0.70$  (accepting  $\text{Nb/Yb} = 1$ )) are following continental arcs in this relation and Mid-ocean ridges have the lowest Th/Yb ratio ( $0.03 < \text{Th/Yb} < 0.07$  (accepting  $\text{Nb/Yb} = 1$ )). Back-arc basins show mixture between Mid-Ocean Ridges and arc regions ( $0.02 < \text{Th/Yb} < 0.9$  (accepting  $\text{Nb/Yb} = 1$ )). Nb is also a signature of subduction component so that Nb content lower in arc-related rocks than mid-ocean ridge originated rocks, which can be observed in all these ratio diagrams. Also, negative Nb anomaly in multi-element diagrams (Figure 39) indicates subduction zone activity where mobile elements (eg.

LILE) may be transferred into the mantle from subducted oceanic slab and its melts while some immobile elements (eg. HFSE) may be covered into the subducted slab (eg. Pearce, 1982). Moreover, higher Nb/Yb ratios imply an enriched source like OIB-type source ( $\text{Nb/Yb} = 22.2$  (Sun and McDonough (1989)) or E-MORB-type source ( $\text{Nb/Yb} = 3.50$  (Sun and McDonough (1989)) and lower Nb/Yb ratios mean a more depleted source like N-MORB-type source ( $\text{Nb/Yb} = 0.76$  (Sun and McDonough (1989)). Type 1 diabases have a more enriched mantle source resulted from having higher Nb/Yb content ( $\text{Nb/Yb} = 1.30\text{-}2.73$ ). They are scattered in the Mid-Atlantic ridge field having an enriched mantle source like E-MORB and also Mariana back-arc field (and Greater Antilles field for 16-BOG-1) for this diagram (Figure 44). In contrast, Type 2 diabases have a more depleted mantle source resulted from having lower Nb/Yb content ( $\text{Nb/Yb} = 0.49\text{-}0.78$ ) and they are confined in Mariana back-arc and Greater Antilles island arc (Figure 44).

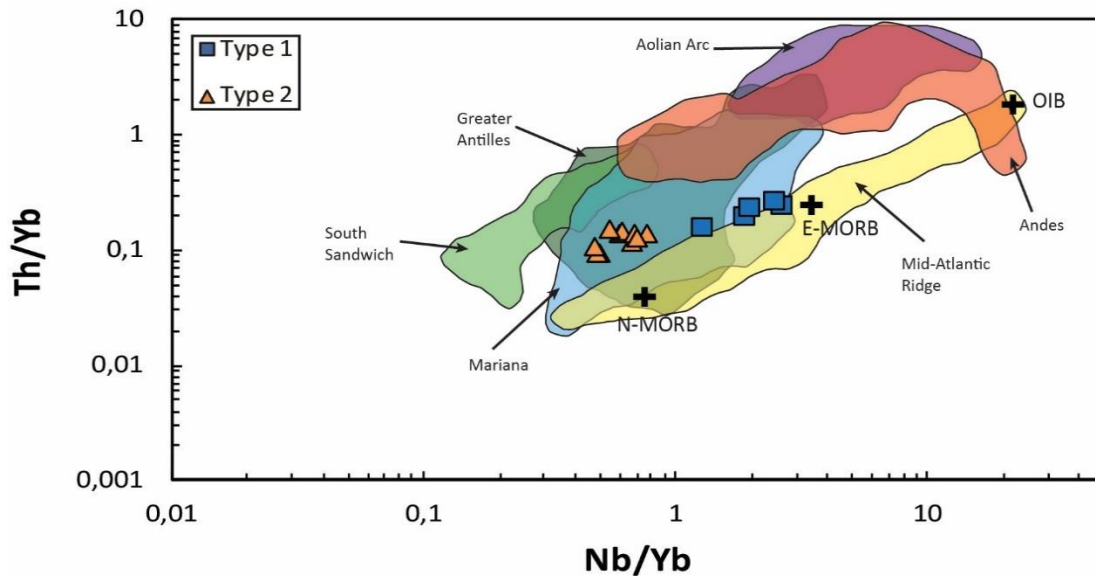


Figure 44. Nb/Yb-Th/Yb diagram. All data sources can be seen in Figure 41.

Zr/Nb versus Th/Nb diagram again shows a similar story with Figure 44 since Th/Nb is a trace for subduction activities. Th/Nb content of Type 1 is 0.09-0.12 and that of

Type 2 is 0.17-0.29 (Figure 45). Continental arcs have higher Th/Nb contents ( $0.2 < \text{Th/Nb} < 2$  (accepting  $\text{Zr/Nb} = 30$ )) (Figure 45). Island arcs are following continental arcs in this comparison ( $0.2 < \text{Th/Nb} < 1$  (accepting  $\text{Zr/Nb} = 30$ )). Lastly, mid-ocean ridges have the lowest Th/Nb ratios ( $0.04 < \text{Th/Nb} < 0.1$  (accepting  $\text{Zr/Nb} = 30$ )). Again, back-arc basins have the mixture of Th/Nb ratios between arc regions and mid-oceanic ridges ( $0.04 < \text{Th/Nb} < 1$  (accepting  $\text{Zr/Nb} = 30$ )). Thus, Type 1 diabases are generally scattered in Mid-Atlantic Ridge field with a lower subduction affected and again an enriched mantle source like E-MORB and Type 2 diabases are scattered in Mariana back-arc basin and Greater Antilles fields with higher subduction affected source (Figure 45).

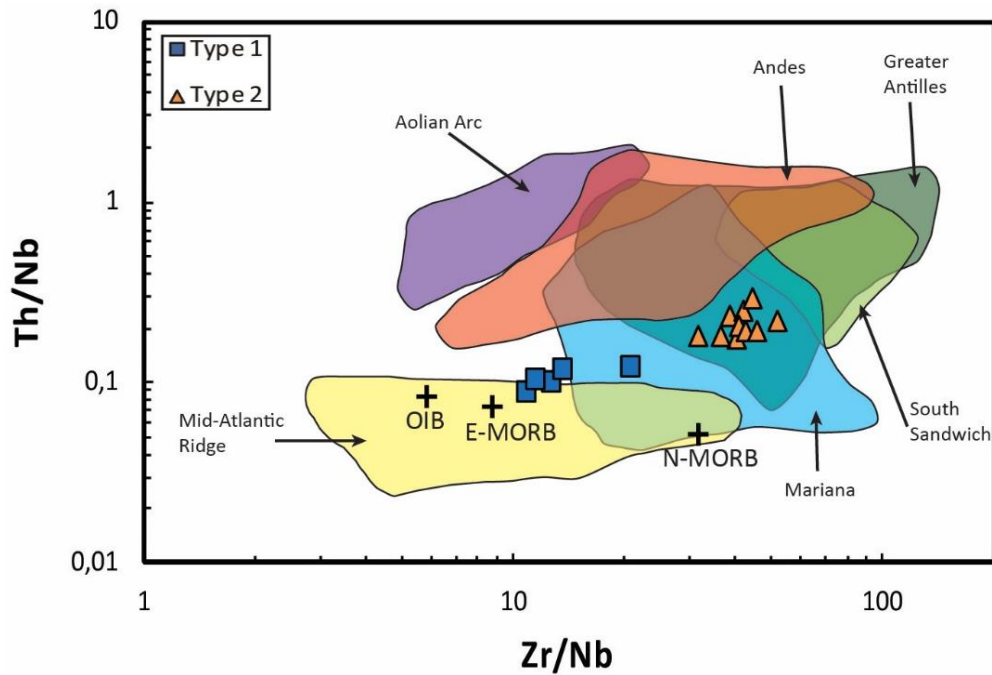


Figure 45. Zr/Nb-Th/Nb diagram. All data source can be seen in Figure 41.

#### 4.5.3. Partial Melting

Another question can be asked about whether these diabases were originated from a spinel or garnet-bearing mantle source. In order to answer this question, the model by

Sayit et al. (2016) including Sm/Yb versus Dy/Yb diagram is used (Figure 46). The reason for using these elements on this diagram is that HREEs are compatible with garnet (Winter, 2001) and not compatible with spinel (Shimizu, 1975; Blundy et al., 1998; Nagasawa et al., 1980). In this model, samples having MgO (wt.%) content more than 5 are chosen in order to lower the effect of fractional crystallization. The model suggests that both Type 1 and Type 2 have been formed in the stability of spinel (Figure 46). Type 1 diabases have generally smaller degree of partial melting than Type 2 diabases (Figure 46).

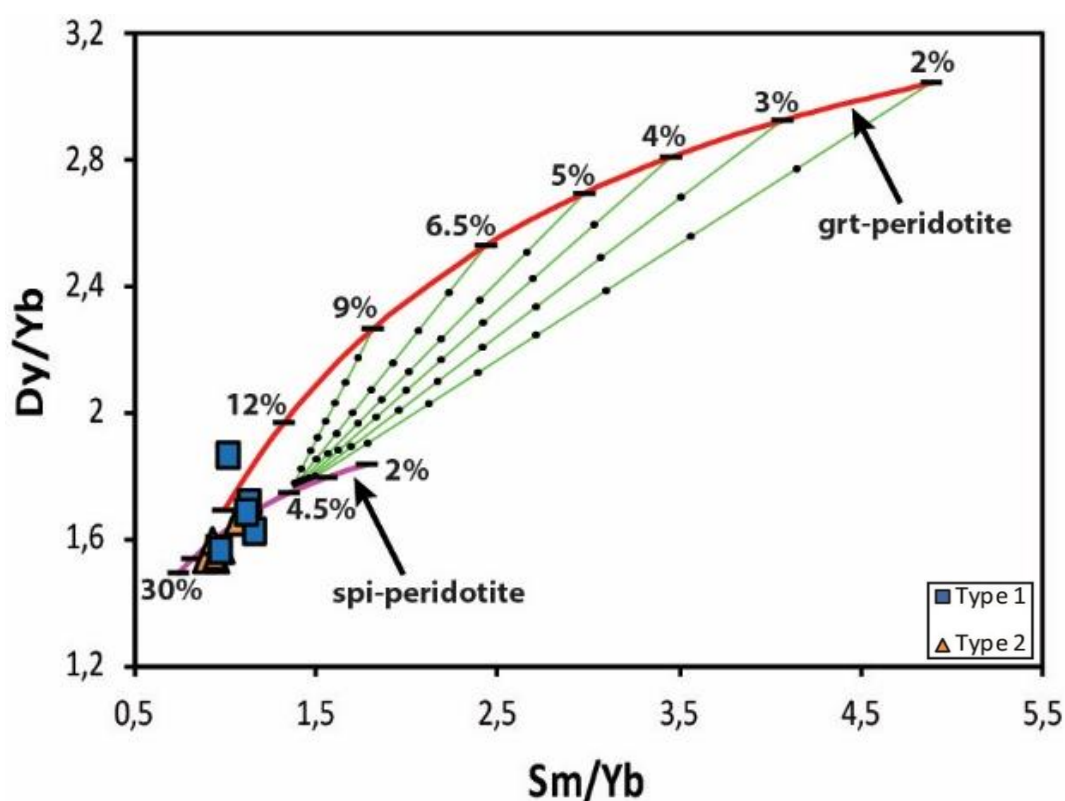


Figure 46. Geochemical modelling of the diabase rocks having MgO (wt.%) content more than 5.00. E-DMM and DMM compositions of Workmann and Hart (2005) have been adopted for the garnet and spinel peridotite sources, respectively. Garnet peridotite source is assumed to have the mode of 0.600 Ol + 0.210 Opx + 0.120 Cpx + 0.070 Grt, which melts in the proportions 0.010 Ol + 0.040 Opx + 0.500 cpx + 0.450 Grt. Spinel peridotite source has the mode of 0.565 Ol + 0.220 Opx + 0.180 Cpx + 0.035 Spi and melts in the proportions of 0.200 Ol + 0.150 Opx + 0.550 Cpx + 0.100 Spi. Both melting curves have been modelled according to batch melting. Straight lines represent melt-mixing lines between various degrees of Grt-facies melts (2–9%) and 4.5% Spi-facies melt. Melt fractions contributed by these facies were indicated by dots drawn at each 10% interval (Sayit et al, 2016).

#### 4.6. Tectonic Discrimination of the Studied Samples

Every tectonic environment has its own geochemical characteristics (Wood et al., 1979), thus it can be useful to use tectonic discrimination diagrams to understand the tectonic environment of the studied diabases.

In Ti/Y-Zr/Y diagram (Pearce and Gale, 1977) (Figure 47), both of diabase types are scattered in the plate-margin basalt field which includes arc-back arc type basalts and MORB Types in the active plate margins. On the other hand, Ti/1000-V diagram (Shervais, 1982) is confined in the BAB (back-arc basalts) - MORB fields (Figure 48). According to this diagram, there is no sample which is scattered in the IAT (island arc tholeiites) field (Figure 48). Moreover, the trivariate Hf-Th-Nb (Wood, 1980) tectonic diagram shows an E-MORB environment of Type 1 and an arc-basalt environment of Type 2 diabases (Figure 49). To sum up, both Type 1 and Type 2 diabases were formed in a plate-margin environment. Specifically, this plate margin environment of both Type 1 and Type 2 was subdivided into back-arc basin or mid-ocean ridge environments by means of Ti/1000 vs. V diagram. However, Figure 49 make this subdivision much more specific where Type 1 had been formed in a mid-ocean ridge environment while Type 2 had been formed in an arc environment that is actually a back-arc basin environment by means of correlating it with Figure 48.

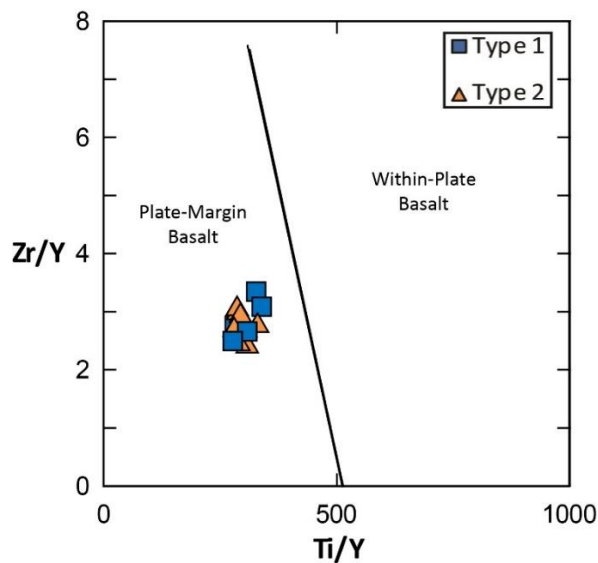


Figure 47. Ti/Y-Zr/Y tectonic discrimination diagram (Pearce and Gale, 1977).

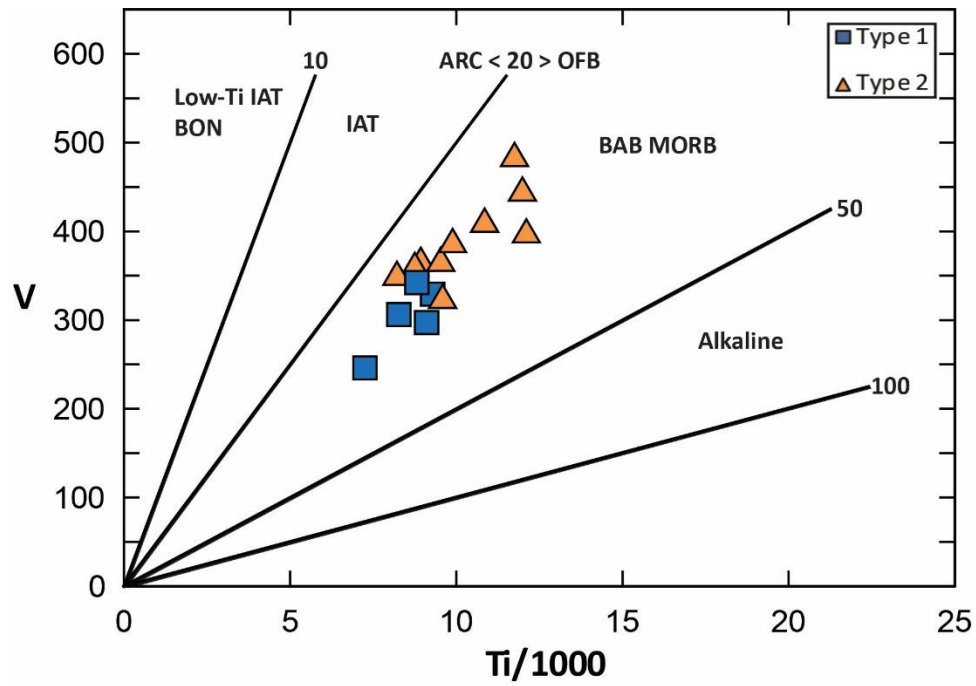


Figure 48. Ti/1000-V tectonic discrimination diagram (Shervais, 1982).

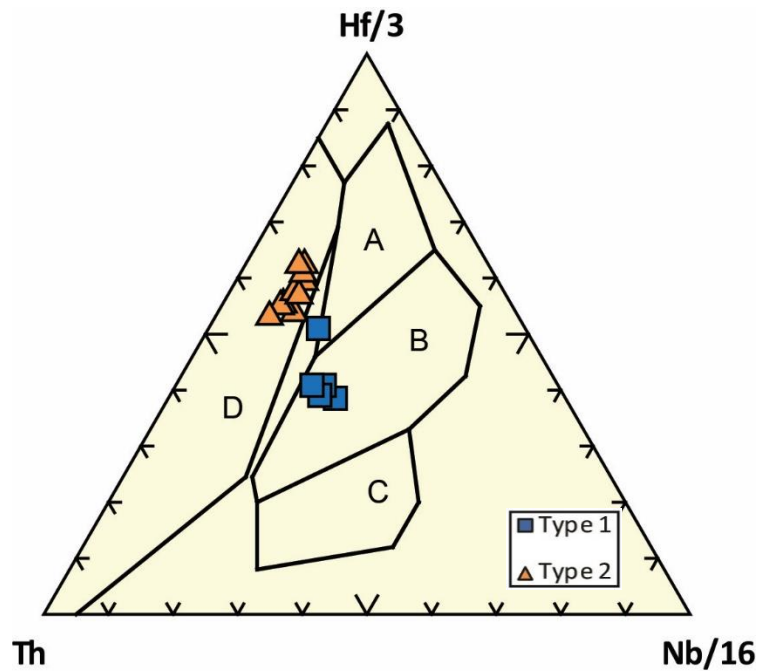


Figure 49. Hf/3-Th-Nb/16 tectonic discrimination diagram. A = N-MORB, B = E-MORB, C = OIB (Rift) and D = Arc-basalts (Wood, 1980)

In addition to these tectonic discrimination diagrams, N-MORB normalized multi-element diagrams including Type 1 and Type 2 diabases and Greater Antilles island, South Sandwich island arc, Aolian continental arc, Andes continental arc, Mariana back-arc, Mid-Atlantic Ridge and OIB and E-MORB data (data source references was given in previous parts; see Figure 41) for comparison are used. To do this comparison, the most primitive sample (highest MgO content) having all or most of the trace elements is selected from the datasets.

Comparison of OIB data with Type 1 and Type 2 points out that OIB data has too much enrichment in almost all elements except Dy, Y and Yb for both types (Figure 50). Therefore, OIB originated environments are not the case for both types.

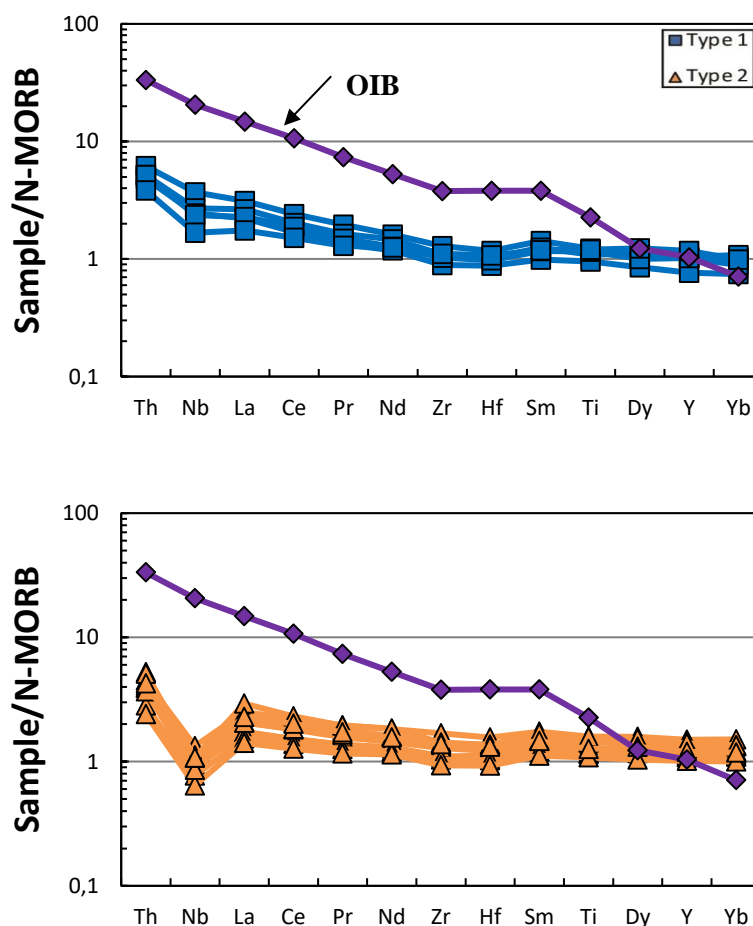


Figure 50. N-MORB normalized multi-element pattern of Type 1 and Type 2 diabases with the comparison of OIB data from Sun and McDonough, (1989).

Comparison of N-MORB normalized multi-element pattern of island arc tectonic environments containing Greater Antilles and South Sandwich with both types indicates that they do not have a match with the island arc environment (Figure 51 and 52). Island arc data shows negative Nb anomaly relative to Th and La like Type 2 diabases but they have greater anomaly than Type 2 (Figure 51 and 52). Furthermore, Greater Antilles island arc is depleted in the less mobile elements (eg. Zr, Hf, Ti, Dy, Y and Yb), which is not seen in both types (Figure 51). Also, South Sandwich island arc is depleted in all elements except Th, which is not the case for both types (Figure 52).

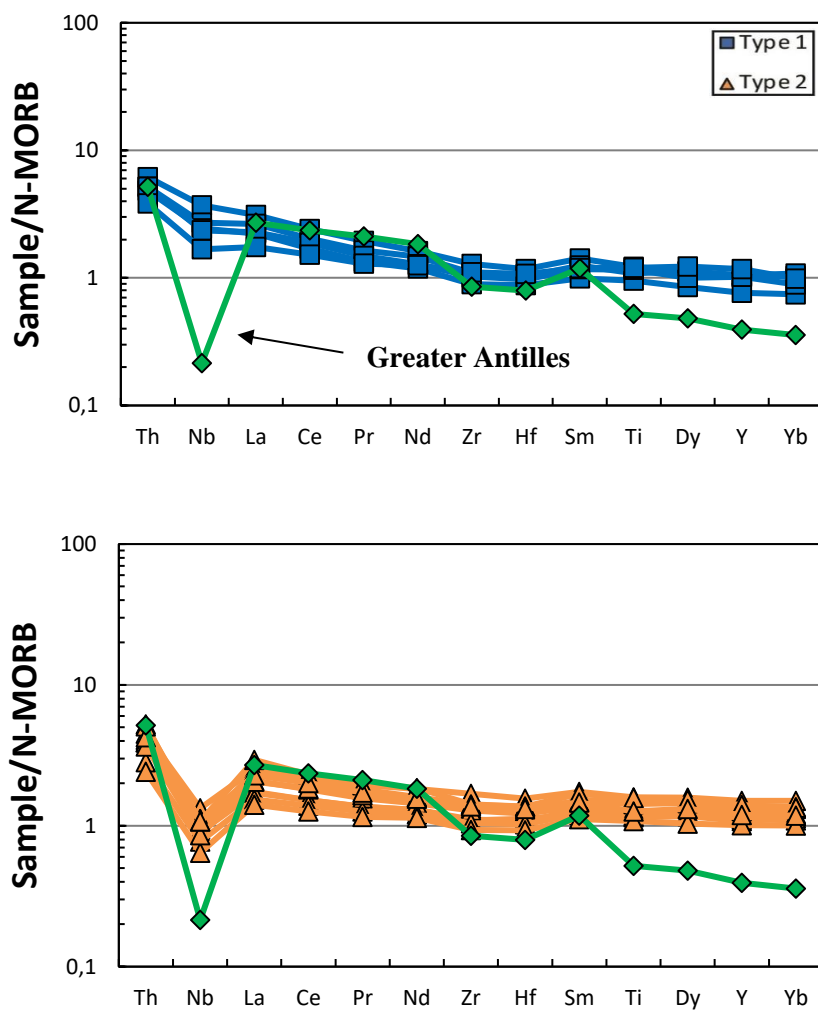


Figure 51. N-MORB normalized multi-element pattern of Type 1 and Type 2 with the comparison of Greater Antilles data (Sample No: FJ-25; MgO (wt.%) = 6.75 from Jolly et al. (1998))

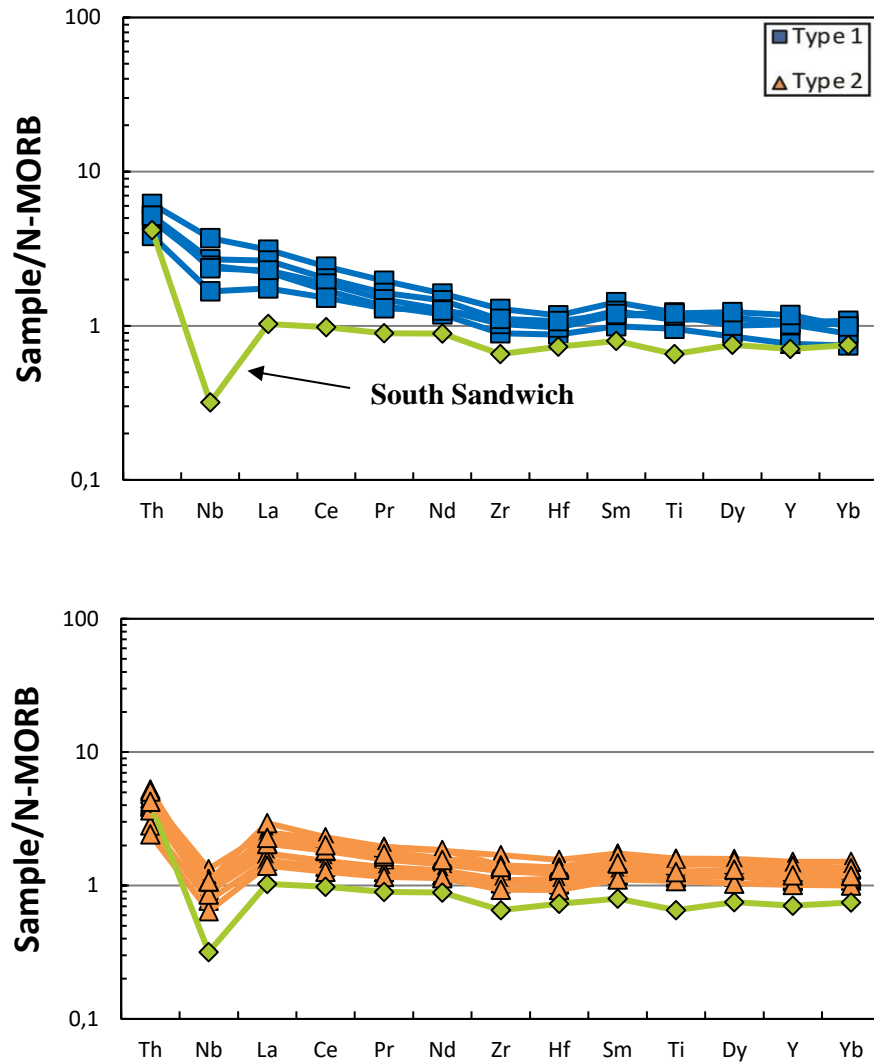


Figure 52. N-MORB normalized multi-element pattern of Type 1 and Type 2 with the comparison of South Sandwich data (Sample No: SSS (10-1); MgO (wt.%) = 7.45 from Pearce et al. (1995)).

Neither of Type 1 nor Type 2 diorites shows similarities with the continental arc data (Figure 53 and 54). Both Aolian continental arc and Andes continental arcs show several negative and positive anomalies. The trace elements Pr and Dy cannot be used for this diagram because they are not available in neither Aolian arc nor Andes datasets. Firstly, they have more enriched Th content than both types, which is a good signature of a continental lithosphere (Figure 53 and 54). Secondly, Aolian arc is

enriched more in the more mobile elements (eg. Th, La, Ce and Nd) except Nb whose content is almost similar with the Type 1 diabases and Andes continental arc is enriched more in the less immobile elements (Th, Nb, La, Ce and Nd) and also in the more immobile elements (eg. Zr, Hf and Sm) than both diabase Types (Figure 53 and 54). On the other hand, in the more immobile elements (Zr, Hf, Ti, Y and Yb) except Sm, Aolian arc is more depleted than both diabase Types (Figure 53 and 54) and Andes continental arc is more depleted than Type 1 diabases in Yb content and is more depleted than Type 2 diabases in Ti, Y and Yb contents (Figure 53 and 54).

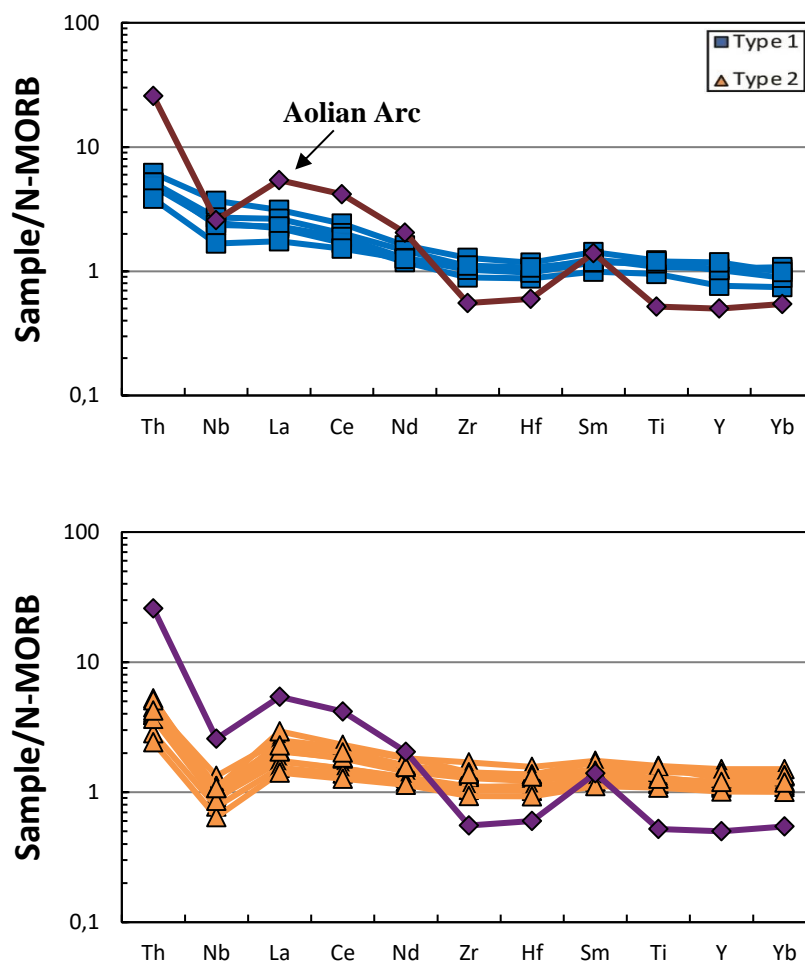


Figure 53. N-MORB normalized multi-element pattern of Type 1 and Type 2 with the comparison of Aolian Arc data ( $\text{MgO (wt.\%)} = 6.37$ ) from Calanchi et al. (2002)).

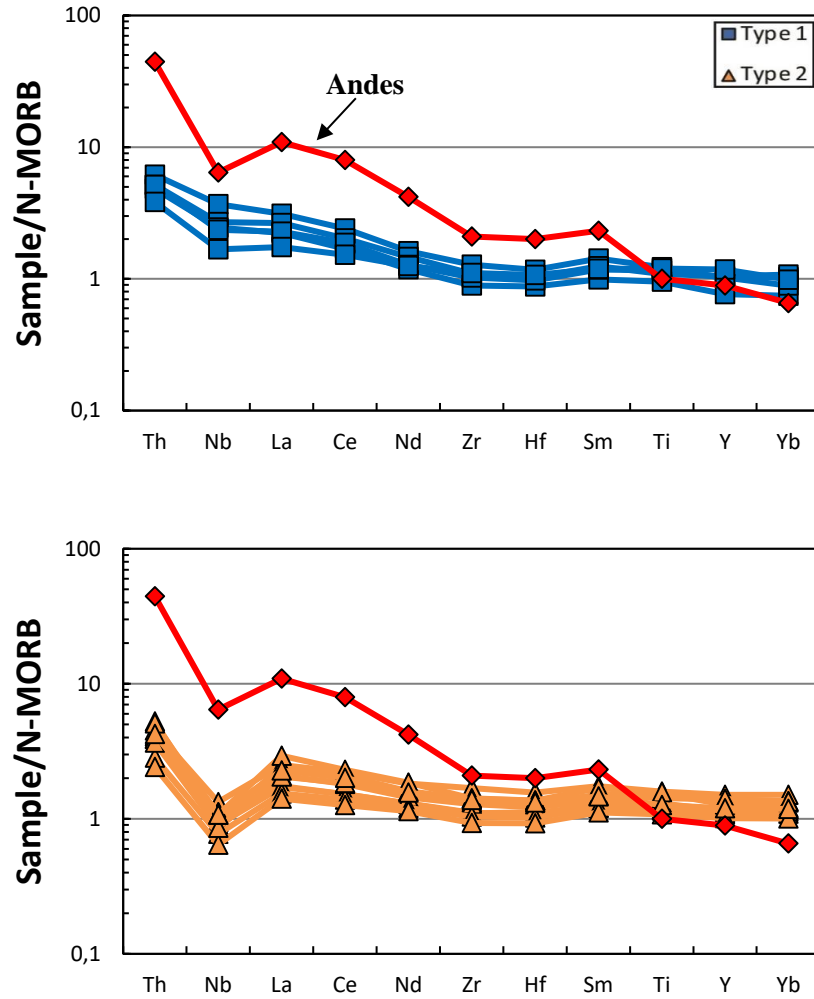


Figure 54. N-MORB normalized multi-element pattern of Type 1 and Type 2 with the comparison of Andes data (Sample No: CVZ-Cal-LO34; MgO (wt.%) = 7.76) from compilation of Winter (2001) after Thorpe et al. (1984)).

E-MORB data show similarities with just Type 1 diabases (Figure 55). General decreasing trend from Th to Yb can be seen in both E-MORB and Type 1 data. Type 1 except one sample only do not have depletion in Ti, Dy, Y and Yb elements which E-MORB has been depleted in. E-MORB is not similar to Type 2 since Type 2 has much more parallel trend from Th to Yb than E-MORB. Also, negative Nb anomaly of Type 2 is not present in E-MORB. Thus, E-MORB data is the best environment for Type 1 so far.

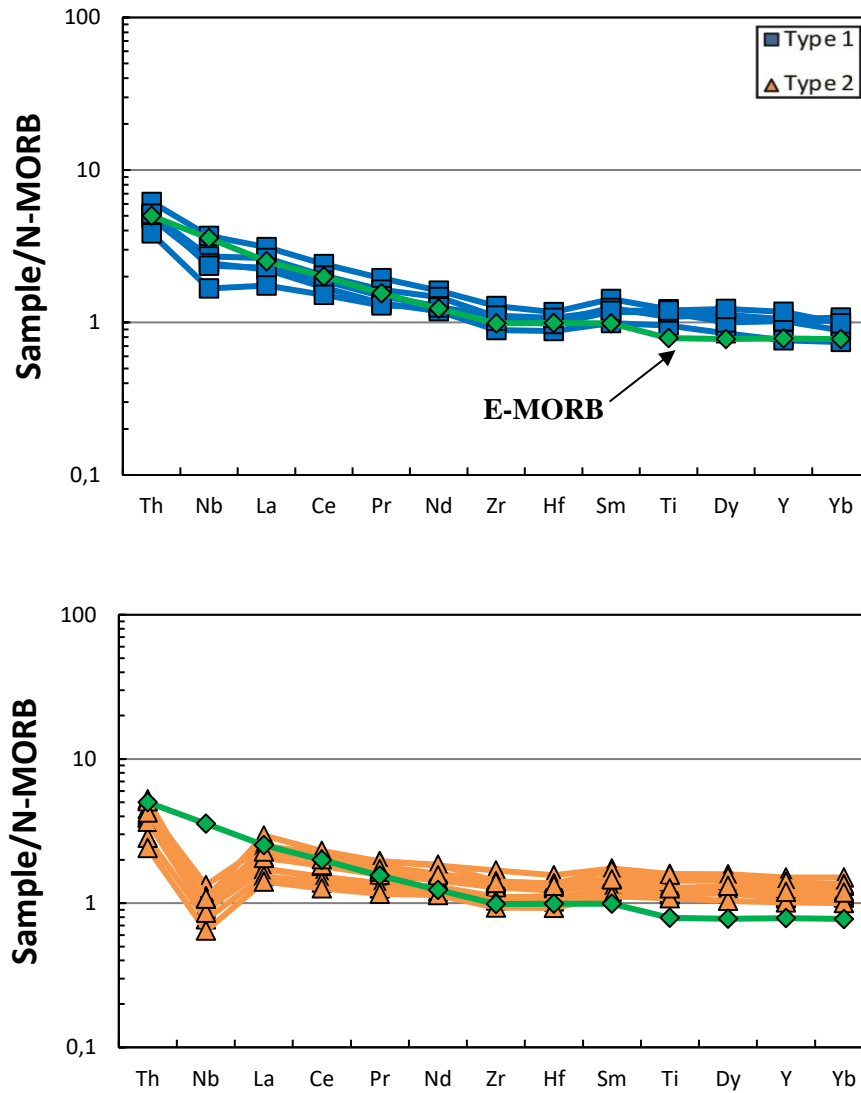


Figure 55. N-MORB normalized multi-element pattern of Type 1 and Type 2 diabases with the comparison of E-MORB data (Sun and McDonough, 1989).

Comparison of Mariana back-arc data with both Type 1 and Type 2 diabases indicates that all Type 2 have a similar pattern with it (Figure 56). Negative Nb depletion of Type 2 and Mariana back-arc data are very similar to each other and positive Sm anomaly is the case for both data. On the other hand, Type 1 has also a similar pattern with Mariana back-arc except from negative Nb anomaly. Moreover, positive Sm anomaly is also present in Type 1 (Figure 56). Hence, Mariana back-arc environment is a perfect match for Type 2 but a possible match for Type 1.

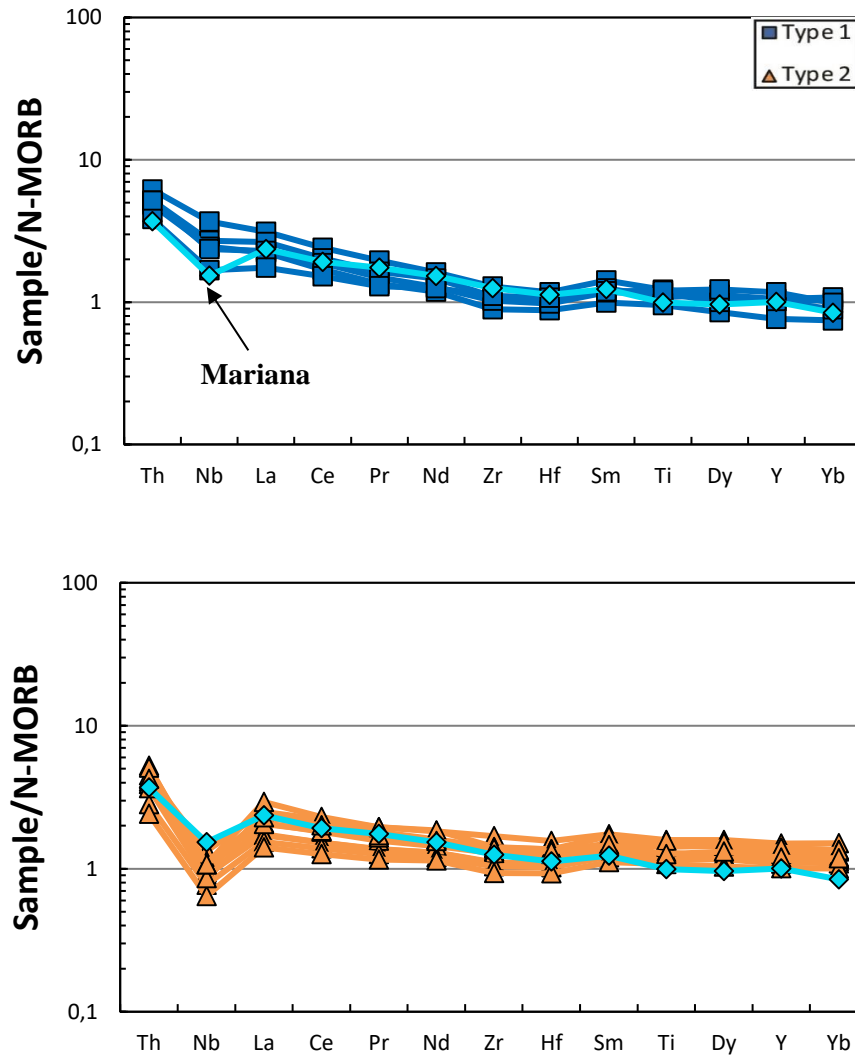


Figure 56. N-MORB normalized multi-element pattern of Type 1 and Type 2 with the comparison of Mariana back-arc data (Sample No: D1010; MgO (wt.%) = 7.57) from Pearce et al. (2005)).

To conclude, whole-rock geochemistry of these diabases according to immobile trace elements systematics supports the idea of the two Type of them determined by petrographical works. Clinopyroxene-bearing Type 1 have an enriched mantle source while amphibole-bearing Type 1 diabases have a depleted mantle source. Since negative Nb anomalies of Type 2 diabases in the N-MORB normalized multi-element patterns, which points out the subduction zones and having generally similar source

with the Mariana back-arc basin, they are having a BABB (back-arc basin basalt) character. On the other hand, Type 1 diabases have a similar enriched mantle source with the E-MORB (Sun and McDonough, 1989) in all of the ratio diagrams. They also have similar pattern with it in both multi-element patterns where they are enriched in incompatible elements. Therefore, Type 1 diabases have an E-MORB Type geochemical character. Tectonic discrimination diagrams are showing that these dykes are formed in an extensional region. This extensional region for Type 1 dykes may be a typical mid-ocean ridges or back-arc basin while that for Type 2 dykes may be behind a subduction zone probably as a back-arc basin.

#### **4.7. Geochronology of the Diabase Dykes**

Two Type 2 diabase rocks (HT-16 and HT-20-A) were analyzed for  $^{40}\text{Ar}/^{39}\text{Ar}$  age dating. Single hornblende crystals have been used to get the age by means of incremental heating method. Both analyzed gave cooling plateau age of the rocks. Both samples have some Ar-loss at their edges which can be understood from inverse isochron plots (Figure 57b and 58b).

Plateau age of HT-16 is  $176.30 \pm 0.52$  Ma (Toarcian) (Figure 57a). Statistically, this age has been confirmed by 95% confidence level limit ( $2\sigma$ ) including 0.29% standard deviation ( $1\sigma$ ) in the J-value. Toarcian age is the primary cooling age of the diabase dykes. Plateau age was calculated from the area between 2% and 94% cumulative  $^{39}\text{Ar}$  (k) released (Figure 57a). Besides, incremental heating of hornblende points out that there were some secondary processes (e.g. hydrothermal alteration) before this time which can be seen for the area before 2% cumulative  $^{39}\text{Ar}$  (k) released (Figure 57). These secondary Ar-loss is related with the edge of the crystals since alteration of a crystal starts from the edges to center. Therefore, the age found here from the center of primary hornblendes gives the cooling age of the crystal and so the dyke.

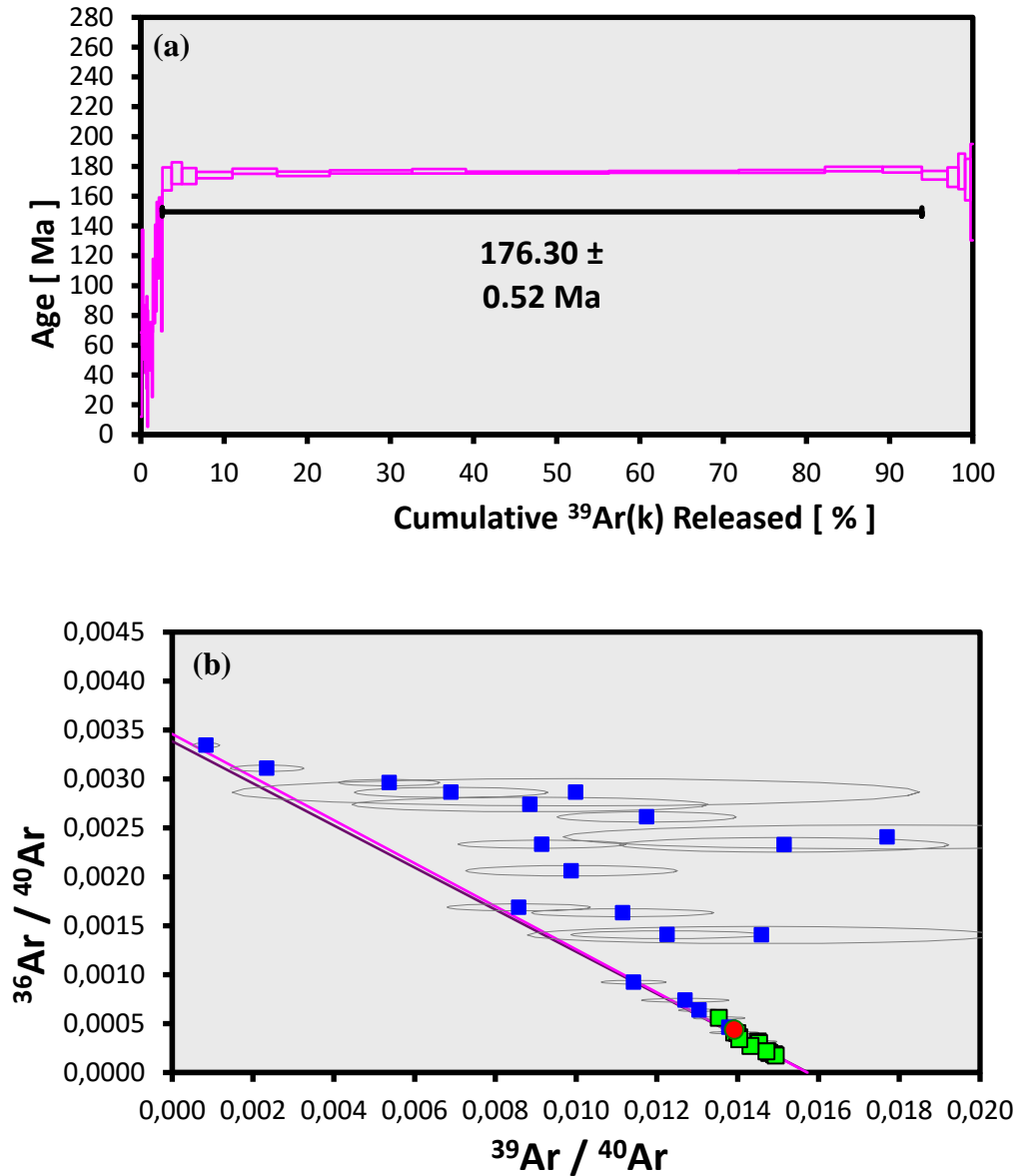


Figure 57. a) Incremental heating  $^{40}\text{Ar}/^{39}\text{Ar}$  age spectra for HT-16 diabase rock showing  $176.30 \pm 0.52$  Ma age. The  $^{40}\text{Ar}/^{39}\text{Ar}$  age has 95% confidence level limit ( $2\sigma$ ) including 0.29% standard deviation ( $1\sigma$ ) in the J-value. b) Inverse isochron plots for incremental heating  $^{40}\text{Ar}/^{39}\text{Ar}$  age spectra for HT-16 diabase rock indicating Ar-loss for the edge of the crystal. Note that reference line (purple line) is shown in conjunction with the calculated isochron (pink line). Green squares indicate steps included in the age calculations. Blue circles indicate steps which are not included in the age calculations. The locations of the total fusion (TF) points are shown by red circle which is not included in the calculations.

Plateau age of HT-20-A gives very close age compared to HT-16. The cooling age of HT-20-A is  $178.82 \pm 0.80$  Ma (Toarcian) (Figure 58a). Statistically, this age also confirmed by 95% confidence level limit ( $2\sigma$ ) including 0.44% standard deviation ( $1\sigma$ ) in the J-value. Plateau age which gives cooling age of the hornblende crystal was calculated from the area between 38% and 98%  $^{39}\text{Ar}$  (k) released (Figure 58a). The area before 38%  $^{39}\text{Ar}$  (k) released contains secondary process traces similar to HT-16.

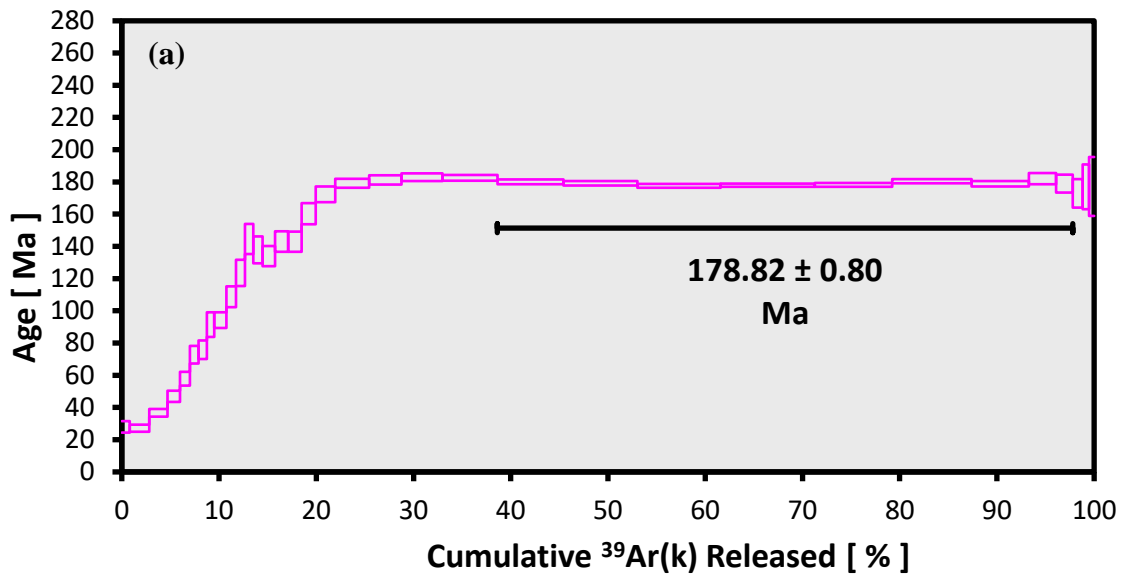


Figure 58. a) Incremental heating  $^{40}\text{Ar}/^{39}\text{Ar}$  age spectra for HT-20-A diabase rock showing  $178.82 \pm 0.80$  Ma age. The  $^{40}\text{Ar}/^{39}\text{Ar}$  age has 95% confidence level limit ( $2\sigma$ ) including 0.44% standard deviation ( $1\sigma$ ) in the J-value. b) Inverse isochron plots for incremental heating  $^{40}\text{Ar}/^{39}\text{Ar}$  age spectra for HT-20-A diabase rock indicating again Ar-loss for the edge of the crystal. Note that reference line (purple line) is shown in conjunction with the calculated isochron (pink line). Green squares indicate steps included in the age calculations. Blue circles indicate steps which are not included in the age calculations. The locations of the total fusion (TF) points are shown by red circle which is not included in the calculations.

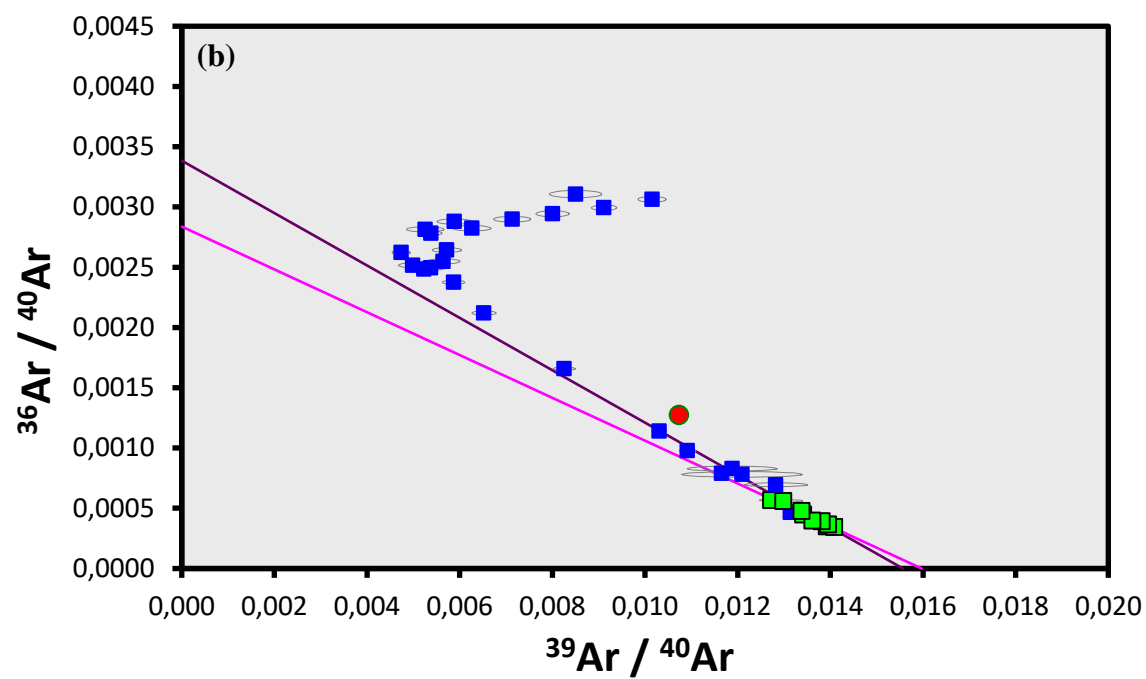


Figure 58. Cont'd.



## **CHAPTER 5**

### **DISCUSSION**

In this chapter, diabase dykes within the Hattuş Ophiolitic Mélange which is the remnant of Izmir-Ankara-Erzincan Ocean will be summarized and discussed according to petrographic, geochemical and geochronological data in order to enlighten the geodynamic evolution of them. Moreover, the geochemical and geochronological findings from these dykes will be compared and correlated with diabase dykes from the western and eastern Turkey as well as diabase dykes around the world.

Field observations point out that studied diabase dykes around Boğazkale region cross-cut peridotite, gabbros and pillow basalts which are the remnants of IAE Ocean. All of the Type 2 diabase dykes cross-cut just the ultramafic peridotite rocks and they are found in the south and southeast of Boğazkale. On the other hand, Type 1 diabase dykes cross-cut ultramafics, gabbros and pillow basalts and they are found in the east of Boğazkale and west of Küçükırka Village. Both Type 1 and Type 2 diabases resemble each other in the field. Both have darker green colors and very fractured appearances. Furthermore, faulting of diabase dykes indicate that the region had been affected by tectonism after the intrusion of dykes.

Total of 48 samples of diabases and their host rocks from Boğazkale region were examined under the polarizing microscope. All of the samples were discussed according to their granularity, crystallinity and fabric properties. Petrographical grouping could not be used for this thesis because some samples could not save their

primary minerals due to hydrothermal alteration. However, the petrographic studies of samples that include their primary minerals saved show that there are two types of diabases which are clinopyroxene and plagioclase dominated Type 1 diabases and hornblende and plagioclase dominated Type 2 diabases. Some of Type 1 diabases have local porphyritic textures containing bigger plagioclase crystals among the other minerals while others have equigranular fabric. Similarly, some of Type 2 diabases show local porphyritic texture with a bigger hornblende and/or plagioclase crystal while others have equigranular fabric. All of the diabases have holocrystalline crystallinity and granularity of them is phaneritic. Ophitic to subophitic textures are present in some Type 1 diabases while poikilitic textures are observed in some Type 2 diabases. Some primary hornblendes in Type 2 diabases indicate simple twinning. Plagioclases in both Types have polysynthetic twinning and skeletal and embayed texture in some samples.

All of the diabases were affected by hydrothermal alteration. The effect of this alteration can be seen with secondary minerals. These secondary minerals are chlorite, epidote and prehnite for Type 1 and chlorite, actinolite, prehnite and biotite for Type 2. LOI values of the samples varies in a wide range, which also suggest that almost all of the samples were affected from secondary processes such as hydrothermal alteration. Alteration is very intense for almost all samples. However, there are also Type 2 samples whose alteration is not that much intense so that primary hornblendes are present. The intensity of alteration for those samples is so reasonable that primary hornblendes had been used for Ar-Ar geochronology.

Pillow basalts, gabbros and ultramafics are the host rocks intruded by these diabase dykes. Pillow basalts cross-cut by clinopyroxene-bearing diabase dykes are aphanitic and holocrystalline. Porphyritic textures are the common texture type with larger olivine crystals and smaller plagioclase laths. Gabbros cross-cut by clinopyroxene-bearing diabase dykes are also phaneritic and holocrystalline. Porphyritic texture is also a common fabric with larger olivine crystals and smaller plagioclase laths. Ultramafics, on the other hand, are cross-cut by both clinopyroxene-bearing and amphibole-bearing diabase dykes. They are made up of serpentinite and carbonatized

ultramafics. Serpentinites are composed of fully serpentine minerals and carbonatized ultramafics contain primary clinopyroxenes and secondary calcites.

Investigating 15 representative diabase samples according to their classification, source of magma and tectonic environment by using several diagrams made up of harker diagrams, multi-element diagrams and tectonic discrimination diagrams points out that there are two types of diabbases, Type 1 and Type 2. Type 1 diabbases have an enriched mantle source (e.g. E-MORB) and show similar geochemical traces with Mid-Atlantic ridge and Mariana back-arc basin and Type 2 have a depleted mantle source (e.g. BABB) and similar geochemical features with Mariana back-arc basin lavas. These groups are also having similarities with their petrographical features. Type 1 diabbases are clinopyroxene-bearing diabase rocks and Type 2 diabbases are amphibole-bearing diabase rocks which were explained in chapter 3 in detail.

In classification diagrams, Nb/Y vs.  $Zr/TiO_2 \cdot 0.0001$  diagram (Winchester and Floyd (1977) modified by Pearce (1996)) shows both types are subalkaline basalt. AFM diagram illustrates a distributed appearance due to mobility of the elements but comparison of different geological environments with the studied samples suggest that Type 1 diabbases show similarities with tholeiitic samples of Mariana back-arc basin basalts (Pearce et al., 2005) and Mid-Atlantic Ridge basalts (Niu et al., 2001) while Type 2 show similarities with tholeiitic samples of Mariana back-arc basin basalts (Pearce et al., 2005).

Some of the bivariate diagrams shows fractional crystallization trends but most of them do not present any trend because of the effect of the hydrothermal alteration. Due to mobility of major oxides under alteration, these bivariate diagrams give generally distributed appearances so that it is not possible to interpret any fractional crystallization trends.

N-MORB normalized multi-element diagrams show an enrichment of elements (e.g. Th, La, Ce, Pr) relative to other elements (e.g. Yb, Y, Dy, Ti) in both types. The N-MORB-like Nb contents and negative Nb anomaly relative to Th and La for Type 2 diabbases points out that they had been derived from depleted asthenospheric mantle source that has been metasomatized by slab-derived fluids/melts. This negative Nb

anomaly is not seen in Type 1 diabases. All the elements in both types are generally more enriched than N-MORB values but more immobile elements have almost similar composition with N-MORB. Chondrite-normalized REE diagrams illustrate higher enrichment of LREE than HREE for Type 1 diabases, but the pattern is almost parallel for Type 2 diabases, which can be interpreted by smaller degree of partial meltings of Type 1 than that of Type 2. Also, depletion of HREE relative to LREE of Type 1 may be interpreted by garnet or spinel lherzolite source. Eu concentration has negative anomalies for some samples in Type 2. This negative Eu anomaly may imply extraction of plagioclase in the source or removal of plagioclase phenocrysts from the melt at a later time (Gao and Wedepohl, 1995).

All Type 1 diabases are derived from an enriched asthenospheric mantle source (e.g. E-MORB) in all ratio diagrams. All ratio diagrams also display that Type 1 have a similar source with Mid-Atlantic ridge having an enriched mantle source like E-MORB (Niu et al., 2001). Nb/Yb vs. Th/Yb diagram just show similar source of Type 1 with Mariana back-arc (Pearce et al., 2005). On the other hand, all Type 2 diabases have a more depleted asthenospheric mantle source (e.g. N-MORB) than Type 1. All ratio diagrams display a similar source of Type 2 with Mariana back-arc (Pearce et al., 2005). Some diagrams (e.g. Zr/Nb vs. Th/Nb; Zr/Nb vs. Zr/Y; Zr/Y vs. Nb/Y; Nb/Yb vs. Th/Yb) also show a similar source with Greater Antilles Island Arc (Jolly et al., 1998) and others (e.g. Zr/Nb vs. Zr/Y; Zr/Y vs. Nb/Y) display a similar source with South Sandwich Island Arc (Pearce et al., 1995).

Model of Sm/Yb vs. Dy/Yb by Sayit et al. (2016) was used to understand the degree of partial melting and to answer the question of whether diabases were originated from a spinel or garnet mantle source. The model suggests that both types were produced from a spinel-bearing source. Moreover, model displays that Type 1 diabases generally have smaller degrees of partial melting than Type 2, which is also seen in Chondrite-normalized rare earth element diagrams.

Tectonic discrimination diagrams of Ti/Y vs. Zr/Y exhibit that both types have a plate-margin environment, Ti/1000 vs. V display BAB/MOR environment of both types and Hf/3-Th-Nb/16 shows that E-MORB environment of Type 1 and Arc-basalts environment of Type 2. Beside of these three tectonic discrimination diagrams,

comparison of N-MORB normalized multi-element diagrams with different environments exhibit that Type 1 has very similar pattern with E-MORB (Sun and McDonough, 1989) and with also Mariana back-arc (Pearce et al., 2005) without the presence of negative Nb anomaly. Type 1 have no similar appearance with continental arcs because Aolian continental arc (Calanchi et al., 2002) and Andes continental arc (Compilation of Winter, 2001 after Thorpe et al., 1984) have much more enrichment in the less immobile elements (e.g. Th, Nb, La, Ce, Nd) than Type 1. Hence, they are not derived from a continental arc environment. They also have no similar appearance with South Sandwich island arc (Pearce et al., 1995) and Greater Antilles island arc (Jolly et al., 1998) because Greater Antilles island arc has much more depletion in immobile elements (e.g. Zr, Hf, Ti, Dy, Y, Yb) than Type 1 and South Sandwich island arc has much more depletion in all elements than Type 1. Thus, they were again not derived from island arc environments. Type 2 diabases have similar pattern with Mariana back-arc (Pearce et al., 2005). They do not have any similar patterns with island arcs and continental arcs. Aolian continental arc (Calanchi et al., 2002) and Andes continental arc (Compilation of Winter, 2001 after Thorpe et al. (1984)) have also much more enrichment in mobile elements (e.g. Th, Nb, La, Ce, Nd) than Type 2. Greater Antilles island arc ( Jolly et al., 1998) has more depletion in immobile elements (e.g. Zr, Hf, Ti, Dy, Y, Yb) than Type 2 and South Sandwich island arc (Pearce et al., 1995) has more depletion in all elements than Type 2. Therefore, Type 2 also were not derived from continental or island arc environments.

In compilation of all geochemical data, Type 1 diabases can be interpreted that they were derived from an enriched asthenospheric mantle source (e.g. E-MORB) and in the stability of spinel field and formed in a mid-ocean ridge or back-arc basin environment. On the other hand, Type 2 diabases can be explained by means of that they were sourced from a more depleted asthenospheric mantle source (e.g. N-MORB) and in the stability of spinel field having larger degrees of partial melting than Type 1 and formed in a back-arc basin environment.

In this study, two  $^{40}\text{Ar}$ - $^{39}\text{Ar}$  age have been taken from two Type 2 diabase samples (HT-16 and HT-20-A) which are the least affected samples from hydrothermal alteration. The analysis were undergone by single crystal incremental-heating method

of primary hornblende crystals. HT-16 gives plateau age of  $176.30 \pm 0.52$  Ma (Toarcian) and HT-20-A gives plateau age of  $178.82 \pm 0.80$  Ma (Toarcian) as cooling ages. The ages are crucial because they are exactly from IAE ophiolitic mélange and the ages also prove that they are not younger post-collisional dykes. Therefore, the age of these dykes can be used to interpret geodynamical evolution of IAE Ocean.

Studied diabase dykes are found as isolated mafic dykes within the IAE Suture which is one of the Northern branch of Neo-Tethys whose remnants are called Alpide Sutures (e.g. Şengör and Yılmaz, 1981; Şengör et al., 1988). In Alpide Sutures, isolated diabase dykes have been worked in several studies (e.g. Weijermars, 1991; Bernoulli et al., 2003; Dilek and Thy, 2006; Çelik and Chiaradia, 2008; Çolakoğlu et al., 2012). Geochemistry of some studies (e.g. Weijermars, 1991 (Betic Zone); Bernoulli et al., 2003 (Alpine)) exhibits forming of diabase dykes in the stage of thinning of continental crust and rifting resulting in opening of Neo-Tethys Ocean. On the other hand, geochemistry of other studies (e.g. Bozovic et al., 2013 (Vardar Zone), Tankut et al., 1998; Dilek and Thy, 2006 (Ankara Mélange), Parlak and Delaloye, 1996 (Mersin ophiolite), Parlak, 2000; Çelik, 2007; Çakır, 2009 (Pozanti-Karsanti ophiolite), Vergili and Parlak, 2005 (Pınarbaşı ophiolite), Çelik and Delaloye, 2003; Çelik and Chiaradia, 2008 (Lycian ophiolite), Bağcı and Parlak, 2009 (Tekirova ophiolite), Parlak et al., 2012 (İspendere ophiolite), Çolakoğlu et al., 2012 (East of Van), Galoyan et al., 2009; Rolland et al., 2010 (Sevan/Akera Ophiolites), Ao et al., 2016 (Zagros ophiolite)) points out forming of isolated diabase dykes in an intra-oceanic arc-back arc or fore-arc environment. The studies (e.g. Parlak et al., 2006) in Northern branch of Neo-tethys in Turkey and the studies (e.g. Bozovic et al., 2013) from its western extension, Vardar Zone, have indicated intra-oceanic back-arc basin for the isolated diabase dykes. Also, the studies from Southern branch of Neo-tethys (e.g. Çolakoğlu et al., 2012) and the studies (e.g. Lugovic et al., 1991) from the Dinaric Ophiolite Belt which is the western extension of Southern branch of Neo-tethys have indicated intra-oceanic back-arc basin origin of isolated diabase dykes. The studies (e.g. Galoyan et al., 2009; Rolland et al., 2010) of Sevan/Akera ophiolites which is the eastern extension of IAE ophiolites also have shown intra-oceanic back-arc origin of isolated diabase dykes.

The diabase dykes studies in this thesis are made up of two Types which are Type 1 cross-cutting ultramafics, gabbros and pillow basalts and Type 2 cross-cutting just carbonatized ultramafics according to field observations. In Vardar Zone, western extension of IAE suture, the isolated diabase dykes cross-cut gabbros, sheeted dykes and pillow basalts and in Sevan/Akera ophiolites, eastern extension of IAE suture, the isolated diabase dykes just cross-cut layered gabbros. Therefore, they show similarities to studied diabases.

Both diabase types were formed in an intra-oceanic environment. Type 2 diabases cross-cutting carbonatized ultramafics were formed in a back-arc basin environment. On the other hand, Type 1 diabases cross-cutting ultramafics, gabbros and pillow basalts were formed in a typical mid-ocean ridge or back-arc basin environment. Other parts within IAE suture zone has interesting stories. Tankut et al, (1998) found two different dyke groups formed Mid-ocean ridge and island arc environments, respectively in Ankara Mélange. Parlak et al, (2006) found isolated diabase dykes having OIB-like enriched source resulted from an asthenospheric window formed in an island arc environment within Divriği ophiolites, Sivas. Dilek and Thy (2006) found diabase dykes formed in a back-arc basin environment in Ankara Mélange. They also found a U-Pb age of a  $179 \pm 15$  Ma from plagiogranites that are coeval with those diabase dykes. However, according to them, this back-arc basin was responsible for the opening of the IAE Ocean despite of their intra-oceanic back-arc basin geochemistry signatures. Sarifakioğlu et al, (2010) also found diabase dykes formed in a fore-arc environment from Orhaneli ophiolites. Hence, workers in regions within IAE suture zone found isolated diabase dykes which were formed in an intra-oceanic subduction zone environment like studied dykes.

There is no radiometric age data from Hattuşaş Ophiolitic Mélange until our  $^{40}\text{Ar}$ - $^{39}\text{Ar}$  ages.  $179 \pm 15$  Ma U-Pb age of Dilek and Thy (2006) from plagiogranites that are coeval with diabase dykes in Ankara Mélange is the age from the closest location to our study area. However, their interpretation and acceptance of opening age of IAE Ocean of that age is a question mark for us according to our results. According to our results, there is an intra-oceanic back-arc basin forming our Type 2 dykes within IAE Ocean at Toarcian time. Therefore, before this time, IAE Ocean was still needed to

open so that there was a mechanism causing to form intra-oceanic subduction zone and then back-arc basin environment. Therefore, it may not be the case for the ones (e.g. Şengör, 1979; Şengör and Yılmaz, 1981; Görür et al., 1983, 1984; Okay and Tüysüz, 1999; Rojay et al., 2001, 2004) who say the IAE Ocean was started to open during Early Jurassic. Instead, our results support the the models accepting that IAE Ocean was started to open during Late Triassic (Carnian) by the ones (e.g. Tekin et al., 2002; Göncüoğlu et al., 2003, 2010; Tekin and Göncüoğlu, 2007, 2009; Sayit et al., 2015, 2017) may be more likely the case.

## CHAPTER 6

### CONCLUSION

1. Studied diabase dykes have been outcropped from Boğazkale, Çorum region within Hattuşaş ophiolites which are the parts of Izmir-Ankara-Erzincan (IAE) Suture Zone. Field observations exhibit that diabase dykes cross-cut ultramafics, gabbros and pillow basalts. Petrographically and geochemically different two types of diabbases have very similar appearances on the field.
2. Two different types of diabbases, Type 1 and Type 2, can be differentiated according to petrographical studies. Type 1 diabbases have clinopyroxene and plagioclase dominated petrography with ophitic to sub-ophitic textures. On the other hand, Type 2 diabbases have amphibole (hornblende) and plagioclase dominated petrography with poikilitic textures. Both samples have holocrystalline crystallinity and phaneritic granularity. Secondary minerals of chlorite, epidote and prehnite for Type 1 and chlorite, actinolite, prehnite and biotite for Type 2 indicate the effect of hydrothermal alteration.
3. Two different types of diabbases, Type 1 and Type 2, are also differentiated from geochemical analysis. Both diabbases have subalkaline tholeiitic character. Type 1 diabbases do not have negative Nb anomalies relative to Th and La in N-MORB normalized multi-element diagrams while Type 2 diabbases have a dramatical negative Nb anomalies relative to Th and La. Moreover, Type 1 diabbases have more enriched asthenospheric mantle source (e.g. E-MORB) than Type 2 which have more depleted asthenospheric mantle source with subduction components (e.g. BABB). According to tectonic discrimination

diagrams, Type 1 diabases were formed in a mid-ocean ridge or back-arc basin and Type 2 diabases were formed in a back-arc basin environment.

4. Geochronology of studied diabases have been performed by means of  $^{40}\text{Ar}/^{39}\text{Ar}$  system for Type 2 diabases. Two age datings from two Type 2 samples which have the least alteration indicate ages of  $176.30 \pm 0.52$  Ma and  $178.82 \pm 0.80$  Ma (Early Jurassic (Toarcian)). These ages are the first ages taken from Hattuşaş Ophiolitic Mélange until now.
5. IAE suture can be traced along its western and eastern extension. Vardar zone which is the western extension of IAE suture has a study of diabase dykes (Bozovic et al., 2013) indicating intra-oceanic back arc basin geochemistry and 166.4 Ma age from K-Ar radiometric age system. Sevan/Akera ophiolites which is the eastern extension of IAE suture have also studies of diabase dykes (Galoyan et al., 2009; Rolland et al., 2010) showing again back-arc basin geochemistry.  $^{40}\text{Ar}$ - $^{39}\text{Ar}$  (Hornblende) ages from gabbros intruded by diabase dykes in Sevan/Akera ophiolites give  $165.3 \pm 1.7$  Ma and  $178.7 \pm 2.6$  Ma, which points out that diabase dykes are younger than these ages. Therefore, studied diabases display similar radiometric ages and tectonic environments with Vardar Zone and Sevan/Ekera ophiolites.
6. Our geochronological and geochemical results supports the idea that accept the opening age of IAE Ocean as during Late Triassic (Carnian) rather than the idea that accept the opening age of it as during Early Jurassic.

## REFERENCES

- Akçay, A.E., Dönmez, M., Kara, H., Yergök, A.F., and Esentürk, K., 2007. 1:100000 ölçekli Türkiye Jeoloji Haritası: Yozgat – İ33 Paftası. Maden Tetkik ve Arama Genel Müdürlüğü, 80.
- Akıman, O., Erler, A., Göncüoğlu, M.C., Güleç, N., Geven, A., Türeli, K. and Kadioğlu, Y., 1993. Geochemical characteristics of granitoids along the western margin of the Central Anatolian Crystalline Complex and their tectonic implications. *Geol. Journ.*, 28, 371-382.
- Altınli, E., 1973. Orta Sakarya Jeolojisi. Cumhuriyetin 50. Yili Yerbilimleri Kongr., Tebligler. Maden Tektik Arama, Ankara, 159-191.
- Ao, S., Xiao, W., Jafari, M.K., Talebian, M., Chen, L., Wan, B., Ji, W., and Zhang, Z., 2016. U–Pb zircon ages, field geology and geochemistry of the Kermanshah ophiolite (Iran): From continental rifting at 79 Ma to oceanic core complex at ca. 36 Ma in the southern Neo-Tethys. *Gondwana Research*, 31, 305-318.
- Ateş, M., Ulu, Ü., Genç, Ş., İmİK, M., 2010. Boğazkale-Osmancık (Çorum) - Gümüşhacıköy (Amasya) Dolayının Jeolojisi. MTA. 11246.
- Bağcı, U., and Parlak, O., 2009. Petrology of the Tekirova (Antalya) ophiolite (Southern Turkey): evidence for diverse magma generations and their tectonic implications during Neotethyan-subduction. *Int J. Earth Sci. (Geol Rundsch)*, 98, 387–405.
- Bernoulli, D., Manatschal, G., Desmurs, L., and Müntener, O., 2003. Where did Gustav Steinmann see the trinity? Back to the roots of an Alpine ophiolite concept. *Geological Society of America, Special Paper*, 373.

- Blundy, J.D., Robinson, J.A.C., and Wood, B.J., 1998. Heavy REE are compatible in clinopyroxene on the spinel lherzolite solidus. *Earth and Planetary Science Letters*. 160, 493-504.
- Boillot, G., and Capdevilla, R., 1977. The Pyrenees: subduction and collision? *Earth planet. Sci. Lett.*, 35, 151-160.
- Bortolotti, V., Chiari, M., Göncüoğlu, M.C., Marcucci, M., Principi, G., Tekin, U.K., Saccani, E., and Tassinari, R., 2013. Age and geochemistry of basalt-chert associations in the ophiolites of the Izmir-Ankara mélange east of Ankara, Turkey: Preliminary data. *Ofioliti*. 38 (2), 157-173.
- Boudier, F., and Nicolas, A., 1986. Harzburgite and lherzolite subtypes in ophiolitic and oceanic environments. *Earth Planet. Sci. Lett.*, 76, 84-92.
- Boulin, J., and Bouyx, E., 1977. Introduction a la geologie de l'Hindou Kouch occidental. In *Livre a la Memoire de Albert F. de Lapparent*. Mem. h. ser. 8, Soc. Geol. France. 87- 105.
- Bozovic, M., Prelevic, D., Romer, R.L., Barth, M., Bogaard, P.V.D., and Boev, B., 2013. The Demir Kapija Ophiolite, Macedonia (FYROM): a Snapshot of Subduction Initiation within a Back-arc. *Journal of Petrology*, 54 (7). 1427-1453.
- Boztuğ, D., 1998. Post–Collisional Central Anatolian Alkaline Plutonism, Turkey. *Turkish Journ. Earth Sci.*, 7, 145-165.
- Boztuğ, D., 2000. S and A-type intrusive associations: geodynamic significance of synchronism between metamorphism and magmatism. In: Bozkurt, E., Winchester, J. and Piper, J.A., (eds.) *Tectonics and magmatism in Turkey and the Surrounding Area*. Geol. Soc. London Special Publ., 173, 441- 458.
- Bright, R.M., Amato, J.M., Denyszyn S.W., and Ernst E., 2014. U-Pb geochronology of 1.1 Ga diabase in the southwestern United States: Testing models for the origin of a post-Grenville large igneous province. *Lithosphere*, Geological Society of America.

- Brown, G.C., and Mussett, A.E., 1993. The inaccessible Earth: An integrated view of its structure and composition. Chapman & Hall. London.
- Calanchi, N., Peccerillo, A., Tranne, C.A., Lucchini, F., Rossi, P.L., Kempton, P., Barbieri, M., and Wu, T.W., 2002. Petrology and geochemistry of volcanic rocks from the island of Panarea: implications for mantle evolution beneath the Aeolian island arc (southern Tyrrhenian sea). *Journal of Volcanology and Geothermal Research*, 115, 367-395.
- Catlos, E.J., Huber, K., and Shin, T.A., 2013. Geochemistry and geochronology of meta-igneous rocks from the Tokat Massif, north-central Turkey: implications for Tethyan reconstructions. *Int. J. Earth Sci. (Geol Rundsch)*, 102, 2175–2198
- Colakoglu, A.R., Sayit, K., Günay K., and Göncüoğlu, M.C., 2012. Geochemistry of mafic dykes from the Southeast Anatolian ophiolites, Turkey: Implications for an intra-oceanic arc–basin system. *Lithos*, 132-133, 113-126.
- Coleman, R.G., 1971. Plate tectonic emplacement of upper mantle peridotites along continental edges. *Journal of Geophysical Research*, 76, 1212-1222.
- Coleman, R.G., 1977. *Ophiolites: Ancient Oceanic Lithosphere*. Springer Verlag. Berlin.
- Çakır, Ü., 2009. Structural and geochronological relationships of metamorphic soles of Eastern Mediterranean Ophiolites to surrounding units: indicators of intra-oceanic subduction and emplacement, *International Geology Review*, 51 (3), 189-215.
- Çelik, Ö.F., 2007. Metamorphic sole rocks and their mafic dykes in the eastern Tauride belt ophiolites (southern Turkey): implications for OIB-type magma generation following slab break-off. *Geol. Mag.*, 144 (5), 849-866.
- Çelik, Ö.F., 2008. Detailed geochemistry and K-Ar geochronology of the metamorphic sole rocks and their mafic dykes from the Mersin Ophiolite, Southern Turkey. *Turkish Journal of Earth Sciences*, 17, 685–708.

- Çelik, Ö.F., and Chiaradia, M., 2008. Geochemical and petrological aspects of dike intrusions in the Lycian ophiolites (SW Turkey): a case study for the dike emplacement along the Tauride Belt Ophiolites. *Int. J. Earth Sci. (Geol Rundsch)*, 97, 1151-1164.
- Çelik, Ö.F., and Delaloye, M., 2003. Origin of metamorphic sole rocks and their postkinematic mafic dyke swarms in the Antalya and Lycian Ophiolites, SW Turkey. *Geological Journal* 38, 235–256.
- Delaune-Mayere, M., Marcoux, J., Parrot, J.-F., and Poisson, A., 1977. Modele d'évolution Mésozoïque de la paleo-marge téthysienne au niveau des nappes radiaritiques et ophiolitiques du Taurus Lycien, d'Antalya et du Baer-Bassit. In: B. Biju-Duval and L. Montadert (Editors), *Structural History of the Mediterranean Basins*. Editions Technip, Paris, 79-94.
- Dewey, J.F., Pitman, W.C., III, Ryan, W.B.F., and Bonnin, J., 1973. Plate tectonics and the evolution of the Alpine System. *Geol. Sot. Am. Bull.*, 84, 3137-3180.
- Dilek, Y., and Eddy, C.A. 1992. The Troodos (Cyprus) and Kizildag (S. Turkey) ophiolites as structural models for slow-spreading ridge segments. *Journal of Geology*, 100, 305-322.
- Dilek, Y., and Robinson, P.T., 2003. Ophiolites in Earth history. *Geological Soc., London, Special Publications*, 218, 43-68.
- Dilek, Y., and Thy, P., 2006. Age and petrogenesis of plagiogranite intrusions in the Ankara mélange, central Turkey. *Island Arc*, 15, 44-57.
- Dilek, Y., Thy, P., Hacker, B., and Grundvig, S., 1999. Structure and petrology of Tauride ophiolites and mafic dyke intrusions (Turkey): implications for the Neotethyan ocean. *Geological Society of America Bulletin*, 111, 1192–1216.
- Duncan, R.A., and Al-Amri, A.M. 2013. Timing and composition of volcanic activity at Harrat Lunayyir, western Saudi Arabia. *Journal of Volcanology and Geothermal Research*, 260, 103-116.

- Dupuy, C., Marsh, J., Dostal, J., Michard, A., and Testa, S., 1988. Asthenospheric and lithospheric sources for Mesozoic dolerites from Liberia (Africa): trace element and isotopic evidence. *Earth and Planetary Science Letters*, 87, 100-110.
- Fletcher, I.R., Libby, W.G., and Rosman, K.J.R., 1987. Geological note: Sm-Nd dating of the 2411 Ma Jimberlana dyke, Yilgarn Block, Western Australia, *Australian Journal of Earth Sciences*, 34 (4), 523-525.
- Flowers, R.M., Bowring, S.A., Tulloch, A.J., and Klepeis, K.A., 2005. Tempo of burial and exhumation within the deep roots of a magmatic arc, Fiordland, New Zealand. *Geological society of America*, 33 (1), 17-20.
- Floyd, P.A., and Winchester, J.A., 1978. Identification and discrimination of altered and metamorphosed volcanic rocks using immobile elements, 21, 291-306.
- Floyd, P.A., Göncüoğlu, M.C., Winchester, J.A., and Yalınız, M.K., 2000. Geochemical character and tectonic environment of Neotethyan ophiolitic fragments and metabasites in the Central Anatolian Complex, Turkey. In: Bozkurt, E., Winchester, J. A. & Piper, J. D. A. (eds) *Tectonics and Magmatism in Turkey and the Surrounding Area*. Geological Society, London, Special Publications, 173, 183-202.
- Fourquin, C., 1975. L'Anatolie du Nord-Ouest, marge meridionale du continent europeen, histoire plaeogeographique, tectonique et magmatique durant le Secondaire et Tertiaire. *Bull. Soc. Geol. Fr., Ser. 7*, 17: 1058-1070.
- Galoyan, G., Rolland, Y., Sosson, M., Corsini, M., Billo, S., Verati, C., and Melkonyan, R., 2009. Geology, geochemistry and  $^{40}\text{Ar}/^{39}\text{Ar}$  dating of Sevan ophiolites (Lesser Caucasus, Armenia): Evidence for Jurassic Back-arc opening and hot spot event between the South Armenian Block and Eurasia. *Journal of Asian Earth Sciences*, 34, 135-153.
- Gao, S., and Wedepohl, K.H., 1995. The negative Eu anomaly in Archean sedimentary rocks: Implications for decomposition, age and importance of their granitic sources. *Earth and Planetary Science Letters*, 133, 81-94.

- Göncüoğlu, M.C., 1982. Zircon U/Pb ages from paragneisses of the Nigde Massif (Central Anatolia). *Geol. Soc. Turkey Bull.*, 25, 61-66.
- Göncüoğlu, M.C., 1989. Structural framework of the Anatolian Hercynites. 28th Int. Geol. Cong. Abstracts, 563-564.
- Göncüoğlu, M.C., 2010. Introduction to the Geology of Turkey: Geodynamic Evolution of the Pre-Alpine and alpine Terranes. General Directorate of Mineral. Res. Explor., Monography Series, 5, 1-66.
- Göncüoğlu, M.C., and Türeli, T.K., 1994. Alpine collisional-type granitoids from the Central Anatolian Crystalline Complex. *Journ. Kocaeli Univ.*, 1, 39-46.
- Göncüoğlu, M.C., Erler, A., Toprak, V., Yalınız, K., Olgun, E. and Rojay, B., 1992. Orta Anadolu Masifinin Batı Kesiminin Jeolojisi, Bölüm II. Orta Kesim: TPAO Rap.No:3155, 76.
- Göncüoğlu, M.C., Gürsu, S., Tekin, U.K., and Köksal, S., 2008. New data on the evolution of the Neotethyan oceanic branches in Turkey: Late Jurassic ridge spreading in the Intra-Pontide branch. *Ofioliti*, 33, 153-164.
- Göncüoğlu, M.C., Kozlu, H., and Dirik, K., 1997. Pre-Alpine and Alpine terranes in Turkey: explanatory notes to the terrane map of Turkey. *Ann. Geol. Pays Helleniques*, 37, 515-536.
- Göncüoğlu, M.C., Sayit, K., and Tekin, U.K., 2010. Oceanization of the northern Neotethys: Geochemical evidence from ophiolitic mélange basalts within the Izmir-Ankara suture belt, NW Turkey, *Lithos*, 116, 175-187.
- Göncüoğlu, M.C., Turhan, N., Şentürk, K., Özcan, A., Uysal, Ş., and Yalınız, K., 2000. A geotraverse across northwestern Turkey: tectonic units of the Central Sakarya region and their tectonic evolution. From: Bozkurt, E., Winchester, J. A. & Piper, J. D. A. (eds) *Tectonics and Magmatism in Turkey and the Surrounding Area*. Geological Society, London, Special Publications, 173, 139-161.
- Göncüoğlu, M.C., Turhan, N., and Tekin, K., 2003. Evidence for the Triassic rifting and opening of the Neotethyan Izmir-Ankara Ocean, northern edge of the

Tauride-Anatolide Platform, Turkey. Bull. Geol. Soc. Italy, Special Volume 2, 203-212.

Göncüoğlu, M.C., Yalınız, K., & Tekin, U.K., 2006a. Geochemical features and radiolarian ages of volcanic rocks from the Izmir-Ankara Suture Belt, Western Turkey. Proceed. Int Symp. Mesozoic Ophiolite Belts of the N Balkan Peninsula (Belgrade-BanjaLuka, 11 May-6 June, 2006) 41-44.

Göncüoğlu, M.C., Yalınız, K., and Tekin, U.K., 2006b. Geochemistry, Tectono-Magmatic Discrimination and Radiolarian Ages of Basic Extrusives within the Izmir-Ankara Suture Belt (NW Turkey): Time Constraints for the Neotethyan Evolution. Ofioliti, 31, 25-38.

Görür, N., Oktay, F.Y., Seymen, I., and Şengör, A.M.C., 1984. Palaeotectonic evolution of the Tuzgölü basin complex, central Turkey: sedimentary record of a Neo-Tethyan closure. Geol. Soc. London Spec. Pub., 17, 467-82.

Görür, N., Şengör, A. M. C., Yılmaz, Y., and Akkok, R., 1983. Pontidlerde Neo-Tetis'in Kuzey Kolunun açılmasına ilişkin sedimentolojik veriler. Türk. Jeol. Kur. Bülteni, 26, 11-20.

Gülmez, F., Genç, C.Ş., Keskin, M., and Tüysüz, O., 2012. A post-collision slab-breakoff model for the origin of the Middle Eocene magmatic rocks of the Armutlu–Almacık belt, NW Turkey and its regional implications. The Geological Society of London.

Green, T.H., 1980. Island arc and continent-building magmatism: A review of petrogenetic models based on experimental petrology and geochemistry. Tectonophys., 63, 367-385.

Harris, N.B.W., Kelley, S.P., and Okay, A.I., 1994. Post-collision magmatism and tectonics of northwest Turkey. Contrib. Mineral. Petrol., 117, 241-252.

Harrison, T.M., 1981. Diffusion of <sup>40</sup>Ar in Honblende. Contrib. Mineral Petrol., 78, 324-331.

- Hart, S.R., Erlank, A.J., and Kable, E.J.D., 1974. Sea Floor Basalt Alteration: Some Chemical and Sr Isotopic effects. *Contributions to Mineralogy and Petrology*, 44, 219-230.
- Hoeck, V., Ionescu, C., Balintoni, I., and Koller, F., 2009. The Eastern Carpathians “ophiolites” (Romania): Remnants of a Triassic ocean. *Lithos*, 108, 151-171.
- Hutton, J., 1795. *Theory of the Earth with proofs and illustrations*, Volume 1: London, Cadell, Junior and Davies, and Edinburgh, William Creech, viii + 620p. + iv plates.
- Jolly, W.T., Lidiak, E.G., Dickin, A.P., and Wu, T.W., 1998. Geochemical diversity of Mesozoic island arc tectonic blocks in eastern Puerto Rico. *Geological Society of America*, 322, 67.
- Kelley, S., 2002. K-Ar and Ar-Ar dating. Department of Earth Sciences, The Open University, 785-818.
- Koppers, A.A.P., Gowen, M.D., Colwell, L.E., Gee, J.S., Lonsdale, P.F., Mahoney, J.J., and Duncan R.A. 2010. New  $^{40}\text{Ar}/^{39}\text{Ar}$  age progression for the Louisville hot spot trail and implications for inter-hot spot motion. *Geochemistry, Geophysics, Geosystems*, 12, 12.
- Köksal, S., Romer, R.L., Göncüoğlu, M.C., and Toksoy-Köksal, F., 2004 Timing of the transition from the post-collisional to A-type magmatism: titanite U/Pb ages from the alpine Central Anatolian Granitoids, Turkey. *Int. Journ. Earth Sci.*, 93, 974-989.
- Köksal, S., Möller, A., Frei, D., Göncüoğlu, M. C., and Köksal-Toksoy, F., 2007. Petrological characteristics and LA-SF-ICP-MS U-Pb ages of S-type Granitoids from Central Turkey. *Geochim. Cosmochim Acta*, 71 (15) Suppl. 1 Goldschmidt 2007, 503.
- Köksal, S., Göncüoğlu, M.C., and Toksoy-Köksal F., 2008. Zircon typologies and internal structures as petrogenetic indicators in contrasting granitoid types from central Anatolia, Turkey. *Mineral Petrol.*, 93, 185-211.

- Laubscher, H.P., and Bernoulli, D., 1977. Mediterranean and Tethys. in: A.E.M. Nairn, W.H. Kanes and F.G. Stehli, (Editors), *The Ocean Basins and Margins*. 4A. The Eastern Mediterranean. Plenum, New York, pp. 1-28.
- Raymond, L.A., 1984. Classification of Melanges. Geological Society of America, Special Paper 198.
- Liu, S., Feng, C., Jahn, B., Hu, R., Gao, S., Coulson, I.M., Feng, G., Lai, S., Yang, C., and Yang, Y., 2013. Zircon U–Pb age, geochemical, and Sr–Nd–Hf isotopic constraints on the origin of mafic dykes in the Shaanxi Province, North China Craton, China. *Lithos*, 175-176, 244-254.
- Lugovic, B., Altherr, R., Raczek, I., Hofmann, A.W., and Majer, V., 1991. Geochemistry of peridotites and mafic igneous rocks from the Central Dinaric Ophiolite Belt, Yugoslavia. *Contrib. Mineral Petrol.*, 106, 201-216.
- Lumpkin, G.R. 1999. Physical and chemical characteristics of baddeleyite (monoclinic zirconia) in natural environments: an overview and case study. *Journal of Nuclear Materials*, 274, 206-217.
- Lytwyn, J.N., and Casey, J.F., 1995. The geochemistry of postkinematic mafic dike swarms and subophiolitic metabasites, Pozantı-Karsantı Ophiolite, Turkey: Evidence for ridge subduction. *Geological Society of American Bulletin*, 107, 830-850.
- Majidi, B., 1978. Etude petrostructurale de la region de Mashhad (Iran). Les problemes des metamorphites, serpentinites et granitoides “hercyniens”. These, Univ. Sci. Et Medic., Grenoble, 277.
- Marcoux, J., 1978. A scenario for the birth of a new oceanic realm: the Alpine Neotethys. *Proc. Int. Congr. Sedimentol.*, 10<sup>th</sup>, Jerus.
- Marroni, M., Frassi, C., Göncüoğlu, M.C., Di Vincenzo, G., Pandolfi, L., Rebay, G., Ellero, A., Ottria, G., 2014. Late Jurassic amphibolite facies metamorphism in the Intra-Pontide Suture Zone (Turkey): an eastward extension of the Vardar Ocean from the Balkans into Anatolia? *J Geol Soc.*, 171, 605–609.

- McDougall, I., and Harrison, T.M., 1999. *Geochronology and Thermochronology by the  $^{40}\text{Ar}/^{39}\text{Ar}$  method*. Oxford University Press, New York, 212.
- Michard, A., Mokhtari, A., Chalouan, A., Saddiqi, O., Rossi, P., and Rjimati, E., 2014. New ophiolite slivers in the External Rif belt, and tentative restoration of a dual Tethyan suture in the western Maghrebides. *Bull. Soc. Geol. France*, 185 (5), 313-328.
- Min, K.W., Mundil, R., Renne, P.R., and Ludwig, K.R., 2000. A test for systematic errors in  $^{40}\text{Ar}/^{39}\text{Ar}$  geochronology through comparison with U/Pb analysis of a 1.1-Ga rhyolite, *Geochim. Cosmochim. Acta*, 64(1), 73–98, doi:10.1016/S0016-7037(99)00204-5.
- Murton, B.J. 1990. Was the Southern Troodos transform fault a victim of microplate rotation? In: Malvas, J., Moores, E.M., Panayiotou, A. and Xenophontos, C. *Ophiolites: Oceanic crustal analogues. Proceedings of the symposium Troodos*. 1987. Geological Survey Department, Nicosia, 87-98.
- Nagasawa, H., Schreiber, H.D., and Morris, R.V., 1980. Experimental mineral/liquid partition coefficients of the rare Earth elements, Sc and Sr for perovskite, spinel and melilite. *Earth and Planetary Science Letters*, 46, 431-437.
- Niu, Y., Bideau, D., Hekinian, R., and Batiza, R., 2001. Mantle compositional control on the extent of mantle melting, crust production, gravity anomaly, ridge morphology, and ridge segmentation: a case study at the Mid-Atlantic Ridge 33-35°N. *Earth and Planetary Science Letters*, 186, 383-399.
- Okay, A.I., and Tüysüz, O., 1999. Tethyan sutures of northern Turkey. *Geol. Soc. London, Spec. Publ.*, 156, 475-515.
- Olsson, J.R., Söderlund, U., Klausen, M.B., and Ernst, R.E. 2010. U–Pb baddeleyite ages linking major Archean dyke swarms to volcanic-rift forming events in the Kaapvaal craton (South Africa), and a precise age for the Bushveld Complex. *Precambrian Research*, 183, 490-500.

- Önen, A.P., 2003. Neotethyan ophiolitic rocks of the Anatolides of NW Turkey and comparison with Tauride ophiolites. *Journ. Geol. Soc. London*, 160, 947-962.
- Önen, A.P., and Hall, R., 1993. Ophiolites and related metamorphic rocks from the Kütahta region, north-west Turkey. *Geol. Journ.*, 28, 399-412.
- Özcan, A., Erkan, A., Oral, A., Özer, S., Siimengen, M., and Tekeli, O., 1980. Basement geology of the area between North Anatolian Fault and the Kırşehir massif. Unpublished Mineral Research and Exploration Institute, Report No. 6722 [in Turkish].
- Pamic, J., Tomljenovic, B., and Balen, D., 2002. Geodynamic and petrogenetic evolution of Alpine ophiolites from the central and NW Dinarides: an overview. *Lithos*, 65, 113-142.
- Pandey, B.K., Gupta, J.N., Sarma, K.J., and Sastry, C.A., 1997. Sm-Nd, Pb-Pb and Rb-Sr geochronology and petrogenesis of the mafic dyke swarm of Mahbubnagar, South India: implications for Paleoproterozoic crustal evolution of the Eastern Dharwar Craton. *Precambrian Research*, 84, 181-196.
- Parlak, O., 2000. Geochemistry and significance of mafic dyke swarms in the Pozantı-Karsantı Ophiolite (Southern Turkey). *Turkish Journal of Earth Sciences*, 9, 29-38.
- Parlak, O., and Delaloye, M., 1996. Geochemistry and timing of postmetamorphic dike emplacement in the Mersin ophiolite (southern Turkey): new age constraints from  $^{40}\text{Ar}/^{39}\text{Ar}$  geochronology. *Terra Nova* 8, 585–592.
- Parlak, O., Karaoğlu, F., Rızaoğlu, T., Nurlu, N., Bağcı, U., Höck, V., Önal, A.Ö., Kürüm, S., and Topak, Y., 2012. Petrology of the İspendere (Malatya) ophiolite from the Southeast Anatolia: implications for the Late Mesozoic evolution of the southern Neotethyan Ocean. *The Geological Society of London*, 372.
- Parlak, O., Yılmaz, H., and Boztuğ, D., 2006. Origin and tectonic significance of the metamorphic sole and isolated dykes of the Divriği Ophiolite (Sivas, Turkey):

- Evidence for slab break-off prior to ophiolite emplacement. *Turkish Journal of Earth Sciences*, 15, 25-45.
- Pearce, J.A., 1996. A user's guide to basalt discrimination diagrams, in Wyman, D.A., ed., *Trace element geochemistry of volcanic rocks: Applications for massive sulphide exploration: Geological Association of Canada, Short Course Notes*, 12, 79-113.
- Pearce, J.A., 1982. The trace element characteristics of lavas from destructive plate boundaries. In: Thorpe, R.S., (ed.), *Andesites*, 525-548. New York: John Wiley and Sons.
- Pearce, J.A., Baker, P.E., Harvey, P.K., Luff, I.W., 1995. Geochemical evidence for subduction fluxes, mantle melting and fractional crystallization beneath the South Sandwich Island Arc. *J. Petrol.*, 36, 1073–1109.
- Pearce, J.A., and Gale, G.H., 1977. Identification of ore-deposition environment from trace-element geochemistry of associated igneous host rocks. *The Institution of Mining and Metallurgy and the Geological Society*, 7, 14-24.
- Pearce, J.A., Stern, R.J., Bloomer, S.H., and Fryer, P., 2005. Geochemical mapping of the Mariana arc-basin system: Implications for the nature and distribution of subduction components. *Geochem. Geophys. Geosyst.* 6 (7).
- Peng, P., Fu, L., MinGuo, Z., and JingHui, G., 2012. Age of the Miyun dyke swarm: Constraints on the maximum depositional age of the Changcheng System. *Chinese Science Bulletin*, 57, 105-110.
- Peters, T.j., Nicolas, A., and Coleman, R.G., 1991. *Ophiolite genesis and the evolution of the oceanic lithosphere*. Kluwer. Dordrecht.
- Robertson, A.H.F., 2000. Mesozoic-Tertiary tectonic-sedimentary evolution of a south Tethyan oceanic basin and its margins in southern Turkey. In: E. Bozkurt, J.A. Winchester and J.D. Piper (Eds.), *Tectonics and magmatism in Turkey and the surrounding area*. *Geol. Soc. London Spec. Publ.*, 173, 43-82.

- Robertson, A.H.F., 2002. Overview of the genesis and emplacement of Mesozoic ophiolites in the Eastern Mediterranean Tethyan region. *Lithos*, 65, 1-67.
- Robertson, A.H.F., 2004. Development of concepts concerning the genesis and emplacement of Tethyan ophiolites in the Eastern Mediterranean and Oman regions. *Earth Sci. Rev.*, 66, 331-387.
- Rojay, B., Altıner, D., Özkan-Altıner, S., Önen, P.A., James, S., And Thirlwall, M.W., 2004. Geodynamic significance of the Cretaceous pillow basalts from North Anatolian Ophiolitic Mélange Belt (Central Anatolia, Turkey): geochemical and paleontological constraints. *Geodyn. Acta*, 17 (5), 349-361.
- Rojay, B., Heimann, A., and Toprak, V., 2001. Neotectonic and volcanic characteristics of the Karasu fault zone (Anatolia, Turkey): The transition zone between the Dead Sea transform and the East Anatolian fault zone. *Geodinamica Acta*, 14, 197-212.
- Rolland, Y., Galoyan, G., Sosson, M., Melkonyan, R., and Avagyan, A., 2010. The Armenian Ophiolite: insights for Jurassic back-arc formation, Lower Cretaceous hot spot magmatism and Upper Cretaceous obduction over the South Armenian Block. *The Geological Society of London*, 340, 353-382.
- Rollinson, H.R., 1993. Using Geochemical data: Evaluation, Presentation, Interpretation. Longman/Wyllie. Harlow/New York.
- Sansone, T.C., Rizzo, G., and Mongelli, G., 2011. Petrochemical characterization of mafic rocks from the Ligurian ophiolites, southern Apennines. *International Geology Review*, 53 (1), 130-156.
- Sarıfakıoğlu, E., Özen, H., Çolakoğlu, A., and Sayak, H., 2010. Petrology, mineral chemistry, and tectonomagmatic evolution of Late Cretaceous suprasubduction-zone ophiolites in the İzmir–Ankara–Erzincan suture zone, Turkey. *International Geology Review*, 52:2-3, 187-222.
- Sayıt, K., Bedi, Y., Tekin, U.K., Göncüoğlu, M.C., and Okuyucu, C., 2017. Middle Triassic back-arc basalts from the blocks in the Mersin Mélange, southern

- Turkey: Implications for the geodynamic evolution of the Northern Neotethys. *Lithos.* 268-271.
- Sayit, K., Göncüoğlu, M.C., and Tekin, U.K., 2015. Middle Carnian arc-type basalts from the Lycian Nappes, Southwestern Anatolia: Early Late Triassic subduction in the Northern Branch of Neotethys. *The Journal of Geology*, 123.
- Sayit, K., Marroni, M., Göncüoğlu, M.C., Pandolfi, L., Ellero, A., and Frassi, C., 2016. Geological setting and geochemical signatures of the mafic rocks from the Intra-Pontide Suture Zone: implications for the geodynamic reconstruction of the Mesozoic Neotethys. *Int. J. Earth Sci. (Geol. Rundsch)*, 105, 39-64.
- Schmitt, A.K., Chamberlain, K.R., Swapp, S.M., and Harrison, T.M., 2010. In situ U–Pb dating of micro-baddeleyite by secondary ion mass spectrometry. *Chemical Geology*, 269, 386-395.
- Schoene, B., 2014. U-Th-Pb Geochronology. Princeton University, Princeton, NJ, USA.
- Shervais, M., 1982. Ti-V plots and the petrogenesis of modern and ophiolitic lavas. *Earth and Planetary Science Letters*, 59, 101-118.
- Shimizu, N., 1975. Rare earth elements in garnets and clinopyroxenes from garnet lherzolite nodules in kimberlites. *Earth and Planetary Science Letters*, 25, 26-32.
- Smith, A.G., Spray, J.G., 1984. A half-ridge transform model for the Hellenic–Dinaric ophiolites. In: Dixon, J.E., Robertson, A.H.F. (Eds.), *The Geological Evolution of the Eastern Mediterranean*. Special Publication-Geological Society of London, 17, 589– 603.
- Söderlund, U., and Johansson, L., 2002. A simple way to extract baddeleyite (ZrO<sub>2</sub>). *Geochemistry Geophysics Geosystems (G<sup>3</sup>)*. 3 (2).
- Söderlund, U., Isachsen, C.R., Bylund, G., Heaman, L.M., Patchett, P.J., Vervoort, J.D., Andersson, U.B., 2005. U–Pb baddeleyite ages and Hf, Nd isotope chemistry constraining repeated mafic magmatism in the Fennoscandian Shield from 1.6 to 0.9 Ga. *Contrib. Mineral Petrol.*, 150, 174-194.

- Stampfli, G. M., 2000. Tethyan oceans. In: Bozkurt, E., Winchester, J. A. and Piper, J. D. (eds) *Tectonics and Magmatism in Turkey and the Surrounding Area*. In: Bozkurt, E., Winchester, J. and Piper, J.A. (eds). *Tectonics and magmatism in Turkey and the Surrounding Area*. Geol. Soc. London Spec. Publ., 173, 1-23.
- Stenonis, N., 1669. *De Solidum intra Solidus Naturaliter Contento: Prodromus Dissertationis: Florentiae, Stellae*, 78 + [i] p. + 1 foldout.
- Stocklin, J., 1974. Possible ancient continental margins in Iran. In: C.A. Burk and CL. Drake (Editors), *The Geology of Continental Margins*. Springer, Berlin, 873-887.
- Stocklin, J., 1977. Structural correlation of the Alpine ranges between Iran and Central Asia. *Mem. h.-ser. Soc. Geol. Fr.*, 8, 333-353.
- Sun, S.S., and McDonough, W.F., 1989. Chemical and isotopic systematics of oceanic basalts: implications for mantle composition and processes. *Geological Society, London, Special Publications*, 42 (1), 313-345.
- Şengör, A.M.C., 1979. Mid-Mesozoic closure of Permo-Triassic Tethys and its implications. *Nature*, 279, 590-593.
- Şengör, A.M.C., and Yılmaz, Y., 1981. Tethyan evolution of Turkey: a plate tectonic approach. *Tectonophys.* 75, 181-241.
- Şengör, A.M.C., Burke, K., and Dewey, J.F., 1978. Rifts at high angles to orogenic belts: tests for their origin and the Upper Rhine Graben as an example. *Am. J. Sei.*, 278, 24-40.
- Şengör, A.M.C., Yılmaz, Y., and Sungurlu, O., 1984. Tectonics of the Mediterranean Cimmerides: nature and evolution of the western termination of Paleo-Tethys. In: Dixon, J. E., and Robertson, A. H. F., (eds). *The geological evolution of the Eastern Mediterranean*. Geol. Soc. London, Spec. Publ., 17, 77-112.
- Şengör, A.M.C., Altınır, D., Cin, A., Ustaömer, T., and Hsü, K. J., 1988. Origin and assembly of the Tethyside orogenic collage at the expense of Gondwana Land.

- In: Audley-Charles, M. G. & Hallam, A. (eds) Gondwana and Tethys, Geological Society, London, Special Publications, 37, 119-181.
- Şengör, A. M. C., Yılmaz, Y., and Sungurlu, O., 1984. Tectonics of the Mediterranean Cimmerides: nature and evolution of the western termination of Paleo-Tethys. Geol. Soc. London Spec. Pub. 17, 77-112.
- Tankut, A., Dilek, Y., and Önen, P., 1998. Petrology and geochemistry of the Neo-Tethyan volcanism as revealed in the Ankara melange, Turkey. Journal of Volcanology and Geothermal Research 85, 265-284.
- Tchouankoue, J.P., Wambo, N.A.S., Dongmo, A.K., and Li, X., 2014.  $^{40}\text{Ar}/^{39}\text{Ar}$  dating of basaltic dykes swarm in Western Cameroon: Evidence of Late Paleozoic and Mesozoic magmatism in the corridor of the Cameroon Line. Journal of African Earth Sciences, 93, 14–22.
- Tekin, U.K., and Göncüoğlu, M.C., 2007. Discovery of the oldest (upper Ladinian to middle Carnian) radiolarian assemblages from the Bornova Flysch Zone in western Turkey: Implications for the evolution of the Neotethyan Izmir-Ankara Ocean. Ofioliti, 32, 131-150.
- Tekin, U.K., and Göncüoğlu, M.C., 2009. Late Middle Jurassic (Late Bathonian-Early Callovian) radiolarian cherts from the Neotethyan Bornova Flysch Zone, Spil Mountains, Western Turkey. Stratigraphy and Geological Correlation, 17 (3), 298–308.
- Tekin, U.K., Bedi, Y., Okuyucu, C., Göncüoğlu, M.C., and Sayit, K., 2016. Radiolarian biochronology of upper Anisian to upper Ladinian (Middle Triassic) blocks and tectonic slices of volcano-sedimentary successions in the Mersin Mélange, southern Turkey: new insights for the evolution of Neotethys. Journal of African Earth Sciences, 124, 409–426.
- Tekin, U.K., Göncüoğlu, M.C., and Turhan, N., 2002., First evidence of Late Carnian radiolarian fauna from the Izmir-Ankara Suture Complex, Central Sakarya, Turkey: Implications for the opening age of the Izmir-Ankara branch of Neotethys. Geobios, 35, 127-135.

- Thompson, G., 1991. Metamorphic and hydrothermal processes: basalt-seawater interactions. In: Floyd, P.A., (ed.), *Oceanic Basalts*. Blackie, Glasgow and London, 148-173.
- Thorpe, R.S., Francis, P.W., and O'Callaghan, L., 1984. Relative roles of source composition, fractional crystallization and crustal contamination in the petrogenesis of Andean volcanic rocks. *Phil. Trans. R. Soc. Lond.*, A310, 675-692.
- Topuz, G., Çelik, Ö.F., Şengör, A.M.C., Altıntaş, İ.E., Zack, T., Rolland, Y., and Barth, M., 2013. Jurassic ophiolite formation and emplacement as backstop to a subduction-accretion complex in Northeast Turkey, the Refahiye ophiolites, and relation to the Balkan ophiolites. *American Journal of Science*, 313, 1054-1087.
- Trümpy, R., 1975. Penninic-Austroalpine boundary in the Swiss Alps: a presumed former continental margin and its problems. *Am. Jour. Sci.*, 275-A, 209-38.
- Vergili, Ö., and Parlak, O., 2005. Geochemistry and tectonic setting of metamorphic sole rocks and mafic dikes from the Pınarbaşı (Kayseri) Ophiolite, Central Anatolia (Turkey). *Ofioliti*, 30 (1), 37-52.
- Wang, Y., Zhao, G., Fan, W., Peng, T., Sun, L., and Xia X., 2007. LA-ICP-MS U–Pb zircon geochronology and geochemistry of Paleoproterozoic mafic dykes from western Shandong Province: Implications for back-arc basin magmatism in the Eastern Block, North China Craton. *Precambrian Research*, 154, 107–124.
- Weijermars, R., 1991. Geology and tectonics of the Betic Zone, SE Spain. *Earth-Science Reviews*, 31, 153-236.
- Winchester, J.A., and Floyd, P.A., 1976. Geochemical magma type discrimination application to altered and metamorphosed basic igneous rocks. *Earth and Planetary Science Letters*, 28, 459-469.
- Winchester, J.A., and Floyd, P.A., 1977. Geochemical discrimination of different magma series and their differentiation products using immobile elements. *Chemical geology*, 20, 325-343.

- Winter, J.D., 2001. An introduction to igneous and metamorphic petrology. Prentice Hall. New Jersey, 166.
- Wood, D.A., 1980. The application of a TH-Hf-Ta diagram to problems of tectonomagmatic classification and to establishing the nature of crustal contamination of basaltic lavas of the British Tertiary Volcanic Province. *Earth and Planetary Science Letters*, 50, 11-30.
- Wood, D.A., Joron, J.L., and Treuil, M., 1979. A reappraisal of the use of trace elements to classify and discriminate between magma series erupted in different settings. *Earth and Planetary Science Letters*, 45, 326-336.
- Wood, D.A., Gibson, I.L., and Thompson, R.N., 1976. Elemental mobility during zeolite facies metamorphism of the Tertiary basalts of eastern Iceland. *Contributions to Mineralogy and Petrology*, 55.3, 241-254.
- Wu, W.N., Schmitt, A.K., and Pappalardo, L., 2015. U-Th baddeleyite geochronology and its significance to date the emplacement of silica undersaturated magmas. *American Mineralogist*, 100, 2082-2090.
- Yaliniz, M.K., Göncüoğlu, M.C., Ozkan-Altiner, S., 2000. Formation and emplacement ages of the SSZ-type Neotethyan Ophiolites in Central Anatolia, Turkey: paleotectonic implications. *Geol Journ.*, 35, 53-68.
- Yılmaz, Y., 1990. Allochthonous terranes in the Tethyan Middle East, Anatolia and surrounding regions. *Phil. Trans. Roy. Soc., Lond.*, A 331, 611–624.

## APPENDICES

### APPENDIX A

#### GEOCHEMICAL ANALYSIS RESULTS

Table 1. Geochemical analysis results of Boğazkale diabases.

ELEMENT/SAMPLE NO	15-BOG-4B	15-BOG-6	15-BOG-7	15-BOG-8
SiO <sub>2</sub> (%)	50,43	51,12	51,83	49,58
Al <sub>2</sub> O <sub>3</sub> (%)	14,03	14,12	14,36	14,86
Fe <sub>2</sub> O <sub>3</sub> (T) (%)	12,83	12,54	10,02	14,02
MnO (%)	0,28	0,20	0,16	0,22
MgO (%)	7,47	6,82	8,63	5,97
CaO (%)	8,77	8,71	9,53	10,21
Na <sub>2</sub> O (%)	3,23	3,61	3,50	2,59
K <sub>2</sub> O (%)	0,25	0,67	0,66	0,68
TiO <sub>2</sub> (%)	1,55	1,38	1,21	2,02
P <sub>2</sub> O <sub>5</sub> (%)	0,17	0,14	0,13	0,19
LOI (%)	3,39	2,59	3,48	4
Total (%)	98,99	99,31	100,04	100,33
Sc (ppm)	40	39	38	38
V (ppm)	329	306	246	396
Cr (ppm)	60	60	240	60
Co (ppm)	46	44	40	43
Ni (ppm)	80	60	110	50

Table 1. Cont'd.

Rb (ppm)	3	8	9	9
Sr (ppm)	133	320	243	842
Y (ppm)	28,4	29,4	21,4	42,1
Zr (ppm)	95	81	66	125
Nb (ppm)	8,6	6,3	5,7	3,1
Cs (ppm)	0,3	0,3	0,2	0,6
Ba (ppm)	42	430	125	820
La (ppm)	7,78	6,62	5,57	6,26
Ce (ppm)	18,1	15,2	12,7	16,6
Pr (ppm)	2,58	2,16	1,77	2,58
Nd (ppm)	11,8	10,7	8,65	13,3
Sm (ppm)	3,74	3,28	2,61	4,58
Eu (ppm)	1,3	1,27	0,992	1,61
Gd (ppm)	4,46	4,42	3,44	6,06
Tb (ppm)	0,82	0,81	0,63	1,13
Dy (ppm)	5,11	5,11	3,87	7,21
Ho (ppm)	1,07	1,11	0,78	1,51
Er (ppm)	3,09	3,24	2,3	4,52
Tm (ppm)	0,471	0,504	0,344	0,674
Yb (ppm)	3,15	3,29	2,27	4,59
Lu (ppm)	0,481	0,488	0,346	0,738
Hf (ppm)	2,4	2,1	1,8	3,2
Ta (ppm)	0,69	0,48	0,47	0,25
Th (ppm)	0,74	0,62	0,58	0,54
U (ppm)	0,23	0,19	0,17	0,18
<b>ELEMENT/SAMPLE NO</b>	<b>15-BOG-12A</b>	<b>15-BOG-12B</b>	<b>HT-13</b>	<b>HT-15</b>
SiO <sub>2</sub> (%)	56,47	55,66	53,99	51,27
Al <sub>2</sub> O <sub>3</sub> (%)	13,69	14,05	14,32	14,90
Fe <sub>2</sub> O <sub>3</sub> (T) (%)	11,44	12,66	14,37	12,18
MnO (%)	0,20	0,19	0,20	0,20
MgO (%)	5,03	4,64	4,16	7,06
CaO (%)	6,15	6,14	5,10	8,34
Na <sub>2</sub> O (%)	4,73	4,89	5,73	4,63
K <sub>2</sub> O (%)	1,14	0,79	0,51	0,37
TiO <sub>2</sub> (%)	1,49	1,46	2,00	1,60
P <sub>2</sub> O <sub>5</sub> (%)	0,12	0,13	0,21	0,16
LOI (%)	1,89	2,26	3,04	3,4
Total (%)	100,46	100,61	100,59	100,72
Sc (ppm)	37	36	36	40

Table 1.Cont'd.

V (ppm)	364	358	443	322
Cr (ppm)	60	40	-	180
Co (ppm)	31	32	29	38
Ni (ppm)	60	80	30	70
Rb (ppm)	34	22	6	5
Sr (ppm)	406	248	344	164
Y (ppm)	31,2	30,3	39,3	33,5
Zr (ppm)	82	81	105	102
Nb (ppm)	2,6	2,1	2,5	2,5
Cs (ppm)	0,6	0,6	0,1	1,1
Ba (ppm)	215	107	107	61
La (ppm)	4,35	4,29	7,34	5,71
Ce (ppm)	11,4	11,4	17,3	15,1
Pr (ppm)	1,8	1,81	2,57	2,27
Nd (ppm)	9,5	9,41	13,5	11,4
Sm (ppm)	3,43	3,16	4,44	3,85
Eu (ppm)	0,863	0,937	1,57	1,32
Gd (ppm)	4,47	4,4	5,84	4,93
Tb (ppm)	0,83	0,82	1,08	0,91
Dy (ppm)	5,38	5,31	6,93	6
Ho (ppm)	1,18	1,12	1,45	1,26
Er (ppm)	3,43	3,35	4,17	3,57
Tm (ppm)	0,527	0,514	0,617	0,539
Yb (ppm)	3,33	3,45	4,1	3,61
Lu (ppm)	0,546	0,535	0,657	0,548
Hf (ppm)	2,2	2,3	2,8	2,7
Ta (ppm)	0,24	0,19	0,24	0,23
Th (ppm)	0,47	0,49	0,61	0,51
U (ppm)	0,16	0,15	0,33	0,17
<b>ELEMENT/SAMPLE NO</b>	<b>HT-16</b>	<b>HT-19</b>	<b>HT-20A</b>	<b>HT-22</b>
SiO <sub>2</sub> (%)	52,00	51,19	50,05	50,61
Al <sub>2</sub> O <sub>3</sub> (%)	14,53	14,84	14,45	14,73
Fe <sub>2</sub> O <sub>3</sub> (T) (%)	14,83	12,64	12,96	11,82
MnO (%)	0,20	0,20	0,22	0,19
MgO (%)	4,65	5,77	8,81	5,98
CaO (%)	7,59	9,43	7,09	11,38
Na <sub>2</sub> O (%)	4,63	3,55	3,82	2,73
K <sub>2</sub> O (%)	0,27	0,28	0,41	0,73
TiO <sub>2</sub> (%)	1,96	1,59	1,65	1,37

Table 1. Cont'd.

P2O5 (%)	0,18	0,14	0,14	0,11
LOI (%)	2,3	2,09	3,8	2,38
Total (%)	100,83	99,63	99,59	99,65
Sc (ppm)	37	39	36	37
V (ppm)	482	364	385	348
Cr (ppm)	30	50	20	80
Co (ppm)	36	39	35	36
Ni (ppm)	170	40	30	40
Rb (ppm)	5	4	7	15
Sr (ppm)	109	723	260	399
Y (ppm)	35,6	32,5	32,1	28,3
Zr (ppm)	98	95	77	69
Nb (ppm)	2,2	2,6	1,8	1,5
Cs (ppm)	0,4	0,1	2	1,2
Ba (ppm)	64	157	89	430
La (ppm)	6,08	5,22	3,84	3,53
Ce (ppm)	15,7	13,6	10,4	9,5
Pr (ppm)	2,38	2,07	1,67	1,53
Nd (ppm)	11,7	10,5	8,79	8,32
Sm (ppm)	3,98	3,59	3,19	2,93
Eu (ppm)	1,42	1,32	1,1	1,16
Gd (ppm)	5,32	4,77	4,65	3,99
Tb (ppm)	1,01	0,9	0,84	0,74
Dy (ppm)	6,5	5,66	5,5	4,72
Ho (ppm)	1,34	1,21	1,22	0,99
Er (ppm)	3,8	3,5	3,52	3
Tm (ppm)	0,585	0,559	0,539	0,459
Yb (ppm)	4,03	3,69	3,58	3,06
Lu (ppm)	0,635	0,557	0,555	0,486
Hf (ppm)	2,6	2,5	2,1	1,9
Ta (ppm)	0,03	0,22	0,18	0,15
Th (ppm)	0,63	0,47	0,34	0,29
U (ppm)	0,19	0,18	0,13	0,11
<b>ELEMENT/SAMPLE NO</b>	<b>HT-37</b>	<b>15-BOG-1</b>	<b>16-BOG-1</b>	
SiO2 (%)	52,62	50,62	50,17	
Al2O3 (%)	15,37	15,44	14,83	
Fe2O3(T) (%)	13,77	12,32	11,78	
MnO (%)	0,23	0,21	0,16	
MgO (%)	5,31	8,32	7,42	

Table 1. Cont'd.

CaO (%)	6,11	8,15	10,04
Na <sub>2</sub> O (%)	4,31	3,50	3,38
K <sub>2</sub> O (%)	1,00	0,19	0,61
TiO <sub>2</sub> (%)	1,81	1,47	1,52
P <sub>2</sub> O <sub>5</sub> (%)	0,15	0,15	0,13
LOI (%)	2,27	5,21	2,92
Total (%)	100,67	100,37	100,05
Sc (ppm)	34	43	38
V (ppm)	408	342	297
Cr (ppm)	30	100	260
Co (ppm)	34	42	37
Ni (ppm)	20	80	100
Rb (ppm)	14	2	9
Sr (ppm)	751	107	185
Y (ppm)	38,8	28,6	32,9
Zr (ppm)	104	76	82
Nb (ppm)	2	5,5	3,9
Cs (ppm)	7,7	-	-
Ba (ppm)	1010	38	42
La (ppm)	5,14	5,71	4,37
Ce (ppm)	13,8	14,1	11,4
Pr (ppm)	2,18	1,96	1,71
Nd (ppm)	11,7	9,31	9,17
Sm (ppm)	3,89	3,09	3,13
Eu (ppm)	1,39	1,2	1,18
Gd (ppm)	5,41	4,01	4,64
Tb (ppm)	1,04	0,71	0,86
Dy (ppm)	6,58	4,56	5,59
Ho (ppm)	1,42	0,97	1,15
Er (ppm)	4,21	2,95	3,29
Tm (ppm)	0,653	0,418	0,48
Yb (ppm)	4,12	2,71	3,01
Lu (ppm)	0,663	0,431	0,484
Hf (ppm)	2,8	2	2,2
Ta (ppm)	0,18	0,45	0,29
Th (ppm)	0,44	0,62	0,46
U (ppm)	0,16	0,16	0,12

## APPENDIX B

### <sup>40</sup>Ar/<sup>39</sup>Ar GEOCHRONOLOGY ANALYSIS RESULTS

#### HT-20-A

Table 2. Incremental heating results of HT-20-A sample.

Incremental Heating		36Ar(a) [fA]	37Ar(ca) [fA]	38Ar(cl) [fA]	39Ar(k) [fA]	40Ar(r) [fA]	Age ± 2σ (Ma)	40Ar(r) (%)	39Ar(k) (%)	K/Ca ± 2σ
17D27994	0,8 %	0,253555	6,3835	0,0033720	0,693784	6,6881	27,99 ± 3,58	8,19	0,82	0,0467 ± 0,0035
17D27996	1,3 %	0,508265	15,6331	0,0150500	1,684329	15,7317	27,13 ± 2,18	9,48	1,99	0,0463 ± 0,0015
17D27997	1,8 %	0,524823	14,9580	0,0000000	1,597818	20,2415	36,70 ± 2,44	11,54	1,89	0,0459 ± 0,0016
17D27998	2,0 %	0,397567	10,5475	0,0029230	1,080985	17,5666	46,94 ± 3,41	13,01	1,28	0,0441 ± 0,0022
17D28000	2,2 %	0,346566	9,2445	0,0128955	0,852944	17,1479	57,89 ± 4,28	14,34	1,01	0,0397 ± 0,0024
17D28002	2,4 %	0,364373	9,3831	0,0121252	0,744851	18,9013	72,77 ± 5,55	14,93	0,88	0,0341 ± 0,0023
17D28003	2,7 %	0,328528	9,2513	0,0000000	0,728977	19,2887	75,82 ± 5,76	16,58	0,86	0,0339 ± 0,0024
17D28005	3,0 %	0,349561	8,8572	0,0000000	0,652796	20,9377	91,50 ± 7,64	16,85	0,77	0,0317 ± 0,0026
17D28006	3,5 %	0,541900	11,9240	0,0000000	1,047865	34,6289	94,21 ± 4,95	17,78	1,24	0,0378 ± 0,0018
17D28007	4,0 %	0,389093	9,6906	0,0000000	0,842166	32,2625	108,76 ± 6,51	21,91	1,00	0,0374 ± 0,0022
17D28009	4,5 %	0,343802	9,2667	0,0057437	0,761266	33,2787	123,60 ± 8,16	24,67	0,90	0,0353 ± 0,0024
17D28010	5,0 %	0,372999	11,1835	0,0000000	0,739547	38,0272	144,53 ± 9,31	25,65	0,88	0,0284 ± 0,0019
17D28011	5,6 %	0,365589	13,2738	0,0000000	0,787670	38,5396	137,79 ± 8,33	26,29	0,93	0,0255 ± 0,0016
17D28013	6,2 %	0,612031	24,9287	0,0190997	1,105368	52,5307	133,98 ± 6,22	22,51	1,31	0,0191 ± 0,0008
17D28014	6,8 %	0,529684	27,5983	0,0133859	1,114092	56,6394	142,96 ± 6,38	26,57	1,32	0,0174 ± 0,0007
17D28015	7,4 %	0,475156	24,5066	0,0223206	1,173774	59,6437	142,89 ± 6,23	29,81	1,39	0,0206 ± 0,0009
17D28017	8,0 %	0,402197	29,1180	0,0000000	1,237580	70,8828	160,28 ± 6,47	37,36	1,47	0,0183 ± 0,0008
17D28018	8,7 %	0,337332	43,7573	0,0099872	1,679329	103,7621	172,33 ± 4,89	51,00	1,99	0,0165 ± 0,0005
17D28019	9,4 %	0,326036	89,9667	0,1172807	2,945139	189,5170	179,13 ± 2,78	66,30	3,49	0,0141 ± 0,0002
17D28021	10,0 %	0,253492	78,0136	0,0788110	2,830362	184,3550	181,21 ± 2,92	71,11	3,35	0,0156 ± 0,0003
17D28022	10,8 %	0,241075	97,8438	0,1252195	3,557628	234,1126	182,98 ± 2,38	76,67	4,21	0,0156 ± 0,0002
17D28023	11,7 %	0,168329	177,5099	0,2458138	4,760721	312,5965	182,60 ± 1,81	86,27	5,64	0,0115 ± 0,0001
17D28025	12,7 %	0,191356	229,6744	0,3199431	5,726496	370,4730	180,04 ± 1,44	86,76	6,78	0,0107 ± 0,0001
17D28026	13,8 %	0,161277	276,6553	0,4086669	6,413175	412,9292	179,23 ± 1,37	89,65	7,60	0,0100 ± 0,0001
17D28027	14,8 %	0,177107	341,7784	0,5466403	7,232485	461,2516	177,61 ± 1,24	89,81	8,57	0,0091 ± 0,0001
17D28029	16,0 %	0,214843	414,6160	0,6690754	8,190524	523,4782	177,97 ± 1,03	89,18	9,70	0,0085 ± 0,0001
17D28030	17,0 %	0,191543	327,9487	0,4729597	6,719361	429,8923	178,14 ± 1,27	88,36	7,96	0,0088 ± 0,0001
17D28031	18,0 %	0,201307	347,6912	0,5001494	6,883365	446,2114	180,39 ± 1,30	88,24	8,15	0,0085 ± 0,0001
17D28033	19,0 %	0,177486	257,4240	0,3492197	4,985533	320,2921	178,85 ± 1,71	85,93	5,90	0,0083 ± 0,0001
17D28034	20,3 %	0,105293	121,8298	0,1835618	2,363242	154,6562	182,02 ± 3,51	83,25	2,80	0,0083 ± 0,0002
17D28035	22,5 %	0,062457	76,4326	0,1197341	1,445459	92,8746	178,87 ± 5,57	83,42	1,71	0,0081 ± 0,0003
17D28037	23,3 %	0,045678	41,4391	0,0452385	0,842729	52,2291	172,83 ± 8,84	79,46	1,00	0,0087 ± 0,0005
17D28038	24,4 %	0,039429	29,1451	0,0612402	0,565248	35,9195	177,00 ± 13,84	75,51	0,67	0,0083 ± 0,0007
17D28040	25,3 %	0,028662	23,3336	0,0771230	0,443999	28,2470	177,19 ± 18,27	76,93	0,53	0,0082 ± 0,0009
Σ		10,028390	3220,8078	4,4375799	84,430606	4905,7342				
Information on Analysis		Results		40(r)/39(k) ± 2σ		Age ± 2σ (Ma)		MSWD	39Ar(k) (%),n	K/Ca ± 2σ
Project = SAYIT (16-34) Sample = HT-20-A Material = Hornblende Location = BoÅYazkale Region = Åtorum Analyst = Dan Miggins Irradiation = 17-OSU-06 (6X25-17) J = 0.00161820 ± 0.00000102 FCT-NM = 28.201 ± 0.023 Ma		Age Plateau Error Mean		64,23136 ± 0,28881 ± 0,45%		178,82 ± 0,80 ± 0,44% Full External Error ± 4,02 Analytical Error ± 0,77		2,51 1%	59,17 9	0,0089 ± 0,0005
		Total Fusion Age		58,10374 ± 0,20046 ± 0,34%		162,50 ± 0,57 ± 0,35% Full External Error ± 3,63 Analytical Error ± 0,54			34	0,0113 ± 0,0000
								2,00 1,5846	2σ Confidence Limit Error Magnification	

Table 3. Inverse isochron data of HT-20-A sample.










Inverse Isochron		39(k)/40(a+r) ± 2σ		36(a)/40(a+r) ± 2σ		r.i.	
17D27994	0,8 %	0,0085008 ± 0,0005679		0,00310677 ± 0,00003018		0,0221	
17D27996	1,3 %	0,0101512 ± 0,0003016		0,00306324 ± 0,00002388		0,0327	
17D27997	1,8 %	0,0091134 ± 0,0002742		0,00299340 ± 0,00002309		0,0272	
17D27998	2,0 %	0,0080045 ± 0,0003598		0,00294390 ± 0,00002534		0,0151	
17D28000	2,2 %	0,0071341 ± 0,0004006		0,00289872 ± 0,00002396		0,0111	
17D28002	2,4 %	0,0058847 ± 0,0003775		0,00287875 ± 0,00002211		0,0027	
17D28003	2,7 %	0,0062644 ± 0,0004121		0,00282316 ± 0,00002294		0,0032	
17D28005	3,0 %	0,0052546 ± 0,0004040		0,00281375 ± 0,00002140		0,0020	
17D28006	3,5 %	0,0053803 ± 0,0002344		0,00278239 ± 0,00001907		0,0014	
17D28007	4,0 %	0,0057197 ± 0,0003163		0,00264259 ± 0,00002015		0,0018	
17D28009	4,5 %	0,0056444 ± 0,0003592		0,00254910 ± 0,00002059		0,0016	
17D28010	5,0 %	0,0049886 ± 0,0003140		0,00251604 ± 0,00001984		0,0013	
17D28011	5,6 %	0,0053740 ± 0,0003167		0,00249428 ± 0,00001910		0,0016	
17D28013	6,2 %	0,0047362 ± 0,0001991		0,00262240 ± 0,00001786		0,0010	
17D28014	6,8 %	0,0052265 ± 0,0002187		0,00248490 ± 0,00001796		0,0011	
17D28015	7,4 %	0,0058673 ± 0,0002446		0,00237516 ± 0,00001786		0,0013	
17D28017	8,0 %	0,0065228 ± 0,0002608		0,00211982 ± 0,00001699		0,0013	
17D28018	8,7 %	0,0082545 ± 0,0002365		0,00165811 ± 0,00001369		0,0015	
17D28019	9,4 %	0,0103027 ± 0,0001623		0,00114054 ± 0,00000961		0,0014	
17D28021	10,0 %	0,0109170 ± 0,0001799		0,00097774 ± 0,00000902		0,0016	
17D28022	10,8 %	0,0116510 ± 0,0001554		0,00078950 ± 0,00000766		0,0013	
17D28023	11,7 %	0,0131389 ± 0,0001347		0,00046456 ± 0,00000563		0,0009	
17D28025	12,7 %		0,0134104 ± 0,0001097	0,00044812 ± 0,00000557		0,0009	
17D28026	13,8 %		0,0139239 ± 0,0001100	0,00035016 ± 0,00000445		0,0008	
17D28027	14,8 %		0,0140823 ± 0,0001011	0,00034484 ± 0,00000451		0,0007	
17D28029	16,0 %		0,0139540 ± 0,0000818	0,00036602 ± 0,00000448		0,0007	
17D28030	17,0 %		0,0138118 ± 0,0001006	0,00039372 ± 0,00000487		0,0008	
17D28031	18,0 %		0,0136116 ± 0,0001007	0,00039808 ± 0,00000494		0,0007	
17D28033	19,0 %		0,0133754 ± 0,0001316	0,00047617 ± 0,00000592		0,0010	
17D28034	20,3 %		0,0127213 ± 0,0002552	0,00056679 ± 0,00000798		0,0015	
17D28035	22,5 %		0,0129835 ± 0,0004212	0,00056101 ± 0,00001114		0,0020	
17D28037	23,3 %		0,0128217 ± 0,0006838	0,00069496 ± 0,00001541		0,0028	
17D28038	24,4 %		0,0118823 ± 0,0009708	0,00082884 ± 0,00002025		0,0030	
17D28040	25,3 %		0,0120925 ± 0,0013042	0,00078064 ± 0,00002336		0,0031	
Results		40(a)/36(a) ± 2σ		40(r)/39(k) ± 2σ		Age ± 2σ (Ma)	MSWD
Inverse Isochron		352,45 ± 55,49 ± 15,74%		62,60704 ± 1,64989 ± 2,64%		174,51 ± 4,39 ± 2,52%	1,86 7%
		Full External Error ± 5,84 Analytical Error ± 4,38					
Statistics		2σ Confidence Limit Error Magnification Number of Data Points Spreading Factor		Convergence Number of Iterations Calculated Line		0,0000377976 2 Weighted York-2	
		2,07 1,3655 9 8,5%					

Table 4. Age summary of HT-20-A sample.

Relative Abundances	36Ar [fA]	%±σ	37Ar [fA]	%±σ	38Ar [fA]	%±σ	39Ar [fA]	%±σ	40Ar [fA]	%±σ	40i/(39i+K) ± 2σ (Ma)	Age ± 2σ (Ma)	40Ar/(K) (%)	39Ar/(K) (%)	K/Ca ± 2σ			
17027994	0.8%	0.255281	0.444	6.3635	1.707	0.0062093	39.231	0.987885	3.315	81.6140	0.190	9.64004 ± 1.24321	27.99 ± 3.58	8.19	0.82	0.0467 ± 0.0035		
17027996	1.3%	0.512493	0.362	15.6331	0.763	0.1332004	18.405	1.694374	1.471	165.9252	0.138	9.34005 ± 0.75679	27.13 ± 2.18	9.48	1.59	0.0463 ± 0.0016		
17027997	1.8%	0.528866	0.362	15.9580	0.789	0.1156841	18.970	1.607428	1.490	175.3277	0.128	12.66821 ± 0.84930	36.70 ± 2.44	11.54	1.89	0.0549 ± 0.0016		
17027998	2.0%	0.400418	0.340	10.5475	1.077	0.0921819	25.783	1.087761	2.230	135.0483	0.121	16.25052 ± 1.19569	46.94 ± 3.41	13.01	1.28	0.0441 ± 0.0022		
17028000	2.2%	0.349666	0.494	9.2445	1.246	0.0909317	26.770	0.858864	7.286	110.5587	0.113	20.14538 ± 1.51124	110.59 ± 4.28	14.34	1.01	0.0397 ± 0.0024		
17028002	2.4%	0.366911	0.377	9.3831	1.200	0.0909111	26.325	0.750880	3.181	126.5740	0.057	25.37594 ± 1.97293	147.78 ± 6.58	14.68	0.88	0.0341 ± 0.0023		
17028003	2.7%	0.331029	0.388	9.2513	1.195	0.0528227	46.918	0.734921	3.622	116.3691	0.066	26.45997 ± 0.20545	75.82 ± 5.76	16.58	0.86	0.0339 ± 0.0024		
17028005	3.0%	0.351955	0.374	8.8572	1.199	0.0566339	34.521	0.658487	3.810	124.2333	0.053	32.07329 ± 1.74588	91.50 ± 6.66	16.57	0.87	0.0317 ± 0.0021		
17028006	3.5%	0.541524	0.339	11.9240	0.911	0.1096004	22.317	1.055226	2.162	194.7612	0.032	33.00474 ± 1.78140	34.21 ± 4.95	17.78	1.24	0.0378 ± 0.0018		
17028007	3.7%	0.391713	0.376	9.6905	1.092	0.0777601	31.312	0.948392	2.745	147.2401	0.043	38.30892 ± 2.26616	179.15 ± 2.78	11.00	0.94	0.0374 ± 0.0022		
17028009	4.5%	0.346307	0.388	9.2667	1.218	0.0808621	30.442	0.767220	2.157	134.8726	0.035	43.71490 ± 1.98531	123.60 ± 8.16	24.67	0.90	0.0353 ± 0.0024		
17028010	5.0%	0.767022	0.389	11.1835	1.037	0.0582624	40.464	0.746732	3.117	148.2488	0.041	51.54196 ± 1.44474	144.53 ± 9.31	25.65	0.88	0.0284 ± 0.0019		
17028011	5.6%	0.361976	0.377	12.3728	0.828	0.0771028	32.581	0.796199	2.915	146.5715	0.042	48.92854 ± 0.70740	177.97 ± 8.33	26.09	0.93	0.0255 ± 0.0016		
17028013	6.2%	0.3386	0.336	24.8287	0.500	0.1513249	15.957	1.121385	2.072	233.3865	0.036	47.52330 ± 2.28858	133.98 ± 6.22	22.51	1.33	0.0191 ± 0.0009		
17028014	6.8%	0.537145	0.355	27.5983	0.484	0.1380654	18.815	1.133824	2.059	213.1616	0.029	50.83504 ± 2.35792	127.79 ± 6.98	26.57	1.32	0.0174 ± 0.0007		
17028015	7.4%	0.481783	0.369	24.0666	0.508	0.1297141	18.137	1.189519	2.057	200.0529	0.030	50.81359 ± 2.30260	142.89 ± 6.23	29.81	1.39	0.0206 ± 0.0009		
17028017	8.0%	0.410068	0.392	29.1180	0.486	0.0848862	28.621	1.256259	1.909	189.7328	0.032	57.27531 ± 2.41647	160.28 ± 6.47	37.36	1.47	0.0183 ± 0.0008		
17028018	8.7%	0.349160	0.388	43.7573	0.382	0.1011920	22.869	1.707443	1.408	203.4446	0.029	61.76811 ± 1.83348	172.33 ± 4.89	51.00	1.99	0.0165 ± 0.0005		
17028019	9.4%	0.391	0.391	89.9647	0.316	0.299793	10.692	0.302942	0.772	385.8624	0.022	64.34910 ± 1.05070	179.13 ± 2.78	66.02	3.49	0.0141 ± 0.0002		
17028021	10.0%	0.275838	0.424	78.0136	0.322	0.1744133	14.899	2.880846	0.809	259.2635	0.024	65.13477 ± 1.10125	181.21 ± 2.92	71.11	3.35	0.0156 ± 0.0003		
17028022	10.8%	0.767537	0.435	97.8438	0.313	0.2308538	10.505	0.326492	0.655	305.3524	0.020	65.80581 ± 0.89888	192.98 ± 2.38	76.67	4.21	0.0156 ± 0.0002		
17028023	11.7%	0.216339	0.465	177.5099	0.299	0.3667215	6.481	4.874771	0.550	362.3406	0.017	65.66158 ± 0.68515	160.20 ± 1.81	86.77	5.64	0.0151 ± 0.0001		
17028025	12.7%	0.253474	0.461	229.6744	0.296	0.4662078	5.125	5.882662	0.398	427.0222	0.015	64.69454 ± 0.54369	180.04 ± 1.47	86.47	6.07	0.0147 ± 0.0001		
17028026	13.8%	0.236105	0.421	276.6553	0.295	0.5665994	4.091	6.590926	0.380	460.5904	0.014	64.38763 ± 0.51760	179.23 ± 1.37	89.65	7.60	0.0100 ± 0.0001		
17028027	14.8%	0.269554	0.414	341.7784	0.294	0.7286085	3.183	7.462508	0.347	513.5911	0.013	63.77497 ± 0.46768	177.61 ± 1.24	89.81	8.57	0.0091 ± 0.0001		
17028029	16.0%	0.326992	0.385	414.6160	0.293	0.8827773	2.621	8.465914	0.282	586.9692	0.011	63.19267 ± 0.38652	177.97 ± 1.03	89.18	9.70	0.0085 ± 0.0001		
17028030	17.0%	0.280243	0.409	327.9487	0.294	0.648896	3.875	6.930068	0.351	486.4974	0.014	64.97815 ± 0.47739	178.14 ± 1.27	88.88	7.96	0.0088 ± 0.0001		
17028031	18.0%	0.295347	0.409	347.6912	0.294	0.6834886	3.910	7.136757	0.357	505.7019	0.013	64.82459 ± 0.49155	180.19 ± 1.26	88.24	8.15	0.0088 ± 0.0001		
17028033	19.0%	0.247108	0.436	257.4240	0.295	0.8893883	4.663	5.150927	0.372	372.7421	0.017	64.24430 ± 0.46556	178.85 ± 1.71	85.93	5.90	0.0083 ± 0.0001		
17028034	20.3%	0.138245	0.529	121.8298	0.306	0.2537112	9.252	2.441517	0.970	185.7177	0.033	65.44242 ± 1.32601	180.82 ± 3.51	83.25	2.80	0.0083 ± 0.0002		
17028035	22.5%	0.083131	0.739	76.4326	0.327	0.1626220	15.182	1.494567	1.567	111.3316	0.057	64.25267 ± 2.10023	178.87 ± 5.57	83.42	1.71	0.0081 ± 0.0003		
17028037	23.1%	0.056881	0.863	41.4391	0.436	0.0714124	34.658	0.892354	2.563	65.7212	0.050	65.87812 ± 0.54268	172.83 ± 8.94	79.46	0.90	0.0080 ± 0.0003		
17028038	24.4%	0.047314	1.010	29.1451	0.468	0.0806820	30.180	0.583973	3.952	47.5710	0.123	63.54645 ± 2.18757	177.00 ± 13.84	75.51	0.67	0.0083 ± 0.0007		
17028040	25.3%	0.034979	1.215	23.3336	0.551	0.0920422	26.014	0.458991	5.214	36.7170	0.157	63.61950 ± 0.21670	177.19 ± 18.27	76.93	0.53	0.0082 ± 0.0009		
	Σ	10.899495	0.072	3220.8078	0.083	7.8239996	1.794	86.499975	0.161	7869.1747	0.007							
Information on Analysis and Constants Used in Calculations																		
	Results											40a/(36a) ± 2σ	40i/(39i+K) ± 2σ	Age ± 2σ (Ma)	MSWD	39Ar/(K) (%)	K/Ca ± 2σ	
Project = SAYIT (16-34)	Age Equations = Min et al. (2000)																	
Sample = HT-20-A	Negative Intensities = Allowed																	
Material = Homblende	Collector Calibrations = 36Ar																	
Location = Bok/Yakum	Decay 40K = 5.530 ± 0.046 E-10 1/a											64.23136 ± 0.28881 ± 0.4536	178.80 ± 0.80 ± 0.4446	2.51	59.17	0.0089 ± 0.0005	1.5	9
Region = Århus	Decay 39Ar = 2.940 ± 0.016 E-10 1/a											Full External Error ± 4.02			20	20	Confidence Limit	Error Magnification
Analyst = Dan Miggins	Decay 37Ar = 8.230 ± 0.012 E-10 1/a											Full Analytical Error ± 0.77			1.5846			
Irradiation = 17-05U-06 (E025-17)	Decay 36Cl = 2.257 ± 0.015 E-10 1/a																	
Position = K 0.1 Y 0.1 Z 0.31 07757 mm	Decay 40K (ECβ) = 5.580 ± 0.009 E-10 1/a											58.10374 ± 0.20046 ± 0.3498	162.50 ± 0.57 ± 0.3539		34	0.0113 ± 0.0000		
FCT-NNM Age = 28.201 ± 0.023 Ma	Decay 40K (β) = 4.950 ± 0.043 E-10 1/a											Full Analytical Error ± 0.54						
FCT-NNM Reference = Kuiper et al (2008)	Atmospheric 40Ar/(K) = 295.50																	
Normal Isochron	Atmospheric 38Ar/(K) = 0.00189											352.39 ± 56.87 ± 116.14%	62.60638 ± 1.64707 ± 1.7614%	174.50 ± 4.38 ± 2.84%	1.86	59.17		
	Production 39Ar/(39K) = 0.000025 ± 0.0000059											Full External Error ± 5.83			2.07	20	Confidence Limit	Error Magnification
	Production 38Ar/(37K) = 0.000073 ± 0.000000173											Full Analytical Error ± 4.38			1.3638		Error Magnification	
	Production 40Ar/(39K) = 0.0000270 ± 0.0000059														15	Number of Iterations		
	Extraction Method = Bulk Laser Heating														0.0005852137	Convergence		
	Extraction Method = Bulk Laser Heating																	
Heating = 64 sec	Production 36Ar/(K) = 262.80 ± 1.71																	
Isolation = 3.00 min	Scaling Ratio K/Ca = 0.40											352.45 ± 55.49 ± 15.74%	62.60704 ± 1.64989 ± 2.64%	174.51 ± 4.39 ± 2.52%	1.86	59.17		
Instrument = ARGUS-VI-D	Abundance Ratio 40K/K = 1.1700 ± 0.0100 E-04											Full External Error ± 5.84			2.07	20	Confidence Limit	Error Magnification
Preferred Age = Plateau Age	Atomic Weight K = 39.0983 ± 0.0001 g											Full Analytical Error ± 4.38			1.3655		Error Magnification	
Age Classification = Cooling Age															2	Number of Iterations		
(GSR = Undefined)															0.000037976	Convergence		
Rock Class = Undefined															9	Spreading Factor		
Lithology = Undefined																		
Lat-Lon = Undefined - Undefined																		

## HT-16

Table 5. Incremental heating results of HT-16 sample.

Incremental Heating		36Ar(a) [fA]	37Ar(ca) [fA]	38Ar(d) [fA]	39Ar(k) [fA]	40Ar(r) [fA]	Age $\pm 2\sigma$ (Ma)	40Ar(r) (%)	39Ar(k) (%)	K/Ca $\pm 2\sigma$
17D28072	0,8 %	0,4513490	0,8434	0,018544	0,113299	1,5814	40,24 $\pm$ 28,24	1,17	0,14	0,0578 $\pm$ 0,0274
17D28074	1,3 %	0,1494936	1,5405	0,029055	0,112789	3,9215	98,63 $\pm$ 38,87	8,15	0,14	0,0315 $\pm$ 0,0130
17D28075	1,8 %	0,1114881	2,0121	0,034858	0,202162	4,6946	66,47 $\pm$ 16,01	12,47	0,24	0,0432 $\pm$ 0,0111
17D28076	2,0 %	0,0548013	1,1370	0,044912	0,132127	2,9515	63,98 $\pm$ 22,72	15,42	0,16	0,0500 $\pm$ 0,0199
17D28078	2,2 %	0,0291076	0,6040	0,016179	0,094108	2,0275	61,75 $\pm$ 31,00	19,08	0,11	0,0670 $\pm$ 0,0414
17D28079	2,4 %	0,0150786	0,2727	0,012276	0,052587	0,8092	44,31 $\pm$ 39,10	15,37	0,06	0,0829 $\pm$ 0,0941
17D28080	2,7 %	0,0513519	1,7701	0,025855	0,230957	4,4880	55,78 $\pm$ 11,04	22,82	0,28	0,0561 $\pm$ 0,0126
17D28082	3,0 %	0,0254365	1,1659	0,008751	0,165628	3,4169	59,17 $\pm$ 16,19	31,25	0,20	0,0611 $\pm$ 0,0200
17D28083	3,5 %	0,0134174	0,5963	0,000000	0,098685	1,6099	46,95 $\pm$ 21,81	28,88	0,12	0,0712 $\pm$ 0,0413
17D28084	4,0 %	0,0520888	3,3026	0,032047	0,204425	6,9396	96,36 $\pm$ 21,67	31,07	0,25	0,0266 $\pm$ 0,0063
17D28086	4,5 %	0,0341460	3,1211	0,000000	0,163701	6,4742	111,78 $\pm$ 29,10	39,09	0,20	0,0226 $\pm$ 0,0062
17D28087	5,0 %	0,0324228	5,2691	0,000000	0,221455	10,2805	130,52 $\pm$ 25,69	51,76	0,27	0,0181 $\pm$ 0,0037
17D28088	5,6 %	0,0267626	5,6534	0,004330	0,232974	11,0982	133,81 $\pm$ 25,30	58,39	0,28	0,0177 $\pm$ 0,0035
17D28090	6,2 %	0,0105477	1,7563	0,000000	0,109502	4,3904	113,27 $\pm$ 43,91	58,48	0,13	0,0268 $\pm$ 0,0111
17D28091	6,8 %	0,0383351	26,9866	0,069334	0,932203	57,5366	171,54 $\pm$ 7,74	83,55	1,13	0,0149 $\pm$ 0,0007
17D28092	7,4 %	0,0297082	29,6960	0,068045	1,014673	64,1420	175,50 $\pm$ 7,29	87,96	1,23	0,0147 $\pm$ 0,0007
17D28094	8,0 %	0,0315041	44,6366	0,176916	1,438857	89,9335	173,62 $\pm$ 5,37	90,62	1,74	0,0139 $\pm$ 0,0005
17D28095	8,7 %	0,0738654	118,9181	0,426797	3,576892	224,3141	174,17 $\pm$ 2,08	91,13	4,33	0,0129 $\pm$ 0,0002
17D28096	9,4 %	0,1125768	153,6199	0,538974	4,403068	280,3025	176,68 $\pm$ 1,71	89,39	5,33	0,0123 $\pm$ 0,0001
17D28098	10,0 %	0,1501259	186,9158	0,678480	5,239350	330,1172	174,95 $\pm$ 1,50	88,15	6,34	0,0121 $\pm$ 0,0001
17D28099	10,8 %	0,1197354	306,5667	1,125110	8,213321	521,6324	176,28 $\pm$ 1,00	93,65	9,94	0,0115 $\pm$ 0,0001
17D28100	11,7 %	0,0712838	201,0898	0,753553	5,308490	338,0379	176,73 $\pm$ 1,52	94,13	6,43	0,0114 $\pm$ 0,0001
17D28102	12,7 %	0,1781982	568,2209	2,354653	14,199058	900,0750	175,96 $\pm$ 0,63	94,47	17,19	0,0107 $\pm$ 0,0001
17D28103	13,8 %	0,1488708	525,3505	2,179263	12,911140	820,2233	176,33 $\pm$ 0,64	94,91	15,63	0,0106 $\pm$ 0,0001
17D28104	14,8 %	0,1253217	340,4807	1,346501	8,572306	545,6415	176,66 $\pm$ 0,93	93,64	10,38	0,0108 $\pm$ 0,0001
17D28106	16,0 %	0,1086443	227,5488	0,850897	5,714096	367,0615	178,21 $\pm$ 1,43	91,96	6,92	0,0108 $\pm$ 0,0001
17D28107	17,0 %	0,0945376	163,6935	0,658982	3,896481	249,6078	177,74 $\pm$ 1,93	89,93	4,72	0,0102 $\pm$ 0,0001
17D28108	18,0 %	0,0853208	106,7474	0,399069	2,550376	159,8519	174,08 $\pm$ 2,83	86,38	3,09	0,0103 $\pm$ 0,0002
17D28110	19,0 %	0,0523059	45,4457	0,207091	1,071711	66,6675	172,83 $\pm$ 6,54	81,18	1,30	0,0101 $\pm$ 0,0004
17D28111	20,3 %	0,0526228	28,3686	0,114848	0,650679	41,4135	176,64 $\pm$ 11,87	72,70	0,79	0,0099 $\pm$ 0,0007
17D28112	22,5 %	0,0321099	23,5457	0,093038	0,552033	33,9785	171,09 $\pm$ 13,95	78,17	0,67	0,0101 $\pm$ 0,0009
17D28114	23,3 %	0,0438515	9,1130	0,000000	0,222789	13,0111	162,72 $\pm$ 32,31	50,10	0,27	0,0105 $\pm$ 0,0022
$\Sigma$		2,6064101	3135,9886	12,268357	82,601925	5168,2312				
Information on Analysis		Results		40(r)/39(k) $\pm 2\sigma$		Age $\pm 2\sigma$ (Ma)		MSWD	39Ar(k) (%n)	K/Ca $\pm 2\sigma$
Project = SAYIT (16-34)		Age Plateau		63,51544 $\pm 0,16532$ $\pm 0,26\%$		176,30 $\pm 0,52$ $\pm 0,29\%$		1,79	91,31	0,0111 $\pm 0,0004$
Sample = HT-16								4%	13	
Material = Hornblende								1,82	2 $\sigma$ Confidence Limit	
Location = BoÅŸYazkale								1,3382	Error Magnification	
Region = ÅŖorum										
Analyst = Dan Miggins		Total Fusion Age		62,56793 $\pm 0,19729$ $\pm 0,32\%$		173,79 $\pm 0,59$ $\pm 0,34\%$			32	0,0113 $\pm 0,0000$
Irradiation = 17-OSU-06 (6X28-17)										
J = 0.00161224 $\pm$ 0.00000132										
FCT-NM = 28.201 $\pm$ 0.023 Ma										

Table 6. Inverse isochron data of HT-16.














Inverse Isochron		39(k)/40(a+r) ± 2σ		36(a)/40(a+r) ± 2σ		r.i.	
17D28072	0,8 %		0,0008395 ± 0,0003317	0,00334444 ± 0,00002337		0,0001	
17D28074	1,3 %		0,0023450 ± 0,0009108	0,00310818 ± 0,00003162		0,0003	
17D28075	1,8 %		0,0053710 ± 0,0012483	0,00296201 ± 0,00003316		0,0007	
17D28076	2,0 %		0,0069013 ± 0,0023957	0,00286239 ± 0,00005216		0,0012	
17D28078	2,2 %		0,0088540 ± 0,0044062	0,00273855 ± 0,00007352		0,0016	
17D28079	2,4 %		0,0099882 ± 0,0085056	0,00286398 ± 0,00013900		0,0024	
17D28080	2,7 %		0,0117461 ± 0,0022170	0,00261167 ± 0,00005294		0,0017	
17D28082	3,0 %		0,0151489 ± 0,0040775	0,00232650 ± 0,00007378		0,0024	
17D28083	3,5 %		0,0177022 ± 0,0080283	0,00240681 ± 0,00012151		0,0035	
17D28084	4,0 %		0,0091540 ± 0,0020821	0,00233249 ± 0,00004182		0,0011	
17D28086	4,5 %		0,0098827 ± 0,0026226	0,00206141 ± 0,00005290		0,0013	
17D28087	5,0 %		0,0111500 ± 0,0022595	0,00163245 ± 0,00004046		0,0014	
17D28088	5,6 %		0,0122576 ± 0,0023914	0,00140807 ± 0,00003936		0,0012	
17D28090	6,2 %		0,0145863 ± 0,0057973	0,00140500 ± 0,00008666		0,0017	
17D28091	6,8 %		0,0135367 ± 0,0006370	0,00055667 ± 0,00001318		0,0005	
17D28092	7,4 %		0,0139147 ± 0,0006034	0,00040740 ± 0,00001216		0,0005	
17D28094	8,0 %		0,0144983 ± 0,0004680	0,00031744 ± 0,00000897		0,0004	
17D28095	8,7 %		0,0145319 ± 0,0001801	0,00030009 ± 0,00000545		0,0003	
17D28096	9,4 %		0,0140418 ± 0,0001408	0,00035902 ± 0,00000501		0,0004	
17D28098	10,0 %		0,0139910 ± 0,0001243	0,00040089 ± 0,00000457		0,0004	
17D28099	10,8 %		0,0147453 ± 0,0000861	0,00021496 ± 0,00000335		0,0003	
17D28100	11,7 %		0,0147827 ± 0,0001317	0,00019851 ± 0,00000402		0,0002	
17D28102	12,7 %		0,0149035 ± 0,0000544	0,00018704 ± 0,00000282		0,0002	
17D28103	13,8 %		0,0149397 ± 0,0000560	0,00017226 ± 0,00000263		0,0002	
17D28104	14,8 %		0,0147120 ± 0,0000798	0,00021508 ± 0,00000326		0,0003	
17D28106	16,0 %		0,0143151 ± 0,0001196	0,00027218 ± 0,00000409		0,0003	
17D28107	17,0 %		0,0140392 ± 0,0001586	0,00034062 ± 0,00000527		0,0004	
17D28108	18,0 %		0,0137810 ± 0,0002331	0,00046103 ± 0,00000668		0,0005	
17D28110	19,0 %		0,0130499 ± 0,0005143	0,00063691 ± 0,00001250		0,0007	
17D28111	20,3 %		0,0114227 ± 0,0008012	0,00092380 ± 0,00001829		0,0006	
17D28112	22,5 %		0,0127001 ± 0,0010808	0,00073872 ± 0,00001960		0,0006	
17D28114	23,3 %		0,0085790 ± 0,0017722	0,00168860 ± 0,00003565		0,0010	
Results		40(a)/36(a) ± 2σ		40(r)/39(k) ± 2σ		Age ± 2σ (Ma)	MSWD
Inverse Isochron		289,15 ± 34,64		63,61458 ± 0,55880		176,56 ± 1,50	1,92
Error Chron		± 11,98%		± 0,88%		± 0,85%	3%
				Full External Error ± 4,17			
				Analytical Error ± 1,48			
Statistics		2σ Confidence Limit		Convergence		0,0000005198	
		Error Magnification		Number of Iterations		3	
		Number of Data Points		Calculated Line		Weighted York-2	
		Spreading Factor					

Table 7. Age summary of HT-16 sample.

Relative Abundances		36Ar [fA]	%1σ	37Ar [fA]	%1σ	38Ar [fA]	%1σ	39Ar [fA]	%1σ	40Ar [fA]	%1σ	40(r)/39(k) ± 2σ	Age ± 2σ (Ma)	40Ar(r) (%)	39Ar(k) (%)	K/Ca ± 2σ										
17D28072	0,8 %	0,4515792	0,348	0,8434	13,116	0,104421	21,740	0,113840	19,660	134,9551	0,024	13,95747 ± 9,90445	40,24 ± 28,24	1,17	0,14	0,0578 ± 0,0274										
17D28074	1,3 %	0,1499135	0,503	1,5405	6,998	0,058635	40,994	0,113779	19,251	48,0969	0,059	34,78652 ± 14,08076	98,63 ± 38,87	8,15	0,14	0,0315 ± 0,0130										
17D28075	1,8 %	0,1120360	0,552	2,0121	5,480	0,058499	39,090	0,203455	11,546	37,6395	0,068	23,22215 ± 5,69816	66,47 ± 16,01	12,47	0,24	0,0432 ± 0,0111										
17D28076	2,0 %	0,0551139	0,894	1,1370	9,692	0,056955	42,048	0,132858	26,111	19,1454	0,136	22,33817 ± 8,07206	63,98 ± 22,72	15,42	0,16	0,0500 ± 0,0199										
17D28078	2,2 %	0,0292727	1,311	0,6040	18,324	0,022865	104,449	0,094496	24,779	10,6289	0,232	21,54489 ± 11,00286	61,75 ± 31,00	19,08	0,11	0,0670 ± 0,0414										
17D28079	2,4 %	0,0151537	2,357	0,2727	37,507	0,015778	147,965	0,052762	42,434	5,2649	0,493	15,38755 ± 13,74277	44,31 ± 39,10	15,37	0,06	0,0829 ± 0,0941										
17D28080	2,7 %	0,0516234	0,995	1,7701	6,094	0,038560	59,903	0,232094	9,390	19,6626	0,128	19,43209 ± 3,90416	55,78 ± 11,04	22,82	0,28	0,0561 ± 0,0126										
17D28082	3,0 %	0,0257527	1,546	1,1659	9,309	0,015715	142,551	0,166377	13,395	10,9335	0,225	20,62980 ± 5,73950	59,17 ± 16,19	31,25	0,20	0,0611 ± 0,0200										
17D28083	3,5 %	0,0135785	2,445	0,5963	18,071	<b>0,000259</b>	9276,533	0,099068	22,584	5,5748	0,449	16,31372 ± 7,67851	46,95 ± 21,81	28,88	0,12	0,0712 ± 0,0413										
17D28084	4,0 %	0,0529853	0,873	3,3026	3,287	0,044845	52,100	0,206547	11,255	22,3320	0,108	33,94699 ± 7,84009	96,36 ± 21,67	31,07	0,25	0,0266 ± 0,0063										
17D28086	4,5 %	0,0349897	1,241	3,1211	3,515	0,033455	676,087	0,165706	13,107	16,5645	0,149	39,54826 ± 10,61605	111,78 ± 29,10	39,09	0,20	0,0226 ± 0,0062										
17D28087	5,0 %	0,0338470	1,177	5,3691	2,164	<b>0,017633</b>	139,036	0,224841	9,979	19,8615	0,133	46,42225 ± 9,46956	130,52 ± 25,69	51,76	0,27	0,0181 ± 0,0037										
17D28088	5,6 %	0,0282913	1,312	5,6534	2,068	0,013163	177,938	0,236606	9,604	19,0067	0,128	47,63703 ± 9,34323	133,81 ± 25,30	58,39	0,28	0,0177 ± 0,0035										
17D28090	6,2 %	0,0110224	2,924	1,7563	5,838	<b>0,014016</b>	160,160	0,110631	19,667	7,5073	0,321	40,09403 ± 16,03482	113,27 ± 43,91	58,48	0,13	0,0268 ± 0,0111										
17D28091	6,8 %	0,0456378	0,990	26,8666	0,481	0,092615	26,035	0,949542	2,310	68,8652	0,038	61,72115 ± 2,91880	171,54 ± 7,74	83,55	1,13	0,0149 ± 0,0007										
17D28092	7,4 %	0,0377430	1,170	29,6960	0,447	0,091197	26,410	1,033753	2,128	72,9214	0,039	63,21440 ± 2,75371	175,50 ± 7,29	87,96	1,23	0,0147 ± 0,0007										
17D28094	8,0 %	0,0435903	1,015	44,6366	0,364	0,208216	11,619	1,467536	1,582	99,2439	0,032	62,50344 ± 2,02590	173,62 ± 5,37	90,62	1,74	0,0139 ± 0,0005										
17D28095	8,7 %	0,1060594	0,624	118,9181	0,289	0,505206	4,628	3,653297	0,606	246,1435	0,013	62,71203 ± 0,78496	174,17 ± 2,08	91,13	4,33	0,0129 ± 0,0002										
17D28096	9,4 %	0,1541640	0,501	153,6199	0,284	0,640842	3,800	4,501769	0,490	313,5716	0,012	63,66072 ± 0,64687	176,68 ± 1,71	89,39	5,33	0,0123 ± 0,0001										
17D28098	10,0 %	0,2007294	0,418	186,9158	0,282	0,803459	2,946	5,559444	0,434	374,4825	0,010	63,00727 ± 0,56813	174,95 ± 1,50	88,15	6,34	0,0121 ± 0,0001										
17D28099	10,8 %	0,2027334	0,441	306,5667	0,277	1,301863	1,803	8,410291	0,284	557,0192	0,008	63,51052 ± 0,37681	176,28 ± 1,00	93,65	9,94	0,0115 ± 0,0001										
17D28100	11,7 %	0,1257274	0,556	201,0898	0,281	0,867183	2,709	5,437690	0,434	359,1055	0,010	63,67873 ± 0,57318	176,73 ± 1,52	94,13	6,43	0,0114 ± 0,0001										
17D28102	12,7 %	0,3320667	0,376	568,2209	0,275	2,661720	0,897	14,564140	0,176	952,7412	0,005	63,38977 ± 0,23799	175,96 ± 0,63	94,47	17,19	0,0107 ± 0,0001										
17D28103	13,8 %	0,2911307	0,358	525,3505	0,275	2,457578	0,968	13,248677	0,181	864,2225	0,006	63,52834 ± 0,24374	176,33 ± 0,64	94,91	15,63	0,0106 ± 0,0001										
17D28104	14,8 %	0,2175128	0,414	340,4807	0,277	1,547338	1,525	8,791065	0,263	582,6792	0,008	63,65165 ± 0,35152	176,66 ± 0,93	93,64	10,38	0,0108 ± 0,0001										
17D28106	16,0 %	0,1702514	0,465	227,5488	0,279	0,981171	2,409	5,860296	0,406	399,1693	0,010	64,23789 ± 0,54313	178,21 ± 1,43	91,96	6,92	0,0108 ± 0,0001										
17D28107	17,0 %	0,1388619	0,516	163,6935	0,283	0,753174	3,291	4,001654	0,549	277,5460	0,012	64,05980 ± 0,73216	177,74 ± 1,93	89,93	4,72	0,0102 ± 0,0001										
17D28108	18,0 %	0,1142219	0,534	106,7474	0,294	0,465030	5,268	2,618962	0,823	185,0658	0,018	62,67778 ± 1,06967	174,08 ± 2,83	86,38	3,09	0,0103 ± 0,0002										
17D28110	19,0 %	0,0646163	0,790	45,4457	0,370	0,237990	9,975	1,109910	1,918	82,1245	0,036	62,20657 ± 2,46823	172,83 ± 6,54	81,18	1,30	0,0101 ± 0,0004										
17D28111	20,3 %	0,0603044	0,861	28,3686	0,469	0,137648	17,814	0,668906	3,411	56,9640	0,045	63,64661 ± 4,48972	176,64 ± 11,87	72,70	7,09	0,0099 ± 0,0007										
17D28112	22,5 %	0,0384853	1,102	23,5457	0,542	0,109944	21,927	0,567162	4,141	43,4673	0,058	61,55161 ± 5,25831	171,09 ± 13,95	78,17	0,67	0,0101 ± 0,0009										
17D28114	23,3 %	0,0463147	0,992	9,1130	1,200	0,011881	192,981	0,228644	10,063	25,9693	0,104	58,40088 ± 12,12737	162,72 ± 32,31	50,10	0,27	0,0105 ± 0,0022										
Σ		3,4555182	0,111	3135,9886	0,091	14,262436	0,939	84,616798	0,152	5938,4755	0,003															
<b>Information on Analysis and Constants Used in Calculations</b>																										
<b>Results</b>																										
Project = SAYIT (16-34) Sample = HT-16 Material = Homblende Location = BoÅYazkale Region = AÅorum Analyst = Dan Miggins Irradiation = 17-OSU-06 (BX28-17) Position = K: 0   Y: 0   Z/H: 34,28375 mm FCT-NM Age = 28.201 ± 0.023 Ma FCT-NM Reference = Kuiper et al (2008) Preferred Age = Plateau Age FCT-NM1 value = 0.00161224 ± 0.00000132 Air Shot MDF = 0.9938052 ± 0.00059289 (LIN) Experiment Type = Incremental Heating Extraction Method = Bulk Laser Heating Heating = 64 sec Isolation = 3.00 min Instrument = ARGUS-VI-D Preferred Age = Plateau Age Age Classification = Cooling Age IGN = Undefined Rock Class = Undefined Uhtology = Undefined Lat-Lon = Undefined - Undefined												Age Equations = Min et al. (2000) Negative Intensities = Allowed Collector Calibrations = 36Ar Decay 40K = 5.530 ± 0.048 E-10 1/h Decay 39Ar = 2.940 ± 0.016 E-07 1/h Decay 37Ar = 8.230 ± 0.012 E-04 1/h Decay 36Cl = 2.257 ± 0.015 E-06 1/a Decay 40K(β-) = 0.580 ± 0.009 E-10 1/a Decay 40K(β+) = 4.950 ± 0.043 E-10 1/a Atmospheric 40/36(a) = 295.50 Atmospheric 38/36(a) = 0.1869 Production 39/37(ca) = 0.0006425 ± 0.0000059 Production 38/37(ca) = 0.0001800 ± 0.0000173 Production 36/39(k) = 0.0002703 ± 0.0000005 Production 40/39(k) = 0.000607 ± 0.000059 Production 38/39(k) = 0.012077 ± 0.000011 Production 36/38(c) = 262.80 ± 1.71 Scaling Ratio K/Ca = 0.430 Abundance Ratio 40K/K = 1.1700 ± 0.0100 E-04 Atomic Weight K = 39.0983 ± 0.0001 g					Age Plateau 63,51544 ± 0,16532 ± 0,26% Full External Error ± 3,92 Analytical Error ± 0,44 Total Fusion Age 62,56793 ± 0,19729 ± 0,32% Full External Error ± 3,88 Analytical Error ± 0,52 Normal Isochron 288,64 ± 35,37 ± 12,25% 63,62099 ± 0,55809 ± 0,88% Full External Error ± 4,17 Inverse Isochron 288,64 ± 35,37 ± 11,98% 63,61458 ± 0,55880 ± 0,88% Full External Error ± 4,17					Age ± 2σ (Ma) 176,30 ± 0,52 ± 0,29% 173,79 ± 0,59 ± 0,34% 176,58 ± 1,50 ± 0,85% 176,58 ± 1,50				